The Effects of Diabatic Heating on the Paradigmatic LC1 and LC2 Baroclinic Lifecycles

Susanne Moen Olsen

Master Thesis in Meteorology
Geophysical Institute
University of Bergen

June 2023

Abstract

Extratropical cyclones play a crucial role in determining mid-latitude weather, where the atmosphere is on average inducive to baroclinic instability. Literature has identified two lifecycle behaviors, one that is predominantly anticyclonic (LC1) and one mostly cyclonic (LC2). The lifecycle behavior is strongly influenced by the structure of the zonal mean wind. While baroclinic lifecycles have been extensively studied using dry models, this thesis introduce moisture into the model and focuses on exploring the impact of diabatic heating on the LC1 and LC2 paradigms on an f-plane. In addition to the traditional approach of triggering baroclinic wave growth using the most unstable normal mode, we also consider the influence of localized perturbations, which allows for the development of upstream and downstream cyclones. Our investigation contains two parts: first, we examine the effects of diabatic heating using modal perturbed simulations, while in the second part, we explore the impact of diabatic heating on localized perturbed simulations. Our results show that the inclusion of moisture leads to intensified and more rapid cyclone growth. The LC1 lifecycle appears to be the most sensitive to the presence of moisture, with dry simulations primarily favoring anticyclonic development at the surface and minimal cyclone growth until later stages, whereas moist simulations accelerate cyclogenesis at an earlier time. Furthermore, our investigations reveal that higher maximum relative humidity levels amplify the northward transport of moisture.

Acknowledgments

First and foremost I would like to thank my main supervisor Thomas Spengler for the guidance and support through the process of writing this thesis. I would also like to thank my co-supervisor Andrea Marcheggiani for the support, advice, and programming help. This project has been challenging, but mostly enjoyable. I am grateful for the opportunity to work with the WRF model and the learning opportunity this thesis has given me. Additional thanks to Clemens Spengsberge for much helpful advice on getting WRF running properly.

I would also like to thank my fellow students at GFI for the endless amount of breaks, the useful discussions, and the friendships that have developed over the last couple of years. Additional thanks to Hannah for volunteering to do proofreading for me.

Contents

List of Figures

List of Tables

Acronyms

EKE	Eddy Kinetic Energy
EP-flux	Eliassen-Palm flux
LC1	Lifecycle 1
LC2	Lifecycle 2
NE-SW	Northeast-southwest
NW-SE	Northwest-southeast
RH	Relative humidity
TCWV	Total Column Water Vapor
THM93	Thorncroft et al. (1993)
WRF	Weather Research and Forecasting

1 Introduction

Mid-latitude weather is primarily influenced by extratropical cyclones and anticyclones. Cyclones, often referred to as eddies within the context of the atmospheric flow, are characterized by low-pressure centers and are the main drivers of changes in temperature, wind speed, precipitation, and cloud cover (*Lamb*, 1991). The passage of one or multiple cyclones through an area often brings a substantial amount of moisture (*Dacre et al.*, 2019), which can potentially lead to heavy rainfall (*Pfahl and Wernli*, 2012) and significant socio-economic impacts for the affected region. For example, the storm Klaus (January 2009) resulted in approximately US$6.6 billion in total economic losses (*Liberato et al.*, 2011; *Aon-Benfield*, 2010) while after storm Xynthia (February 2010) it was reported a total loss of approximately US$4.5 billion (*Liberato et al.*, 2013). On the other hand, anticyclones (or high-pressure systems) bring about stable and dry conditions, characterized by the absence of rain and clouds and are associated with more calm weather conditions (*Johannessen*, 1970). Given the considerable impact of extratropical cyclones on local weather conditions, it is essential to understand their characteristics and behavior.

The formation and growth of extratropical cyclones are closely connected to baroclinic instability (*Charney*, 1947; *Eady*, 1949). Baroclininc instability arises from horizontal temperature gradients in a rotating and stratified atmosphere where temperature (T) and pressure (p) gradients are not parallel everywhere ($\nabla T \times \nabla p \neq 0$, *Holton and Hakim*, 2012). The instability grows by converting the potential energy of the mean flow into eddy kinetic energy (*Pierrehumbert and Swanson*, 2003).

We refer to a baroclinic zone as an unstable environment where baroclinic waves can spontaneously form and amplify in response to minor disturbances, such as a temperature anomaly (*Thorncroft et al.*, 1993; *Holton and Hakim*, 2012). Baroclinic instability has been extensively investigated and studied, with the formulation of various models aimed at understanding and explaining this phenomenon. Notable examples include the Eady and Charney models, which are simplified mathematical theories focused on explaining baroclinic instability in terms of the growth rate of the most unstable mode (*Charney*, 1947; *Eady*, 1949).

The trajectory of extratropical cyclones is closely intertwined with the zonal mean wind and jet stream (*Murray and Johnson*, 1952; *Vederman*, 1954; *Ferreira et al.*, 2016). In the mid-latitudes, the zonal flow is predominantly in the eastward direction, with a maximum in the upper troposphere (*Vallis*, 2017a). Within this westerly flow region, two distinct jets are observed: the subtropical jet around $30°N$ and the polar jet located further north (*Vallis*, 2017a). Our primary focus is on the polar jet ($40° - 60°N$), which exhibits westerly winds extending all the way to the surface. The interaction between the wind and the surface leads to momentum convergence caused by friction. This convergence arises due to the transient eddies, which is why it is also referred to as the eddy-driven jet (*Vallis*, 2017a). The presence of stirring in the mid-latitudes induces outward propagation of Rossby waves. By definition, the direction of momentum fluxes

is opposite to the wave propagation direction (*Vallis*, 2017a). Consequently, when eddies propagate outwards from the stirring region, there is a net convergence of the momentum fluxes into the same region, resulting in the emergence or acceleration of a net eastward flow (*Vallis*, 2017a).

A mid-latitude cyclone typically undergoes a series of distinct stages in its lifetime (or lifecycle), namely corresponding to cyclogenesis, intensification, and dissipation. The different stages were first identified within the Norwegian cyclone model (*Bjerknes and Solberg*, 1922). In the initial stage of cyclogenesis, a low-pressure system forms as a result of interactions between two contrasting air masses (figure 1.1a,b).

In the intensification stage, the cyclone begins to draw in relatively warm, moist air from the south and cool, dry air from the north resulting in the characteristics of counterclockwise circulation commonly observed in northern hemisphere cyclones (figure 1.1c,d). The interface between the relatively warm and cold air masses is referred to as the frontal zone, which exhibits strong temperature and pressure gradient (*Bjerknes*, 1919; *Bjerknes and Solberg*, 1922). The frontal zone consists of two distinct fronts: a warm front,

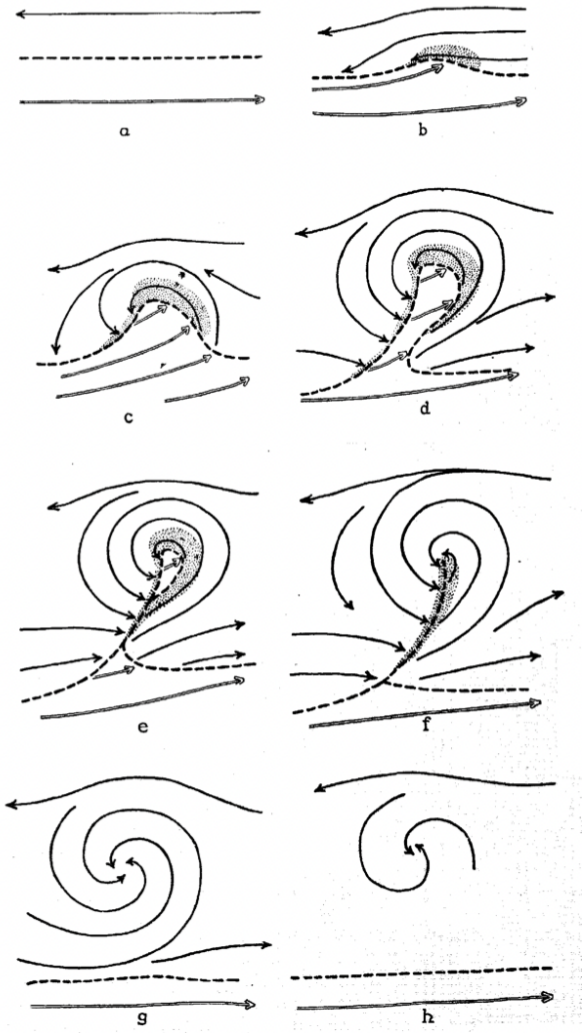

Figure 1.1: Schematic of the lifecycle of extratropical cyclones (taken from Bjerknes and Solberg, 1922)

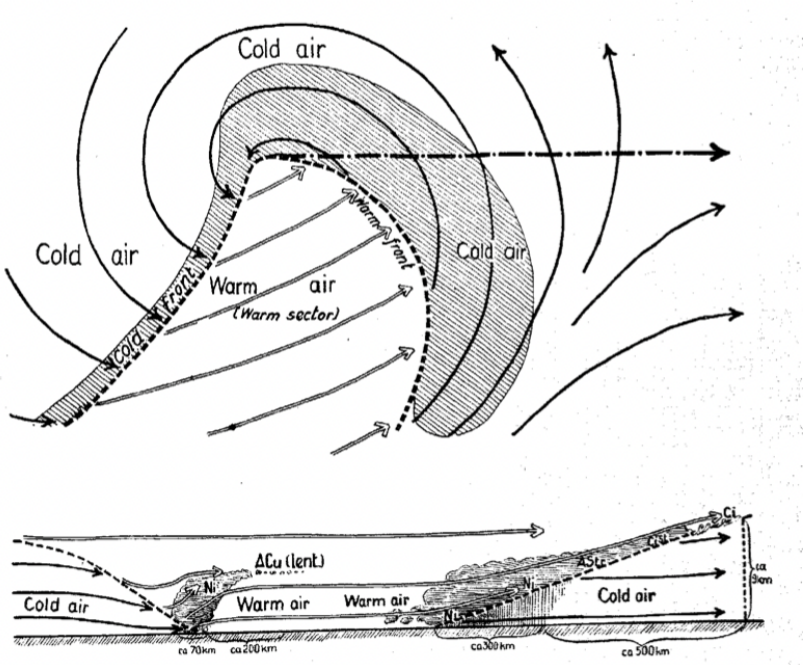

Figure 1.2: Schematic of a well-developed idealized cyclone (taken from Bjerknes and Solberg, 1922)

where warm, moist air is lifted and displaced northward, and a cold front, where cold, dry air is displaced southward figure 1.2. As the warm, moist air at the frontal zone ascends, it cools and becomes saturated forming clouds and precipitation (*Bjerknes*, 1919).

During the intensification process, the cold front advances faster than the warm front, eventually catching up and the fronts start to occlude (figure 1.1e,f). At the end of this stage, the warm air detaches from the surface and the cyclone enters the final phase of its lifecycle (i.e. dissipation). During the dissipation stage, the cyclone undergoes a weakening process, causing it to lose its structure and organization, while the atmospheric conditions gradually return to a more stable state (figure 1.1g,h).

It is useful to think of cyclones and anticyclones as one atmospheric system (or baroclinic wave), and then explain the behavior of its moist and dry air masses by following the isentropic motion (figure 1.3; *Thorncroft et al.*, 1993). The warm conveyor belt is composed of ascending warm, moist air originating from the south-west of the warm front (*Bjerknes*, 1919; *Carlson*, 1980), while the dry intrusion consists of descending dry air originating from the upper level of the troposphere (*Dacre et al.*, 2019). In the warm conveyor belt, the lower-level warm, moist air moves poleward, rising and splitting into two branches (C and D in Figure 1.3). Branch C exhibits a cyclonic motion, while branch D indicates an anticyclonic motion. Similarly, the descending dry air from the dry conveyor belt also splits into two branches, with branch A taking an anticyclonic trajectory while branch B takes a cyclonic trajectory. This classification allows us to identify A and D as instances of anticyclonic behavior, characterized by backward-tilting and narrowing troughs of isentropic surfaces that move equatorward. Conversely, B and C represent cases of cyclonic wave breaking, characterized by forward-tilting isentropic surfaces that wrap up cyclonically (*Thorncroft et al.*, 1993).

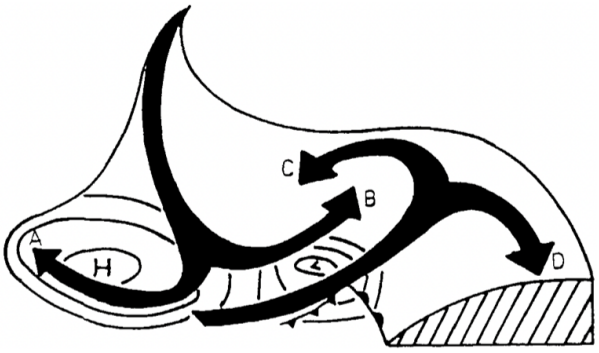

Figure 1.3: A schematic of isentropic motion of the baroclinic wave. The solid arrows indicate the flow along a sloping isentropic surface relative to the surface pressure. (Figure is taken from Thorncroft et al., 1993)

Thorncroft et al. (1993, hereafter THM93) first investigated the lifecycles of baroclinic waves and their response to changes in the mean zonal wind. They identified two distinct behaviors, anticyclonic and cyclonic, primarily driven by the structure of the zonal mean wind profile. First, they prescribed westerly zonal flow (figure 1.4a), which leads to a lifecycle of predominantly anticyclonic behavior of the air masses, referred to as LC1. Other notable features include the growth of large anticyclones, accompanied by a northward displacement of developing surface cyclones. Additionally, the jet undergoes a northward shift during this process.

On the other hand, by introducing a barotropic shear to the zonal winds (figure 1.4), a significantly different development is observed, referred to as LC2. This barotropic shear consists of westerly winds at $20°N$ and easterly winds at $50°N$ which is added to the mean zonal wind used in LC1. The isentropic motion of the air exhibits predominantly cyclonic motion throughout the lifecycle of the baroclinic wave. Some other distinctive characteristics involve the formation of large, circular cyclones that are primarily confined in the meridional direction. Additionally, there is a slight equatorward shift observed in the jet.

In baroclinic lifecycle studies, it is common to use the most unstable normal mode (also referred to as modal) as a perturbation to the basic state (*Davies et al.* 1991; THM93). However, in modally perturbed experiments, the zonal symmetry of the perturbation constrains the evolution of surface cyclones and anticyclones, leading to a fixed zonal distance between each cyclone and anticyclone throughout the simulation (*Davies et al.*, 1991). This symmetry is loosened by imposing a localized (nonmodal) initial perturbation (*Wernli et al.*, 1998). By introducing such a perturbation, we allow for the development of both upstream and downstream cyclones and anticyclones (*Wernli et al.*, 1999). An upstream cyclone or anticyclone develops to the east of the primary system, while a downstream cyclone or anticyclone develops to the west of the primary system.

Extratropical cyclones are responsible for the net poleward heat transport in the midlatitudes (*Blackmon et al.*, 1977) and are therefore expected to decrease the horizontal temperature gradient between tropical and polar regions (*Charney*, 1947; *Eady*, 1949; *Blackmon et al.*, 1977). As a result, the eddies decrease the baroclinicity of the atmo-

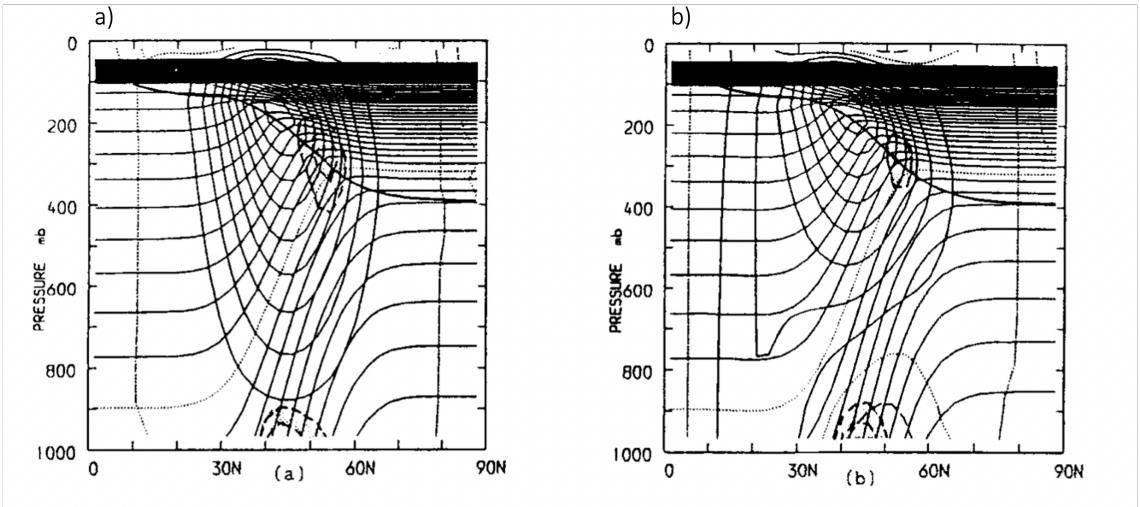

Figure 1.4: The initial zonal mean wind (contours with interval of $5ms^{-2}$) for a) LC1 and b) LC2 of THM93 baroclinic-lifecycle stydy. The dotted line indicates zero wind. Potential temperature with a contour interval of 5K (dotted line is 300K). The shading indicates regions of eddy kinetic energy maxima. (The figure is taken from THM93)

sphere. However, *Hoskins and Valdes* (1990) argues that diabatic heating associated with these eddies can act as a self-maintenance mechanism of the storm track by replenishing baroclinicty.

The slope of the isentropic surfaces can be used as a tool to quantify the contribution of the various physical processes that maintain baroclinicity (*Papritz and Spengler*, 2015) because the isentropic surface is proportional to the horizontal temperature gradient and the inverse static stability (*Delden*, 1999). The two largest contributors to the change of slope of the isentropic surface are the isentropic displacement of the surface (tilt) and its deformation by diabatic heating (*Papritz and Spengler*, 2015). The tilt of the surface is related to the growth of extratropical cyclones which tends to flatten the isentropic slope and reduce baroclinicity, while diabatic heating is a restoring force that, climatologically, is counterbalanced by the tilting term (*Papritz and Spengler*, 2015). The results from *Papritz and Spengler* (2015) reinforce the argument by *Hoskins and Valdes* (1990) that diabatic processes provide for a self-maintenance mechanism for cyclone activity (storm track).

Diabatic processes, in the form of latent heat release, are associated with the ascent of warm, moist air from the warm conveyer belt which then condensates and releases latent heat to the surrounding environment (*Lin*, 2007). Even though latent heat release within the cyclone itself enhances instability in its wake allowing for more cyclone activity (*Papritz and Spengler*, 2015; *Weijenborg and Spengler*, 2020), the diabatic processes can also have a strong impact on the intensification of individual storms (*Danard*, 1964; *Wernli et al.*, 2002; *Ludwig et al.*, 2014; *Schemm et al.*, 2013), where the latent heating induces growth but also reduces the horizontal scale (*Craig and Cho*, 1988; *Moore and Montgomery*, 2004). Latent heat release also contributes to the increase of eddy available potential energy in extratropical cyclones (*Vincent et al.*, 1977; *Lin and Smith*, 1979) and therefore enhances the conversion to kinetic energy (*Robertson and Smith*,

1983).

Many studies on baroclinic lifecycle are based on dry simulations of the atmosphere (*Davies et al.*, 1991; *Thorncroft et al.*, 1993; *Jäger et al.*, 2023). However, as discussed previously, moisture plays quite an important role in cyclone growth and intensification. This raises the question of how moisture affects the evolution of the two baroclinic lifecycles by THM93.

In this study, we first reproduce the two distinct lifecycle behaviors described by THM93, here using the Weather Research and Forecasting (WRF) model on an f-plane approximation. We then compare our results with the results by THM93. Afterward, we introduce moisture into the simulations to explore how the synoptic evolution is affected by moist processes.

In the second part of this thesis, we carry out similar experiments but with a localized surface perturbation instead of a modal perturbation. The objective is to examine how the basic state responds to this type of disturbance in comparison to the modal perturbation. We follow the same structure as the first part, namely first focusing on dry dynamics and subsequently introducing moisture.

2 Method

2.1 Model Setup

We use the Weather Research and Forecasting (WRF) model (Version 4.4, *Skamarock et al.*, 2021) which is a well-developed and widely tested mesoscale numerical weather prediction system designed for both operational forecasting and research purposes. WRF is suitable for simulations based on actual atmospheric conditions (real) and idealized conditions (ideal). In this thesis, the non-hydrostatic real version of the WRF model is used to conduct the experiments.

An overview of the model setup, including relevant parameters and their values, can be found in table 2.1. The simulations are conducted in a periodic channel with a horizontal resolution of 20 km. The vertical domain consists of 60 eta-levels, and the time increment is set to 120 seconds. The zonal length of the channel spans 28 000 km, approximately equal to the Earth's circumference at 45°N latitude, while the meridional width covers 10 000 km, approximately representing the distance from the Equator to the Pole. The model top is defined at 10 hPa to ensure that it does not interfere with the zonal wind field. With 60 eta levels, the vertical extent of the model reaches 29 km. Additionally, the experiments are conducted on an f-plane centered at 45°N. The model setup does not incorporate a boundary layer, and the zonal boundaries are periodic, ensuring continuity in the zonal direction. The lateral boundaries are defined with a relaxation zone at the meridional walls.

In the dry simulations, all physical parameterization schemes, including microphysics, cumulus convection physics, radiation, surface layer, and boundary layer physics, are deactivated. This allows us to focus solely on the dynamic aspects of the experiments. In contrast, the moist simulations incorporate microphysics and cumulus convective

Table 2.1: Model setup

Parameterization scheme	**Description**
Microphysics	WRF Single-Moment (WSM) 5-class scheme (*Hong et al.*, 2004)
Cumulus convective	Kain-Fritsch scheme (*Kain*, 2004)
Boundaries	**Description**
Zonal	Periodic
Meridional	Specified with relaxation zone
Resolution & domain size	**Values**
Horizontal resolution	20 km
Vertical resolution	60 eta levels
Time step	120 sec
Zonal length	28 000 km
Meridional length	10 000 km
Model height	29 km

schemes. These two schemes are the only physics parameterization schemes used, while radiation, surface layer, and boundary layer physics are not included in any of the simulations. This allows us to investigate the influence of moisture on the synoptic evolution.

The microphysics scheme is responsible for capturing microscale processes that influence clouds and precipitation. It specifically addresses the formation and growth of cloud and precipitation particles (*Warner*, 2011a). In this study, we use the WRF single-moment 5-class (WSM5) microphysics scheme (*Hong et al.*, 2004). This scheme is an improved version of the WSM 3-class scheme and utilizes bulk parameterization techniques to represent microphysical processes associated with clouds and precipitation. It accounts for five distinct hydrometeor classes, namely vapor, ice, snow, rain, and cloud. Unlike a two-moment scheme that considers both particle concentration and mass, the single-moment scheme focuses solely on mass for each water phase (*Hong et al.*, 2004).

The convective parameterization scheme plays a crucial role in capturing sub-grid scale convection that cannot be explicitly resolved on the model grid. It calculates the vertical transport of heat, moisture, and momentum resulting from convective processes (*Warner*, 2011a). In our study, we employ the Kain-Fritsch cumulus scheme, which is a one-dimensional entraining or detraining cloud model derived from the Fritsch-Chappell cumulus scheme (*Kain*, 2004). This scheme incorporates a downdraft feature within the cloud model. It has been designed for grid lengths of approximately around 25 km and is suited for simulating convective processes in midlatitude environments (*Kain*, 2004).

2.2 Initial Setup

The initial setup is established using the approach by *Terpstra and Spengler* (2015), which ensures geostrophic and hydrostatic balance in the initial conditions. This method offers the flexibility to define the wind field, and the other atmospheric parameters are derived based on the thermal wind balance, geostrophic equation, hydrostatic equation, and equation of state. The thermal wind balance,

$$\frac{\partial u_g}{\partial dz} = u_g \frac{\partial lnT}{\partial dz} - \frac{g}{f}\frac{\partial lnT}{\partial dy} = u_g \frac{\partial ln\theta}{\partial dz} - \frac{g}{f}\frac{\partial ln\theta}{\partial dy}. \tag{2.1}$$

where u_g, θ, T, f, and g are geostrophic wind, potential temperature, temperature, Coriolis parameter, and gravity, respectively.
Given the wind field and assuming geostrophic balance,

$$u_g = \frac{1}{\rho f}\frac{\partial p}{\partial y}, \tag{2.2}$$

and hydrostatic balance,

$$\frac{\partial p}{\partial z} = -\rho g, \tag{2.3}$$

we can define the pressure field as:

$$\left[u_g \frac{\partial}{\partial z} - \frac{g}{f}\frac{\partial}{\partial y}\right] p = 0, \tag{2.4}$$

where p and ρ are the pressure and density. The Coriolis parameter (f) and gravity (g) are assumed to be constant. With the use of equation (2.3) and equation (2.4) we can derive the density from the equation of state,

$$p = \rho R_d T, \tag{2.5}$$

where R_d is the gas constant for dry air.

Equations (2.1) to (2.5) provides the atmospheric field for a dry atmosphere. With the use of virtual temperature (T_v), we can include moisture into the equation of state,

$$p = \rho R_d T_v \quad , \quad T_v \approx (1 + 0.61q)T, \tag{2.6}$$

where q is the water vapor mixing ratio. By using the virtual temperature we ensure the unsaturated Brunt-Väisälä frequency (N_m),

$$N_m = \sqrt{\frac{g}{\theta_v}\frac{\partial \theta_v}{\partial_z}} \quad , \quad \theta_v \approx (1 + 0.61q)\theta, \tag{2.7}$$

remains unchanged when moisture is added. Here θ_v is the virtual potential temperature.

2.2.1 Boundaries

To determine the pressure field (equation (2.4)) and to subsequently calculate the other atmospheric parameters, it is necessary to determine boundary conditions for the y and z directions. The first step is to define the vertical pressure profile at the southern boundary as $p_{-L}(z)$. At the upper boundary, we require ($u_g = 0$), which implies that $\partial p/\partial y|_L = 0$ and p = constant at the upper boundary. We also require that $\partial p/\partial y|_L$ is zero at the northern boundary. Since $p_{-L}(z)$ determines the stratification at $-L$, we can use the potential temperature at the southern boundary,

$$\theta_{-L,z_{k+1}} = \theta_{-L,z_k} exp\left[\frac{N^2_{z_k}}{g}(z_{k+1} - z_k)\right], \tag{2.8}$$

to calculate $p_{-L}(z)$, where k is the index for the z levels. We can define N_{z_k} as

$$N_{z_k} = \begin{cases} N_t, & z_k \leq Z_{trop} \\ N_s, & z_k > Z_{trop}, \end{cases} \tag{2.9}$$

where the tropospheric and stratospheric Brunt-Väisälä frequency, N_t^2 and N_s^2 are given in table 2.2 and table 2.3. The pressure at the southern boundary can then be calculated using the equation:

Table 2.2: Overview over initial conditions for each modal perturbation experiment

Options	Values						Description
	D-LC1	D-LC2	M-LC1-R30	M-LC2-R30	M-LC1-R40	MLC2-R40	
Basic state							
$p_0(hPa)$	948	1058	948	1058	958	1058	Sea level pressure at southern boundary
$\theta_0(K)$	298	298			301	293	Surface potential temperature at southern boundary
$Z_{trop}(km)$	14	14	14	14	14	14	Tropopause height at southern boundary
$N_t^2(s^{-2})$	$11x10^{-4}$	$11x10^{-4}$	$11x10^{-4}$	$11x10^{-4}$	$11x10^{-4}$	$11x10^{-4}$	Static stability of the troposphere
$N_s^2(s^{-2})$	$4x10^{-4}$	$4x10^{-4}$	$4x10^{-4}$	$4x10^{-4}$	$4x10^{-4}$	$4x10^{-4}$	Static stability of the stratosphere
Zonal mean wind							
$U_0(ms^{-1})$	45	45	45	45	45	45	Maximum jet speed
$L_y(km)$	1500	1500	1500	1500	1500	1500	Meridional width of jet from $y = 0$
$l_1 \& l_2$	0.1	0.1	0.1	0.1	0.1	0.1	Transition zone
$Z_{jet}(km)$	12	12	12	12	12	12	Jet core altitude
$Z_u(km)$	12	12	12	12	12	12	Vertical distance from jet core to jet top
$Z_l(km)$	13	13	13	13	13	13	Vertical distance from jet core towards the surface
$u_0(ms^{-1})$	10	-10	10	-10	10	-10	Maximum shear speed
t	2	2	2	2	2	2	Exponential coefficient for vertical shear profile
$h_s(km)$	13	13	13	13	13	13	Scaling height for the shear
$z_u(km)$	25	25	25	25	25	25	Vertical extent of shear from surface
$l_y(km)$	500	500	500	500	500	500	Characteristic length of the hyperbolic tangent function
Perturbation							
$z_p(km)$	0	0	0	0	0	0	Core altitude of initial perturbation
$H_p(km)$	4	4	4	4	4	4	Vertical extent of perturbation
$y_0(km)$	0	0	0	0	0	0	Meridional placement of perturbation
$\delta p(hPa)$	-1	1	-1	1	-1	1	Magnitude of perturbation
k	5	6	5	6	5	6	Wavenumber
Moisture							
$rh_0(\%)$			60	60	80	80	Maximum RH at the surface
$z_{rh}(km)$			12	12	12	12	Scaling height
n			4	4	4	4	Decaying parameter

Table 2.3: Overview over initial conditions for each localized finite pressure perturbation experiment

Options	Values						Description
	LD-LC1	**LD-LC2**	**LM-LC1-R30**	**LM-LC2-R30**	**LM-LC1-R40**	**LM-LC2-R40**	
Basic state							
$p_0(hPa)$	948	1058	948	1058	958	1058	Sea level pressure at southern boundary
$\theta_0(K)$	298	298			301	293	Surface potential temperature at southern boundary
$Z_{trop}(km)$	14	14	14	14	14	14	Tropopause height at southern boundary
$N_t^2(s^{-2})$	$11x10^{-4}$	$11x10^{-4}$	$11x10^{-4}$	$11x10^{-4}$	$11x10^{-4}$	$11x10^{-4}$	Static stability of the troposphere
$N_s^2(s^{-2})$	$4x10^{-4}$	$4x10^{-4}$	$4x10^{-4}$	$4x10^{-4}$	$4x10^{-4}$	$4x10^{-4}$	Static stability of the stratosphere
Zonal mean wind							
$U_0(ms^{-1})$	45	45	45	45	45	45	Maximum jet speed
$L_y(km)$	1500	1500	1500	1500	1500	1500	Meridional width of jet from $y = 0$
$l_1\&l_2$	0.1	0.1	0.1	0.1	0.1	0.1	Transition zone
$Z_{jet}(km)$	12	12	12	12	12	12	Jet core altitude
$Z_u(km)$	12	12	12	12	12	12	Vertical distance from jet core to jet top
$Z_l(km)$	13	13	13	13	13	13	Vertical distance from jet core towards the surface
$u_0(ms^{-1})$	10	-10	10	-10	10	-10	Maximum shear speed
t	2	2	2	2	2	2	Exponential coefficient for vertical shear profile
$h_s(km)$	13	13	13	13	13	13	Scaling height for the shear
$z_u(km)$	25	25	25	25	25	25	Vertical extent of shear from surface
$l_y(km)$	500	500	500	500	500	500	Characteristic length of the hyperbolic tangent function
Perturbation							
$z_p(km)$	0	0	0	0	0	0	Core altitude of initial perturbation
$H_p(km)$	4	4	4	4	4	4	Vertical extent of perturbation
$R_p(km)$	120	120	120	120	120	120	Radius of the initial perturbation
$y_0(km)$	0	0	0	0	0	0	Meridional plancement of perturbation
$x_0(km)$	6000	6000	6000	6000	6000	6000	Zonal placement of perturbation
$\delta p(hPa)$	-1	-1	-1	-1	-1	-1	Magnitude of perturbation
Moisture							
$rh_0(\%)$			60	60	80	80	Maximum RH at the surface
$z_{rh}(km)$			12	12	12	12	Scaling height
n			4	4	4	4	Decaying parameter

$$p_{-L,z_{k+1}} = \left[p^{\alpha}_{-L,z_k} - \frac{2(z_{k+1} - z_k) p_0^{\alpha} \alpha g}{R_d(\theta_{-L,z_{k+1}} + \theta_{-L,z_k})} \right]^{1/\alpha}. \tag{2.10}$$

$p_0 = 1000$ is the reference pressure, c_p is the heat capacity for dry air at constant pressure, and $\alpha = \frac{R_d}{c_p}$.

To define density, we use linear extrapolation,

$$\rho = \rho_{z_1} + 2(\rho_{z_{0.5}} - \rho_{z_1}) \tag{2.11}$$

where z_0 is the lower boundary and $z_{0.5}$ and z_1 is the layer above. Finally the lower boundary condition can be expressed with the use of pressure,

$$u_{g_{y_j,z_0}} \left(\frac{-3p_{y_j,z_0} + 4p_{y_j,z_1} - p_{y_j,z_2}}{2\partial z} \right) - \frac{g}{f} \left(\frac{p_{y_{j+1},z_0} - p_{y_{j-1},z_0}}{2\partial y} \right), \tag{2.12}$$

where j is the grid point position in the y-direction.

2.2.2 Basic State

Wind Field

The initial zonal mean wind field (U) consists of an asymmetric jet (u) of westerly winds with a tangent hyperbolic shear (u_s) added to the zonal wind field (figure 2.1),

$$U(y, z^*) = u(y, z^*) + u_s(y, z^*). \tag{2.13}$$

The parameters used in the wind field setup can be found in table 2.2 (modal perturbed experiments) and table 2.3 (localized perturbed experiments).

The asymmetric jet (*Bui and Spengler*, 2021), consist of a horizontal ($W_y(y)$) and vertical ($W_z(z^*)$) function,

$$u(y, z^*) = U_0 W_y(y) W_z(z^*), \tag{2.14}$$

where U_0 defines the maximum wind velocity at jet core and z^* is the transformed vertical coordinate defined as:

$$z^*(y, z) = z + A tanh\left(\frac{y_{jet} - y}{B} \right). \tag{2.15}$$

Here, y_{jet} is the meridional location of the jet with origin at $y = 0, z = 0$. $y_{jet} = 0$ is the center of the domain. A and B are empirical parameters and are defined as:

$$A(z) = |Z_{jet} - Z_{trop}| \begin{cases} 0, & z < -L_z \\ sin\left(\frac{\pi}{2} \frac{Z_u + z}{Z_u}\right), & -Z_u \leq z \leq 0 \\ 1, & z > 0, \end{cases} \tag{2.16}$$

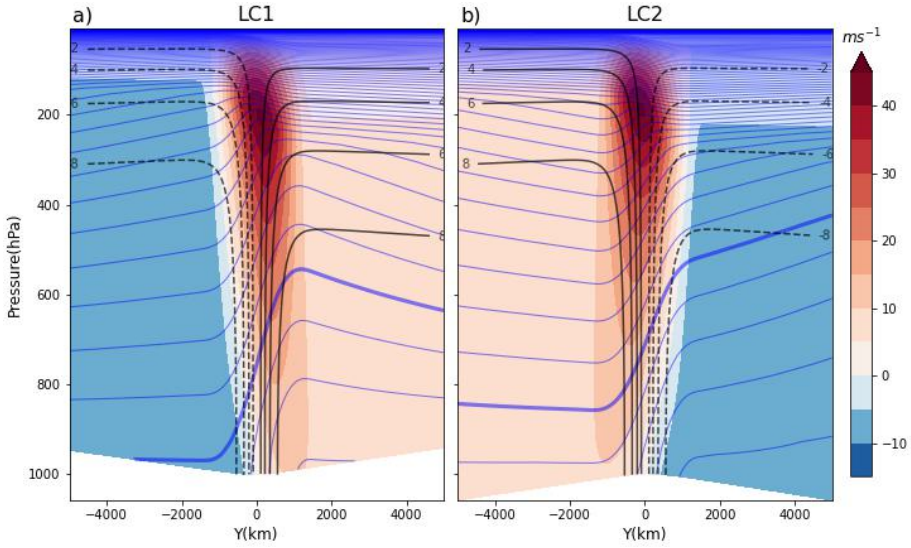

Figure 2.1: Mean zonal wind (shading in ms^{-1}), shear (black contours in ms^{-1}), and potential temperature (blue contours in K) for a) LC1 and b) LC2. The potential temperature contours are drawn at intervals of 5hPa with the bold line representing the 300K contour.

$$B = \frac{2L_y}{5}. \tag{2.17}$$

Here, Z_{jet}, Z_{trop}, Z_u, and L_y are the jet core altitude, tropopause height at the southern boundary, vertical extent from the jet core, and the meridional width of the jet from $y = 0$. Using the transformed vertical coordinate (z^*) we define the horizontal ($W_y(y)$) and vertical ($W_z(z^*)$) wind profiles,

$$W_y(y) = cos^2\left(\frac{\pi}{2}\frac{y - y_{jet}}{L_y}\right), \tag{2.18}$$

$$W_z(z) = \begin{cases} C\left(\frac{z}{l_1}\right)^2\left[\frac{1}{6}\left(\frac{z}{l_1}^2\right) - 1\right], & |z| \le l_1 \\ w_0 - \alpha|z|, & l_1 < |z| < Z_u - l_2 \\ \frac{\alpha l_2}{2}\left(\frac{Z_u - |z|}{l_2}\right)^3\left(2 - \frac{Z_u - |z|}{l_2}\right), & Z_u - l_2 \le |z| \le Z_u \\ 0, & |z| > Z_u, \end{cases} \tag{2.19}$$

where l_1 and l_2 defines the transition zones. w_0, C, and α are defined with the equations:

$$w_0 = \frac{1}{1 - \frac{3}{8}\frac{l_1}{Z_u - 0.5l_2}}, \tag{2.20}$$

$$C = \frac{3}{4}w_0\frac{l_1}{Z_u - 0.5l_2}, \tag{2.21}$$

$$\alpha = \frac{w_0}{Z_u - 0.5l_2}. \tag{2.22}$$

The hyperbolic shear (u_s), inspired by *Schemm et al.* (2013), added to the zonal mean

wind field consist of a horizontal ($w_y(y)$) and vertical ($w_z(z^*)$) function,

$$u_s(y, z^*) = u_0 w_y(y) w_z(z^*), \tag{2.23}$$

where u_0 is the maximum shear velocity and z^* is the transformed vertical coordinate defined in equation (2.15). The horizontal ($w_y(y)$) and vertical ($w_z(z^*)$) shear functions are defined as:

$$w_y(y) = \tanh\left(\frac{y}{l_y}\right), \tag{2.24}$$

$$w_z(z^*) = \begin{cases} \cos^t\left(\frac{\pi}{4}\frac{z}{H_s}\right), & z < z_u \\ 0, & \text{otherwise.} \end{cases} \tag{2.25}$$

Here l_y is the characteristic length of the hyperbolic tangent function, H_s is the scaling height, and z_u defines the vertical extent of shear.

The tangent hyperbolic shear (u_s) produces anticyclonic horizontal wind shear at the surface for LC1 (figure 2.1a) and cyclonic surface wind shear for LC2 (figure 2.1b). For LC1, the configuration allows the growth of large anticyclones and smaller cyclones to the north. Conversely, for LC2 the configuration allows for the growth of large, meridional confined surface cyclones.

Reproducing the distinct characteristics of THM93's LC1 and LC2 lifecycle proved to be challenging and required several attempts. The shear setup used in this thesis is somewhat different compared to the original barotropic shear described by THM93. The specific equations of the zonal mean wind are not provided in THM93. Several studies have interpreted the written explanation and constructed their own set of equations for the zonal mean wind (*Polvani and Esler*, 2007; *Jäger et al.*, 2023). In our initial attempt to replicate LC1 and LC2, we draw inspiration from the equations presented in *Jäger et al.* (2023), which yield a symmetric jet with surface shear decreasing with height. Further details regarding the modified shear setup for our initial attempt are found in appendix A.1.

The approach inspired by *Jäger et al.* (2023), which incorporates an exponential decrease in shear with height, does not produce the desired distinct lifecycle behaviors with our model setup. A closer examination of the initial zonal mean wind presented in THM93 (figure 1.4), we notice that the added shear to the main jet is barotropic in nature, with a constant wind speed throughout the entire tropopause. In our next attempt, we made modifications to the equations in our initial attempt (see appendix A.1) to establish a barotropic contribution. Additional information regarding the setup of the barotropic shear is found in appendix A.2. However, the obtained results portray similar characteristics as our initial attempt and do not show the expected characteristics of THM93's LC1 and LC2. Instead, a prevailing cyclonic behavior is observed in both cases.

Only after incorporating a tangent hyperbolic shear profile, modified from a study by *Schemm et al.* (2013), we are able to successfully replicate the distinct characteristics of

LC1 and LC2. The study by *Schemm et al.* (2013) is conducted on an f-plane, similar to the experiments in this thesis.

Initial Perturbation

Two types of initial pressure perturbation are introduced, a modal perturbation (i.e., a wave perturbation pattern) and a localized finite pressure perturbation (figure 2.2). The localized perturbation is similar to *Bui and Spengler* (2021),

$$p'(r,z) = \begin{cases} \Delta p \cos^2\left(\frac{\pi}{2}\frac{z-Z_p}{H_p}\right)\left(1-R^2\right)^3, & r < R_p \text{ and } -H_p < z - Z_p < H_p \\ 0, & \text{otherwise,} \end{cases} \tag{2.26}$$

where Δp is the magnitude, Z_p is the core altitude, H_p is the vertical extent, and R is the standardized distance from perturbation location,

$$R = \frac{r}{R_p}. \tag{2.27}$$

R_p is the radius of initial perturbation where r,

$$r = \sqrt{(x-x_0)^2 + (y-y_0)^2}, \tag{2.28}$$

defines the zonal and meridional coordinates. Origin (x_0, y_0) is at the center of the perturbation.

The modal perturbation is based on localized finite pressure perturbation (equation (2.26)),

$$p'(x,y,z) = \begin{cases} \Delta p \cos^2\left(\frac{\pi}{2}\frac{z-Z_p}{H_p}\right)\left(1-R^2\right)^3, & y < \frac{L_x}{4k} \text{ and } -H_p < z - Z_p < H_p \\ 0, & \text{otherwise,} \end{cases} \tag{2.29}$$

where k is the wavenumber in the zonal direction. In this case, R is defined as:

$$R = \frac{(y-y_0)^2}{\frac{L_x}{4}}. \tag{2.30}$$

Here L_x is the zonal length of the domain. R scales the meridional width of individual perturbation to the zonal length.

Both the modal and localized initial pressure perturbation introduced in our experiment has a small amplitude and is surface-based (see table 2.2 and table 2.3 for values used for each experiment). We use $k = 5$ for the modal LC1 experiments and $k = 6$ for the modal LC2 experiments. The particular choice of wavenumber is to optimize the wavelength for each dry experiment to achieve symmetry of the evolving systems.

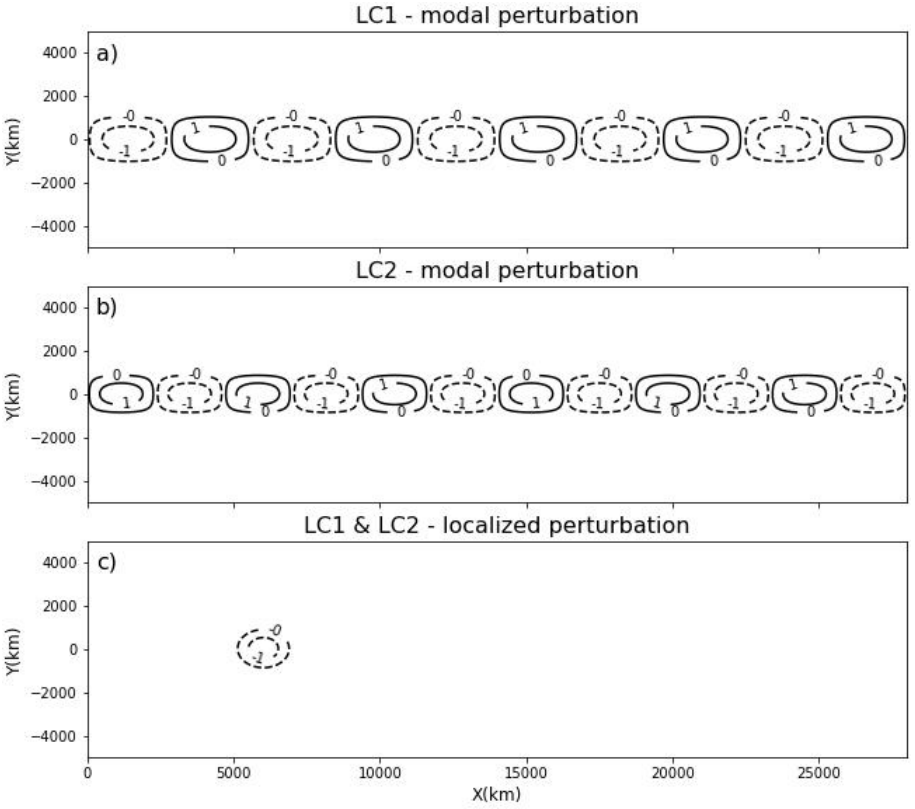

Figure 2.2: Initial perturbation (in hPa) for LC1 and LC2. a),b) modal and c) localized perturbation

Initial Moisture Content

To compute the initial moisture, we utilize the same method as *Terpstra and Spengler* (2015). The vertical distribution of relative humidity ($rh(z)$),

$$rh(z) = rh_0 e^{-0.5\left(\frac{z}{z_{rh}}\right)^n}, \tag{2.31}$$

provide a horizontal, uniform relative humidity profile (RH) (figure 2.3). rh_0, z_{rh}, and n are the maximum RH at the surface, scaling height, and decay parameter, respectively.

With the use of the RH profile, we can calculate the water vapor mixing ratio,

$$q(y,z) = rh(z) * \frac{R_d}{R_v}\left[\frac{e_s(y,z)}{p(y,z) - e_s(y,s)}\right], \tag{2.32}$$

where R_v is the gas constant for water vapor. e_s is the saturated vapor pressure,

$$e_s(y,z) = \begin{cases} \frac{R_d}{R_v} exp\left[17.67\left(\frac{T(y,z)-T_f}{T(y,z)-29.65}\right)\right], & T(y,z) > T_f \\ \frac{R_d}{R_v} exp\left[21.87\left(\frac{T(y,z)-T_f}{T(y,z)-7.66}\right)\right], & T(y,z) \leq T_f, \end{cases} \tag{2.33}$$

where T_f defines if we are above or below the freezing level ($T_f = 273.15K$).

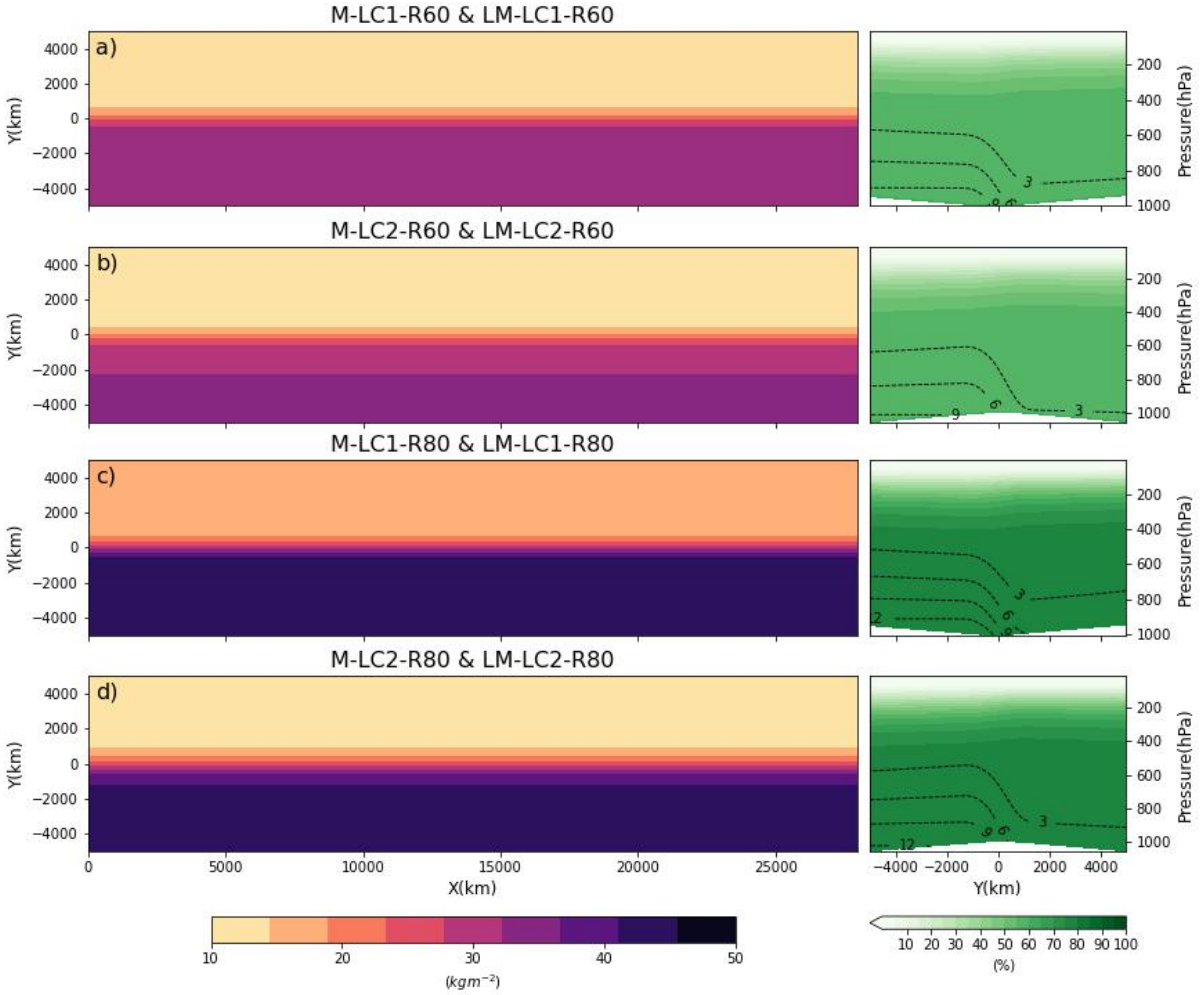

Figure 2.3: a),c),e),h) displays the TCWV content (shading in kgm^{-2}) and b),d),f),h) displays the RH (green shading in %) and total water vapor mixing ratio (blue stippled contours in gkg^{-1}).

The horizontal, homogeneous RH profile gives us the maximum water vapor mixing ratio at the surface in the south of the domain. The water vapor mixing ratio decays both with height and northward (figure 2.3).

To control the amount of moisture in the initial setup, we calculate the total column water vapor ($TCWV$),

$$TCWV = \int_{z_0}^{z_1} q * \rho(y, z) * dz, \tag{2.34}$$

from the surface (z_0) to model top (z_1). TCWV is the parameter we use to ensure both LC1 and LC2 have the same amount of moisture.

TCWV is calculated using the density field (equation (2.34)). Density depends on pressure and temperature(equation (2.5)) and pressure and temperature depend on the wind field (equation (2.4)). Due to this relationship, the TCWV distribution on the southern side of the domain is affected by the direction of wind shear. Notice from figure 2.4a) that

LC1 experiments have an increase in TCWV between y = −5000km and y=−1200km, before decreasing. LC2 decreases slowly over the same distance, before rapidly decreasing between the northern and southern part of the domain (figure 2.4b)). To ensure we have the correct amount of initial moisture we calculate the average TCWV between $y_0 = -5000km$ and $y_1 = -1200km$,

$$TCWV_{south} = \int_{y_0}^{y_1} TCWV(y)dy. \tag{2.35}$$

There are two ways to change the moisture content. Either by changing the RH profile (equation (2.31)) or changing the surface potential temperature at the southern boundary ($th0$). See table 2.2 and table 2.3 for values used to determine the moisture content for each experiment.

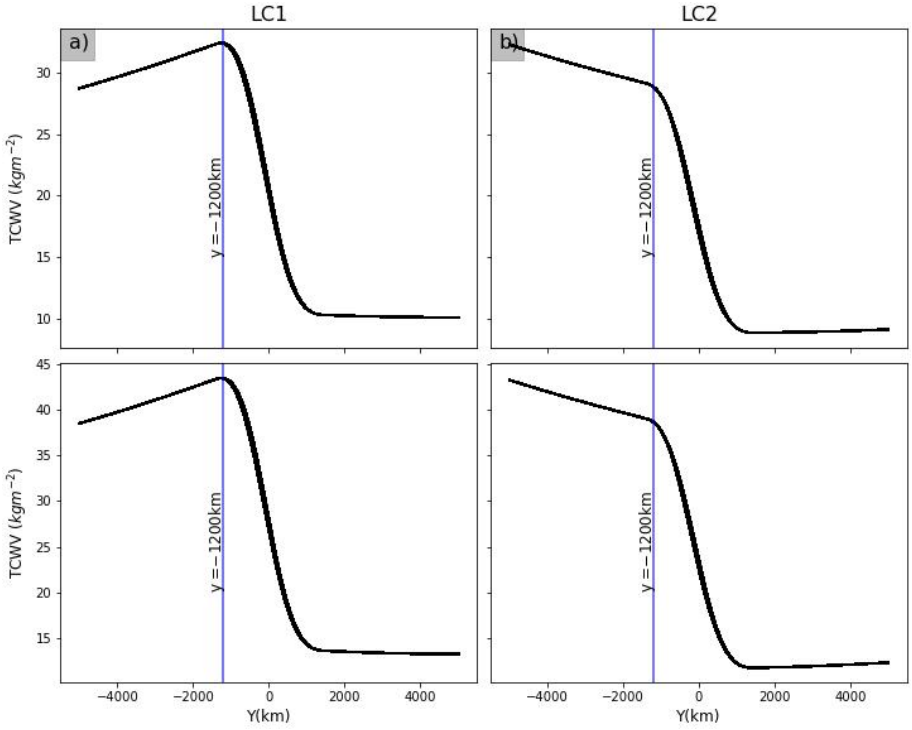

Figure 2.4: The meridional TCWV distribution (in kgm^{-2}) for a) LC1 experiemnts and b) LC2 experiments. The vertical blue line indicates the -1200km mark for calculation of $TCWV_{south}$.

2.3 Experiment Design

An overview of the experiment setup is found in table 2.4. Included in this thesis are 12 experiments of which six have a modal wave perturbation and six have a localized perturbation. Within the first six experiments in table 2.4, two are dry and four experiments include moisture with varying moisture content. The dry modal perturbed experiments (D-LC1 and D-LC2) are for comparison to THM93's experiments of lifecycle LC1 and LC2. The next four experiments (M-LC1-R60, M-LC1-R80, M-LC2-R60, and M-LC2-R80) are to investigate how the two distinct lifecycle behaviors change when introducing moisture into the model. For the last six experiments in table 2.4, denominate with an L, we repeat the previous six experiments, but with a localized pressure perturbation instead of a modal wave perturbation. All of the experiments have a duration of 15 days.

Table 2.4: Experiment design overview

Experiment	Physics	Wind setup	Perturbation	Maximum RH
D-LC1	No	LC1	Modal	
D-LC2	No	LC2	Modal	
M-LC1-R60	Yes	LC1	Modal	RH = 60%
M-LC2-R60	Yes	LC2	Modal	RH = 60%
M-LC1-R80	Yes	LC1	Modal	RH = 80%
M-LC2-R80	Yes	LC2	Modal	RH = 80%
LD-LC1	No	LC1	Localized	
LD-LC2	No	LC2	Localized	
LM-LC1-R60	Yes	LC1	Localized	RH = 60%
LM-LC2-R60	Yes	LC2	Localized	RH = 60%
LM-LC1-R80	Yes	LC1	Localized	RH = 80%
LM-LC2-R80	Yes	LC2	Localized	RH = 80%

2.4 Diagnostics

2.4.1 Eddy kinetic energy

Baroclinic waves undergo growth by transforming available potential energy into kinetic energy (*Pierrehumbert and Swanson*, 2003). This occurs as warm, lighter air parcels are lifted, while cold and denser air parcels descend. Consequently, the fluid's center of gravity shifts downward, converting potential energy into EKE (*Vallis*, 2017b). To calculate the EKE (K_E) of our experiments, we base our calculations on the energy framework of *Lorenz* (1955),

$$K_E = \int_{y_0}^{y_1} \int_{z_0}^{z_1} \overline{\frac{1}{2}(u'^2 + v'^2)} dz dy, \tag{2.36}$$

where the bottom and top vertical boundary for the calculations are $z_0 = 0$ (surface) and $z_1 = 29$km (model top), respectively. We are only interested in the EKE of the troposphere and therefore only use values below the pressure level of 150hPa. The

meridional boundaries are set to $y_0 = -3000$km and $y_1 = 3000$km. u' and v' represent the eddy zonal and meridional velocity components,

$$u' = u - \overline{u} \quad , \quad v' = v - \overline{v}. \tag{2.37}$$

2.4.2 Eliassen-Palm flux

Mid-latitude eddies serve as the primary mechanism for heat transport between lower and higher latitudes (*Blackmon et al.*, 1977). The EP-flux explores the interaction eddies have on the zonal mean flow, by quantifying the momentum and heat flux (*Eliassen and Palm*, 1960). The EP-flux is derived from a set of Quasi-geostrophic potential vorticity (q) and buoyancy (b) equations following *Vallis* (2017c),

$$\frac{\partial q}{\partial t} + J(\psi, q) = D, \quad q = \beta y + \left[\nabla^2 + \frac{\partial}{\partial z}\left(\frac{f_0^2}{N^2}\frac{\partial}{\partial z}\right)\right]\psi \quad , \quad 0 < z < H \tag{2.38a}$$

$$\frac{\partial b}{\partial t} + J(\psi, b) + wN^2 = H, \quad b = f_0\frac{\partial \psi}{\partial z} \quad , \quad z = 0, H, \tag{2.38b}$$

where N, ψ, β, and f_0 are the brunt-Väisäla frequency, stream function, and Coriolis parameters, respectivly. D and H are non-conservative terms of the potential vorticity (equation (2.38a)) and heating term (equation (2.38b)), respectively.

From equation (2.38) we can derive the zonally averaged vorticity flux (detailed derivation found in appendix A.3),

$$\overline{v'q'} = \nabla \cdot \mathcal{F} = -\frac{\partial}{\partial y}(u'v') + \frac{\partial}{\partial z}\left(\frac{f_0^2}{N^2}v'b'\right). \tag{2.39}$$

$\nabla \cdot \mathcal{F}$ is the divergence of EP-flux, where EP-flux is defined as:

$$\mathcal{F} = -\overline{u'v'}\mathbf{j} + \frac{f_0}{N^2}\overline{v'b'}\mathbf{k}. \tag{2.40}$$

From Equation (2.39) we can deduce that both the eddy momentum and heat flux influence the zonal mean flow. A standard method of presenting the EP-flux is to calculate the meridional cross-section and display the EP-flux in terms of arrows and its divergence in terms of contours (*Edmon et al.*, 1980). Upward arrows indicate a contribution from heat fluxes with little contribution from momentum fluxes. In contrast, horizontal arrows indicate a contribution from momentum fluxes with little contribution from heat fluxes. It is important to note that the momentum flux contribution to the potential vorticity flux is defined as "downgradient". This implies that when we observe horizontal arrows directed northward, the momentum flux contribution is southward.

The contours representing the divergence of the EP-flux provide valuable insights into the regions where momentum and heat flux work to accelerate or decelerate the zonal mean flow. A positive divergence of the EP-flux results in the acceleration of the zonal mean flow. On the other hand, a negative divergence, or convergence, of the EP-flux indicates a deceleration of the zonal mean flow, suggesting that the combined effects of momentum and heat flux act to reduce the zonal mean flow.

3 Results and Discussion

First, we examine experiments D-LC1 and D-LC2 and compare the results with the study by THM93. Thereafter, we assess how diabatic heating influences the synoptic evolution of LC1 and LC2. Finally, we analyze how the use of localized pressure perturbation instead of modal perturbation impacts the outcomes of both dry and moist LC1 and LC2 experiments. In modal and localized perturbed LC1 experiments and modal perturbed LC2 experiments, there is no significant development of cyclones or anticyclones prior to day 4, while localized LC2 simulations experience no significant development prior to day 8. Therefore, results and discussion cover day 4 and onwards for modal perturbed and localized LC1 experiments and from day 8 for localized LC2 experiments.

THM93 included figures of surface pressure, 2PVU potential temperature, zonal mean zonal wind, EP-flux, eddy kinetic energy, and $\sigma = 0.967$ potential temperature. σ-levels are used in atmospheric models as a terrain-following vertical coordinate (*Warner*, 2011b). In this thesis, similar variables were chosen to facilitate comparison with results from THM93. Since WRF uses η-levels instead of σ, we have chosen 850hPa as our close-to-surface comparison for potential temperature. We have also included wind at 200hPa to provide a clearer picture of how the upper-level wind evolves over time.

3.1 Synotic evolution of D-LC1 and D-LC2

When adding a tangent hyperbolic shear to the zonal mean wind, the anticyclonic behavior of LC1 and cyclonic behavior of LC2 in our dry experiments (D-LC1 and D-LC2) exhibit similarities with THM93. Consistent with THM93, D-LC1 generates extensive surface high-pressure systems while D-LC2 produces large, circular low-pressure systems. In the following section, we examine the synoptic evolution of D-LC1 and D-LC2 and compare them to THM93.

3.1.1 D-LC1

Day 4:
By day 4, the surface anticyclones in D-LC1 grow faster compared to the surface cyclones (figure 3.1a). A dent in the isobars, located north of the anticyclones, suggests cyclogenesis, but there is no strong development at this stage. The 850hPa potential temperature field displays warm air moving northward and cold air moving southward, forming a slightly northeast-southwest (NE-SW) tilted wave of the temperature contours, with a stronger gradient on the western side (figure 3.2a). The initial stages of D-LC1 are somewhat different from THM93's observations. While THM93 also observes the development of anticyclones by day 4 in their study, their surface cyclones have developed to approximately the same extent as their anticyclones (figure 6 from THM93). THM93 also observe northwest-southeast (NW-SE) tilt of the 2PVU potential temperature contours (figure 7 from THM93). The low-level potential temperature contours have stronger gradients on the eastern side of the ridge where the warm front is located

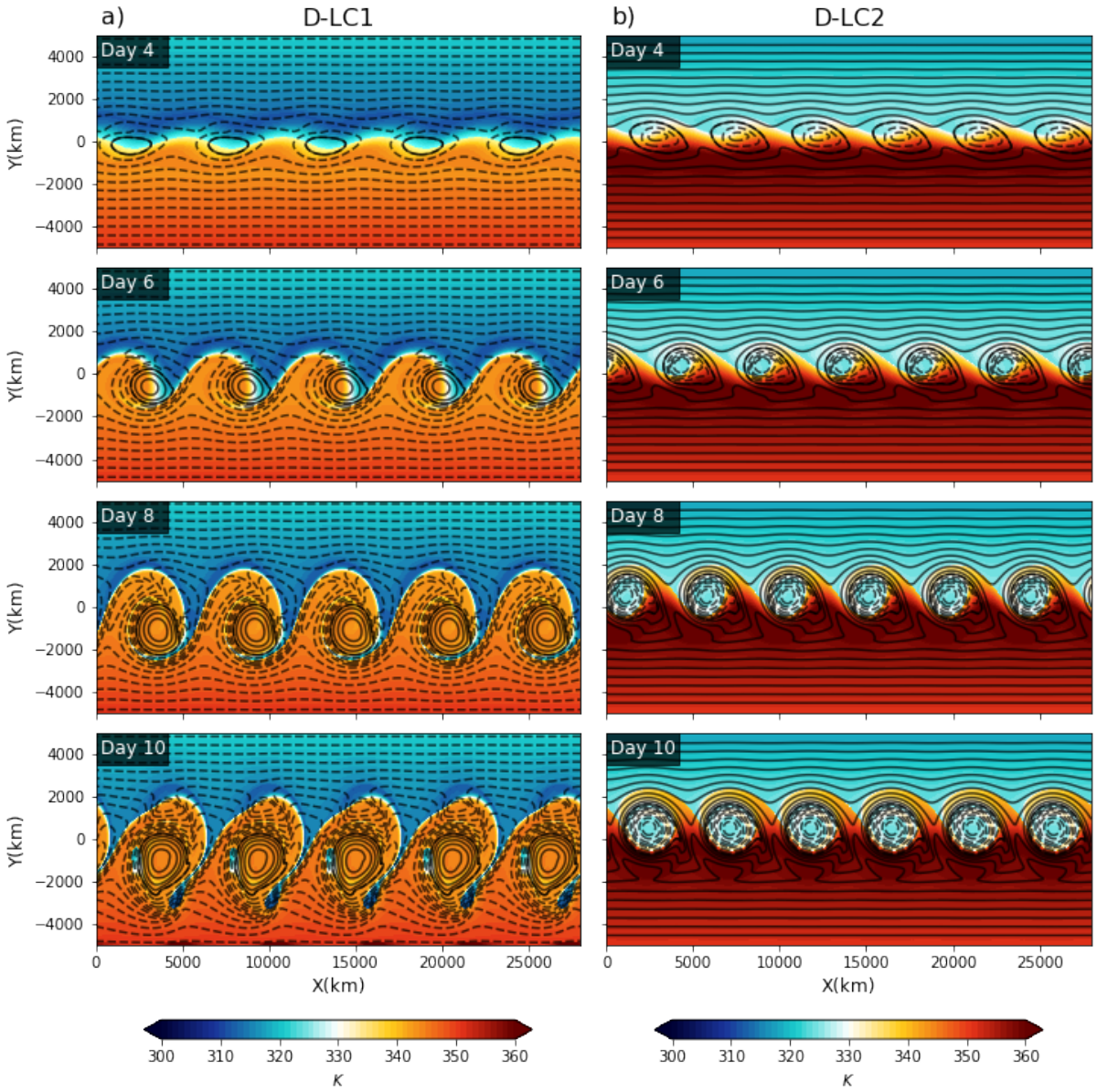

Figure 3.1: Surface pressure (black contours in hPa) and potential temperature on the PV = 2 PVU surface (shading in K) for a) D-LC1 and b) D-LC2. The contour lines are drawn at intervals of 5hPa, with the bold contour line representing the 1000hPa level. Dashed contours indicate pressure below 1000hPa and solid lines indicate pressure above 1000hPa.

(figure 5 from THM93). The behaviors of the upper and lower temperature fields resemble the characteristics of cyclonic motion, while the behaviors of D-LC1 resemble the characteristics of anticyclonic motion. It is likely that the observed disparity in behavior, at this stage, is a result of the difference in zonal mean wind configuration between our experiments and THM93.

Day 6:

By day 6, the 2PVU potential temperature field shows a distinct NE-SW tilted wave pattern with relatively warm air moving northward (figure 3.1a). The surface anticyclones continue to grow and are circular in shape, moving slightly westward without changing their meridional placement. The 850hPa potential temperature contours show increased

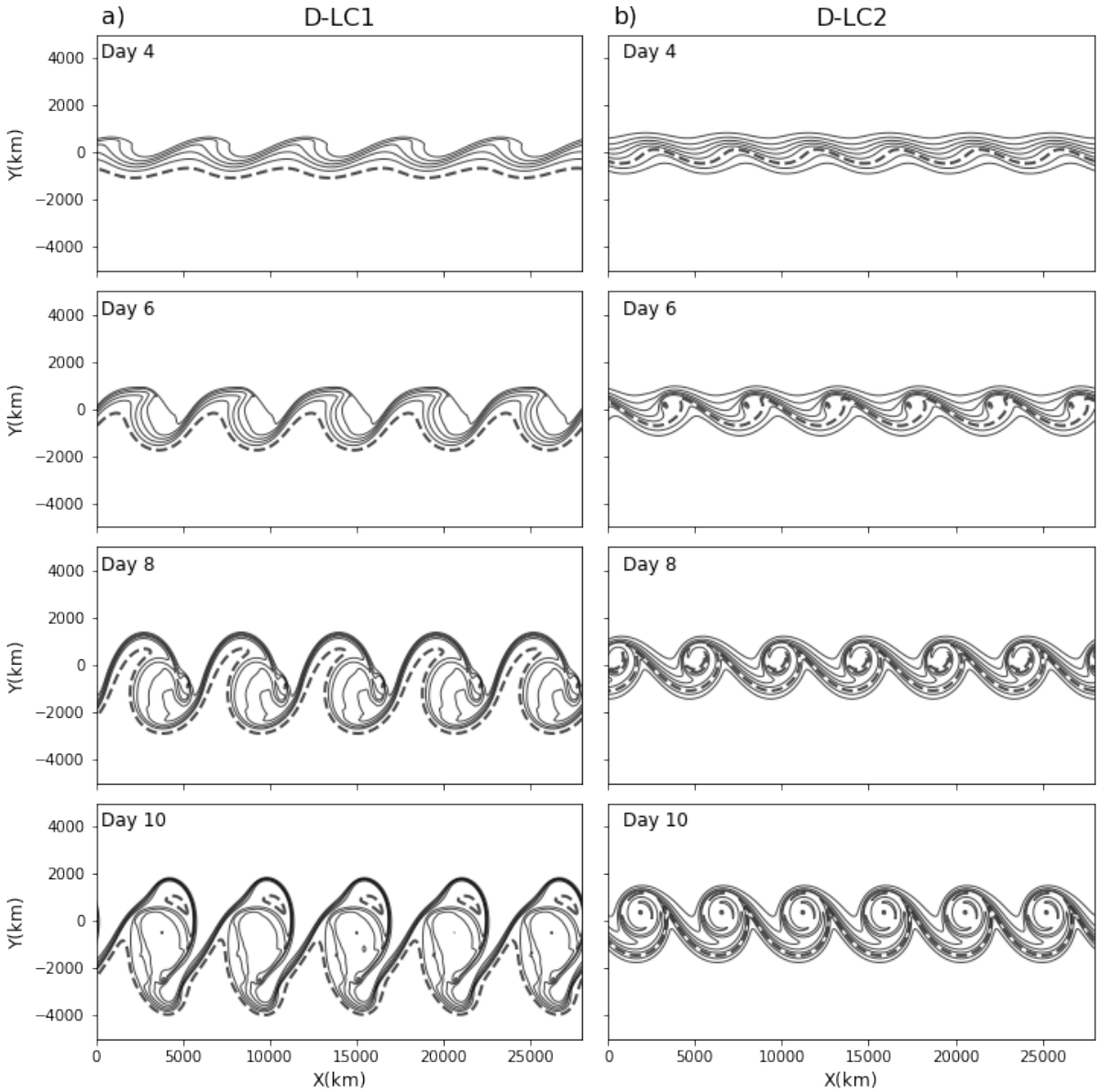

Figure 3.2: Potential temperature (contours in K) at 850hPa for a)D-LC1 and b)D-LC2. The contour lines are drawn at intervals of 5K, with the stippled contour line representing the 300K contour.

gradients on the western side of the wave, which has started to turn counterclockwise (figure 3.2a). We observe the 200hPa wind transitioning from predominantly westerlies to curving northward (figure 3.3a), with low pressures positioned north of the northward wind flow and high pressures positioned to the south of the curve. THM93 observe NW-SE-tilted potential temperature contours on the 2PVU surface, which have started to turn and become parallel to the cold front of surface cyclones moving towards an anticyclonic trajectory (figure 7 from THM93). The surface cyclones have moved northward, while the anticyclones are becoming circular. At day 6, the placement of D-LC1 surface cyclones resembles the location and shape of THM93's cyclones (figure 6 from THM93).

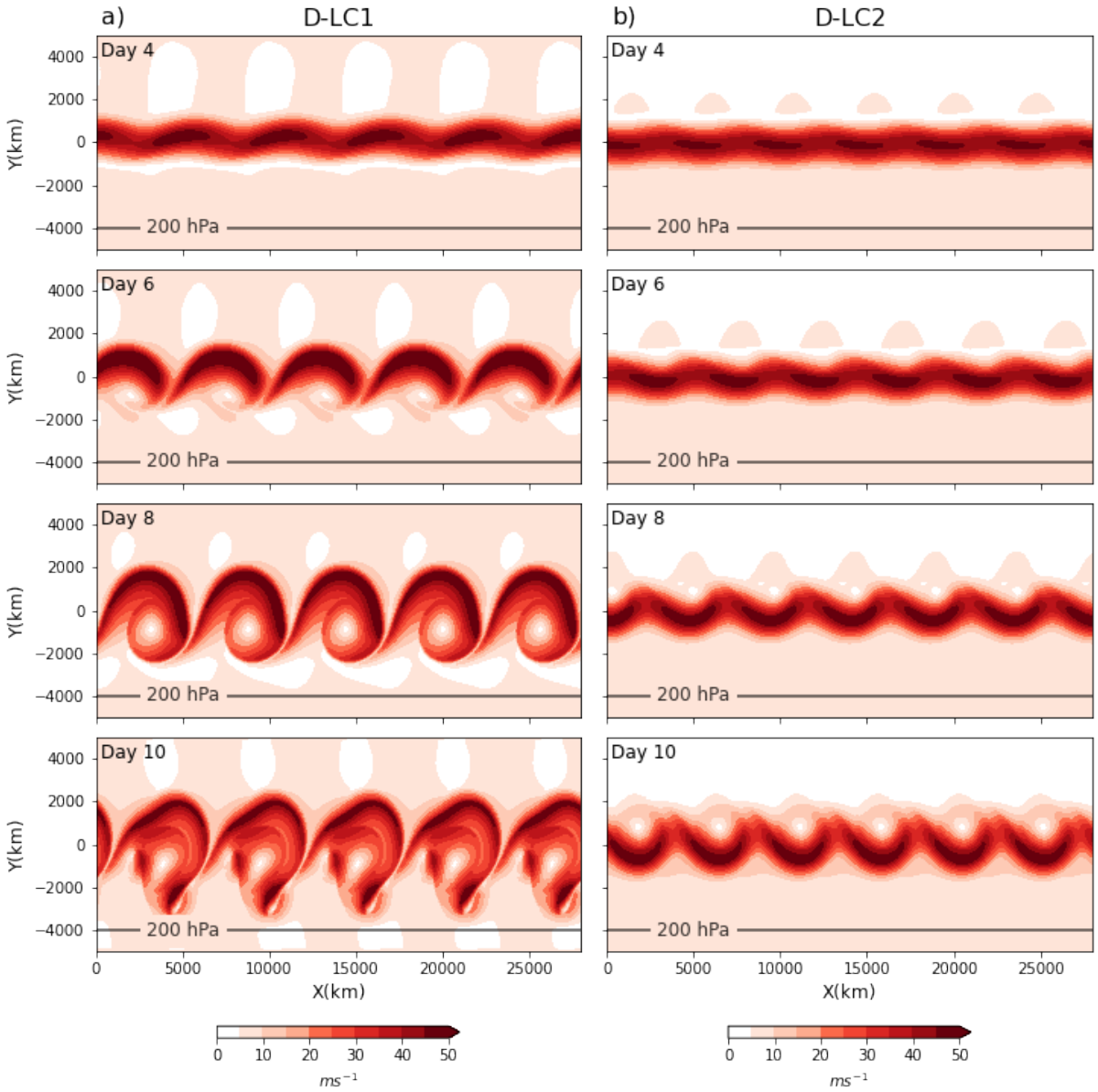

Figure 3.3: Total wind speed at 200hPa (shading in ms^{-1}) for a) D-LC1 and b) D-LC2

Day 8:
On day 8, the surface high-pressure systems continue to strengthen and become more circular in shape. The low-pressure surface systems are still in the early stages of development, with the relatively cold and warm air along the front starting to turn cyclonically (figure 3.1a). The curving of the upper-level wind continues to move northward, causing the surface cyclones to shift northward as well (figure 3.3a). At this point, the 2PVU potential temperature surface exhibits distinct anticyclonic motion with an elongated NE-SW tilted wave and narrowing troughs. The 850hPa potential temperature field also shows very strong gradients on the western side of the ridge (figure 3.2a). At this stage in the evolution of THM93's LC1 simulation the surface, cyclones have already secluded and broken off from their warm source in the south (figure 5 from THM93). However, the cyclones in D-LC1 develop at a slower pace, and therefore the seclusion does not happen until a later time step in D-LC1. Additionally, the anticyclones in THM93's simulation has grown so large that they begin to merge with each other (figure 6 from THM93),

and the ridges of warm air on the 2PVU surface almost cut off the cold troughs (figure 7 from THM93). This also occurs in D-LC1 but at a later stage.

Day 10:
On day 10, we observe the first clear anticyclonic motion in the northern part of the domain ($y = 2000km$) with the potential temperature contours turning anticyclonically (figure 3.2a). The 2PVU potential temperature field shows that the warm air ridges in the north are now cutting off the cold air troughs to the south. In THM93's LC1 simulation, the mid-latitude baroclinicity is already mostly destroyed, and surface pressure is becoming more zonal (figure 6 from THM93). This occurs at a later time in D-LC1. While D-LC1's development is slower, it shares a common feature with THM93, namely the presence of a second frontal cyclone on the cold front to the south ($y = -3000$ in figure 3.1a, figure 5 from THM93).

Although it is not shown in the figures that are included here, some of the features observed by THM93 between day 8 and 10 can be seen in D-LC1 between day 12 and 14. For instance, the warm air ridge on the 2PVU surface cuts off the relatively cold air between day 10 and 12. The cold front eventually catches up with the warm front, cutting the warm air from the south between day 12 and 14. Additionally, the anticyclones start merging, and the isobars become more zonal between day 12 and 14. Notably, the development of surface cyclones is much slower in D-LC1 compared to THM93. This could be attributed to the anticyclonic wind shear at the surface of the zonal mean wind throughout the domain in D-LC1 (figure 2.1a), while THM93 have cyclonic surface shear in the northern domain and anticyclonic shear in the southern domain (figure 1.4a)

EP-flux

In the first 5-6 days of the simulation, the EP-fluxes are predominantly vertical (figure 3.4a). This indicates that the EP-flux vectors are dominated by heat-flux and we experience baroclinic growth. By day 8, the arrows in the southern upper troposphere are starting to turn southward, indicating a shift towards momentum flux domination in this region, although there are still areas with mostly vertical arrows. On day 10, the arrows are mostly horizontal, pointing southward across the entire domain, indicating that we are transitioning into the barotropic decay phase. Southward-pointing arrows signify northward momentum flux, which corresponds well with the northward shift of the jet shown in figure 3.5a.

The contours of EP-flux divergence in figure 3.4a are consistent with the zonal mean zonal winds in figure 3.5a. From day 4 to day 6, there is a deceleration of zonal winds throughout the entire depth of the atmosphere and the convergence of EP-fluxes in figure 3.4a at $y = 0$ from the surface to the tropopause. Additionally, there is convergence at the surface near $y = -1000$km, which corresponds to a strengthening of the easterlies in that region. In figure 3.5a, the jet is seen to accelerate between $y = 1000$km and 2000km while further decelerating between 0 and 1000km, further indicating a northward shift of the jet.

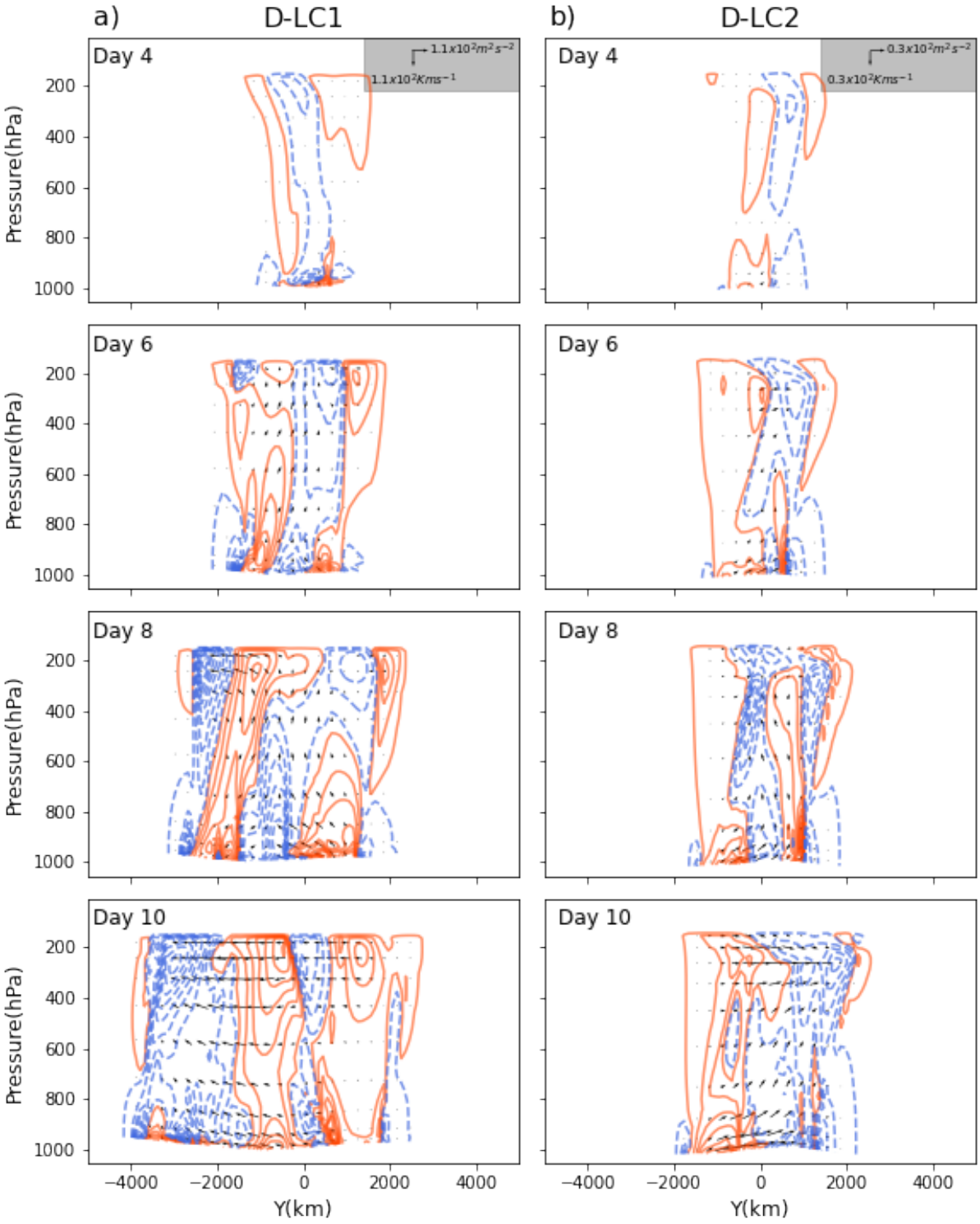

Figure 3.4: EP-flux (arrows, where the vectors are in m^2s^{-2} (momentum flux) and Kms^{-2} (heat flux)) and its divergence (contours in ms^{-2}) for a) D-LC1 and b) D-LC2. The divergence is multiplied by 400. Solid red contours denote the flux divergence giving eastward flow acceleration. Dashed blue contours denote the flux convergence giving eastward flow deceleration. Contour interval is $10ms^{-2}$.

Due to differences in our initial wind profile (figure 2.1) from THM93 (figure 1.4), there are some disparities in the EP-flux divergence contours. On day 5, THM93 observes a convergence of the EP-fluxes between 30°N and 60°N, from the surface to the tropopause, corresponding to the initial position of their jet (figure 15 from THM93). Our results show the deceleration of the jet, which is consistent with their findings. However, we observe an additional acceleration of zonal mean wind at $y = 1000$km in the upper troposphere, which is not present in THM93. This discrepancy is likely due to the shear we have added, which induces easterlies throughout the entire troposphere on the northern side of the main jet, which is not present in THM93's LC1 zonal mean wind. On day 8 and day 10, both THM93 and our simulation exhibit a deceleration on the southern side and acceleration on the northern side of the jet, indicating a northward shift of the jet.

Energetics

Inspection of EKE is consistent with our EP-flux analysis. In fact, in the time period between day 4 and 8, we observe a steep increase in EKE, in agreement with the large contribution from the heat fluxes to the EP-fluxes vectors (figure 3.6). Following day 8, EKE levels off. The period between day 9 and 10 is characterized by a negative slope in the D-LC1-EKE curve, indicative of a barotropic decay phase, which is also supported by the mostly horizontal EP-flux vectors.

The general shape of the D-LC1-EKE curve is similar to that of THM93's EKE curve for LC1 (figure 4 from THM93), with both exhibiting a period of baroclinic growth followed by barotropic decay. However, there are several significant differences between the two. For example, THM93's LC1 reaches peak EKE levels on day 7, while D-LC1 does not reach peak EKE levels until day 10. Additionally, the EKE in THM93 features a steeper slope compared to D-LC1. These differences can be attributed to the differences in the synoptic evolution between the two simulations, with the surface cyclones developing much later in D-LC1 than in THM93.

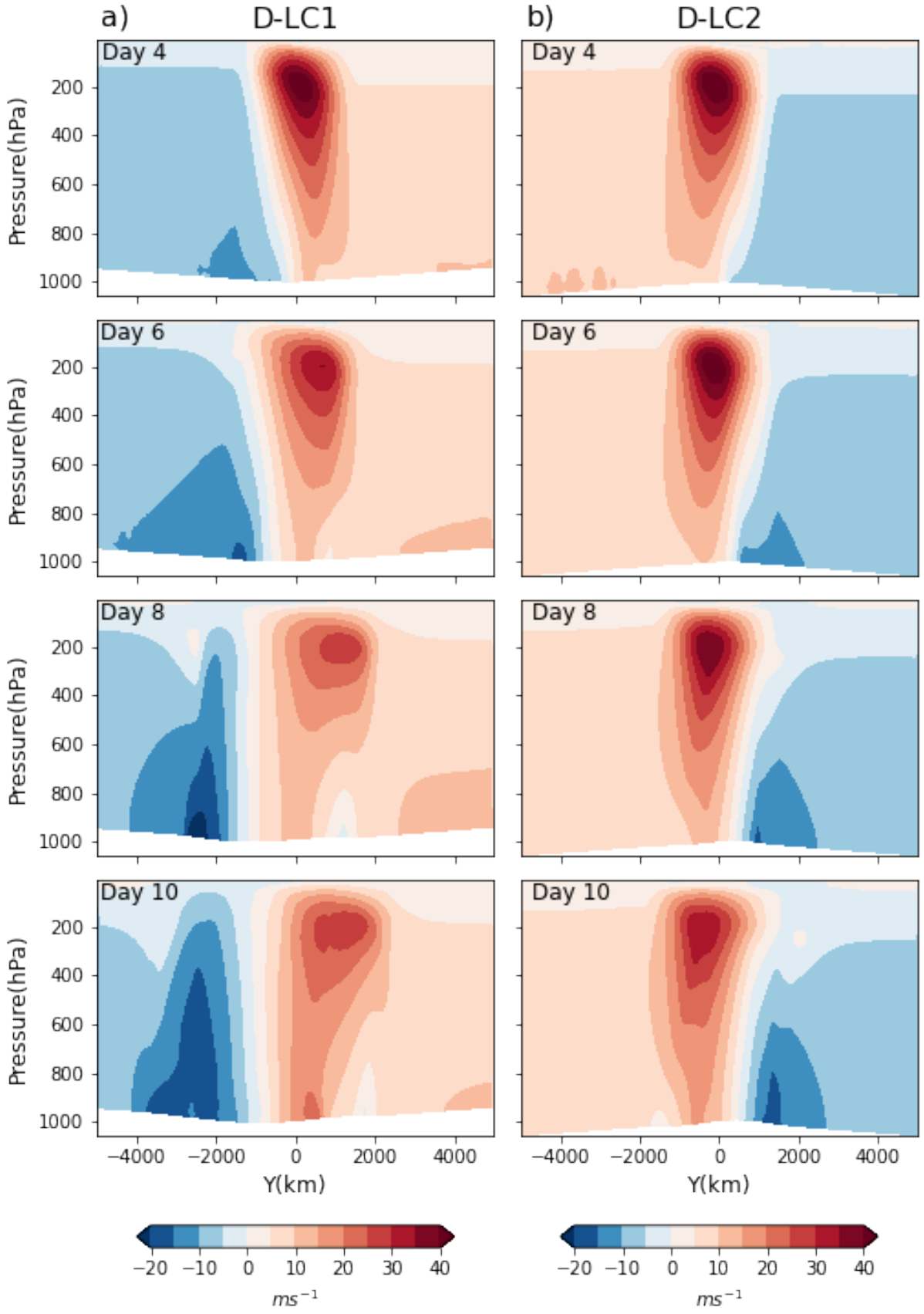

Figure 3.5: Zonal mean zonal wind (shading in ms^{-2}) for a) D-LC1 and b) D-LC2

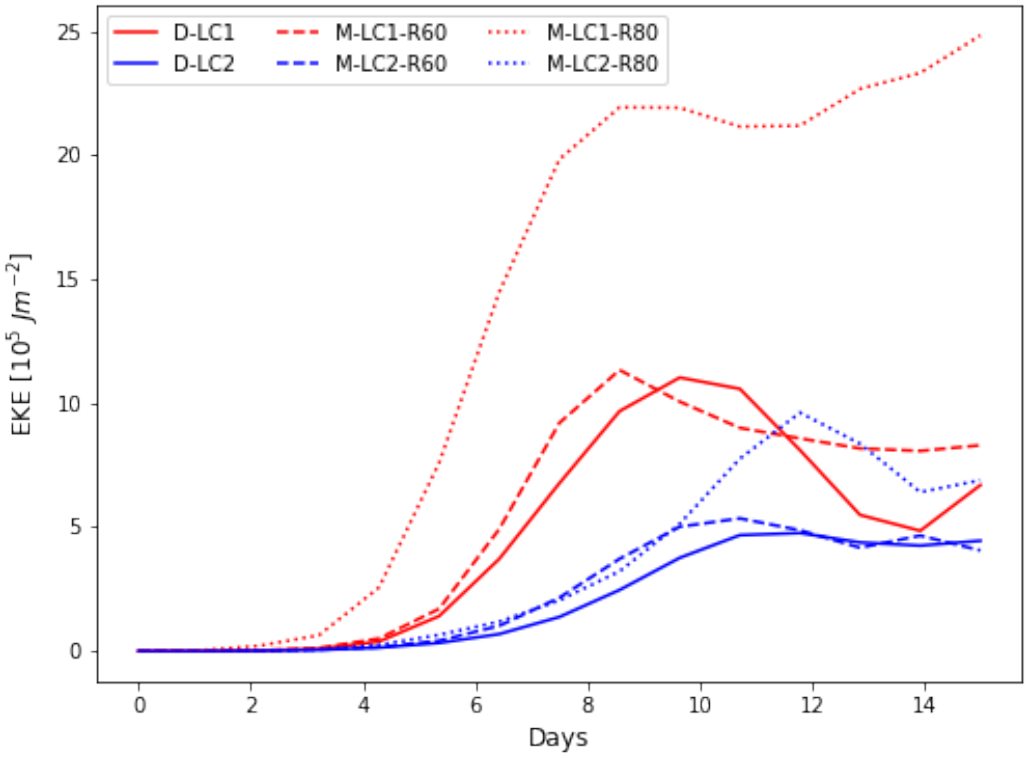

Figure 3.6: Eddy kinetic energy ($10^5 Jm^{-2}$) for modal perturbed experiments.

3.1.2 D-LC2

Day 4:
In contrast to D-LC1, D-LC2 exhibits surface cyclones developing on day 4 (figure 3.1b). At the 850hPa potential temperature field, a NW-SE tilted wave with stronger gradients on the eastern side develops, (figure 3.2b). This wave is also visible at the 2PVU potential temperature field, created by the strong cyclonic shear in figure 3.1b. The characteristics of D-LC2 on day 4 are quite similar to THM93 with the predominantly cyclone development and NW-SE tilt of the potential temperature fields. We observe a minimum surface pressure of 995hPa by day 4, while THM93 experience a minimum pressure of 984hPa. At this point in time, without having knowledge of the initial pressure field, it is impossible to determine whether this is a result of slower cyclone development or variation in initial surface pressure.

Day 6:
On day 6, the relatively cold air is moving southward and rotating westward, while the relatively warm air is moving northward and rotating eastward creating a counter-clockwise rotating of the upper-level air (figure 3.1b). The surface cyclones in D-LC2 reach a minimum pressure of 985hPa and the gradient on the eastern side of the 850hPa potential temperature field ridge becomes stronger (figure 3.2b). On day 6, THM93's surface lows have reached a minimum pressure of 952hPa (figure 9 from THM93). Between day 4 and 6, the surface cyclone in D-LC2 intensify with about 10hPa while THM93 ob-

serve an intensification of about 39hPa. This indicates slower growth of surface lows in D-LC2 compared to THM93.

Day 8:
On day 8, a circular pattern is formed as relatively warm air rotates at both the 850hPa and the 2PVU surface (figure 3.2b, figure 3.1b). In comparison to D-LC1, which has narrowing troughs of relatively cold air at the 2PVU surface, D-LC2 exhibits more zonally wide and meridionally confined troughs (figure 3.1b). The 850hPa potential temperature contours take a circular shape and the surface cyclones continue to expand and intensify (figure 3.1b). In figure 3.3c, the upper-level wind has hardly moved from its initial position at $y = 0$, suggesting that the surface cyclones in the LC2 lifecycle do not move much meridionally, but expand to a much greater horizontal width than the surface cyclones in D-LC1. Up to this point in time, the characteristics of THM93's LC2 experiment is a few timesteps ahead of D-LC2. THM93's cold front has caught up with the warm front, and warm air is being secluded in the center of the cyclone (figure 8 from THM93). However, the frontal regions are still connected to the northern part of the wave.

Day 10:
On day 10, the fronts are occluding, (figure 3.2b). At this point, the cyclone is still connected to its source of warm air in the south, and the wind has only curved slightly more to the south, resulting in minimal meridional movement of the cyclones (figure 3.3c).

Similar to D-LC1, the characteristics of THM93's LC2 on days 7 to 9 are observed in the following days for D-LC2. By day 12, the surface cyclones have cut off their connection to the warm air source in the south, but there is still warm air secluded in the center of the cyclones. The potential temperature on the 2PVU surface indicates that relatively warm air continues to wrap up cyclonically. The large-scale vortices observed in the 2PVU potential temperature field are persistent and last for an extended period. In summary, despite being a few timesteps behind in the synoptic evolution, the lifecycle of D-LC2 shows similar characteristics to THM93's LC2 experiments.

EP-flux

The amplitude of D-LC2 EP-fluxes is weaker compared to D-LC1, and similar to D-LC1, the EP-fluxes do not become apparent until day 6 (figure 3.4b). Unlike D-LC1, where the heat fluxes dominated the entire domain, D-LC2 shows a combination of momentum and heat fluxes. In the mid-troposphere, heat fluxes dominate the EP-fluxes, while in the upper troposphere, momentum fluxes are dominant giving southward momentum flux(northward-facing arrows). On day 10, the northward-facing horizontal arrows in the upper troposphere are stronger, indicating southward momentum flux, which corresponds well with the jet moving slightly southward (figure 3.5b).

EP-flux divergence, shown in figure 3.4b is visually well correlated with the zonal wind (figure 3.5b). On day 4, we observe convergence on the northern side of $y = 0$ and divergence on the southern side at the surface (figure 3.4b). Below 700hPa, the zonal mean wind on the northern side of $y = 0$ becomes stronger easterlies, while on the southern

side, the surface westerlies become more intense (figure 3.5b). The EP-flux divergence shown in figure 3.4b is primarily on the southern side of $y = 0$, with convergence on the northern side. This pattern is evident on days 8 and 10 as well. The density of the EP-flux contours is not as high as in figure 3.4a, indicating that the changes in the zonal mean zonal wind are less pronounced in D-LC2 than in D-LC1.

Energetics

In figure 3.6, the EKE of D-LC2 exhibits significant differences from THM93 (figure 4 from THM93), as well as from other studies on LC1 and LC2 (*Polvani and Esler*, 2007; *Jäger et al.*, 2023). According to these studies, the EKE for LC2 should peak at a later timestep and reach higher values compared to LC1. Although D-LC2 attains its maximum EKE between day 10 and 12, after D-LC1 reaches its peak EKE levels, its EKE curve lies significantly below D-LC1's curve, which is unexpected. One possible explanation for this difference is that the D-LC2 cyclones intensify much more slowly compared to THM93's LC2 lifecycle. Furthermore, the EKE of D-LC2 does not exhibit the same degree of decay as D-LC1, suggesting that the barotropic decay mechanisms acting in D-LC1 are not as active in D-LC2. This observation is also supported by figure 3.4c, which shows that the EP-fluxes are significantly smaller in D-LC2 compared to D-LC1.

3.2 Synoptic evolution of M-LC1 and M-LC2

In the following section, we explore the effect moisture has on the two paradigms LC1 and LC2.

3.2.1 M-LC1

Day 4:
On day 4 of the experiment, M-LC1-R60 exhibits the growth of surface anticyclones without any clear evidence of cyclone development (figure 3.7a). The warm air is transported towards the north and the cold air is transported towards the south at the frontal zones, creating a wave pattern of the potential temperature contours, with stronger gradients on the western side of the ridge, resulting in an anticyclonic motion of the potential temperature field (figure 3.8a). Although the upper-level wind still appears almost zonal, it has a slight northward curve (figure 3.9a). There are no distinctive differences between M-LC1-R60 and D-LC1 until this point in time and the synoptic evolution is identical. It will take some time before the air becomes saturated enough for water vapor to condense and for microphysical processes to come into effect, leading to a similar evolution between the two experiments in the beginning stages.

By day 4, we observe the asymmetrical development of cyclones and anticyclones in M-LC1-R80, where the individual systems exhibit varying zonal widths between each other (figure 3.7b). Additionally, their growth rate differs. In comparison, D-LC1 and M-LC1-R60 experience symmetric development, where the five individual systems of cyclones and anticyclones have the same growth rate and develop with the same constant zonal width between each other (figure 3.1a and figure 3.7a). To achieve the symmetry

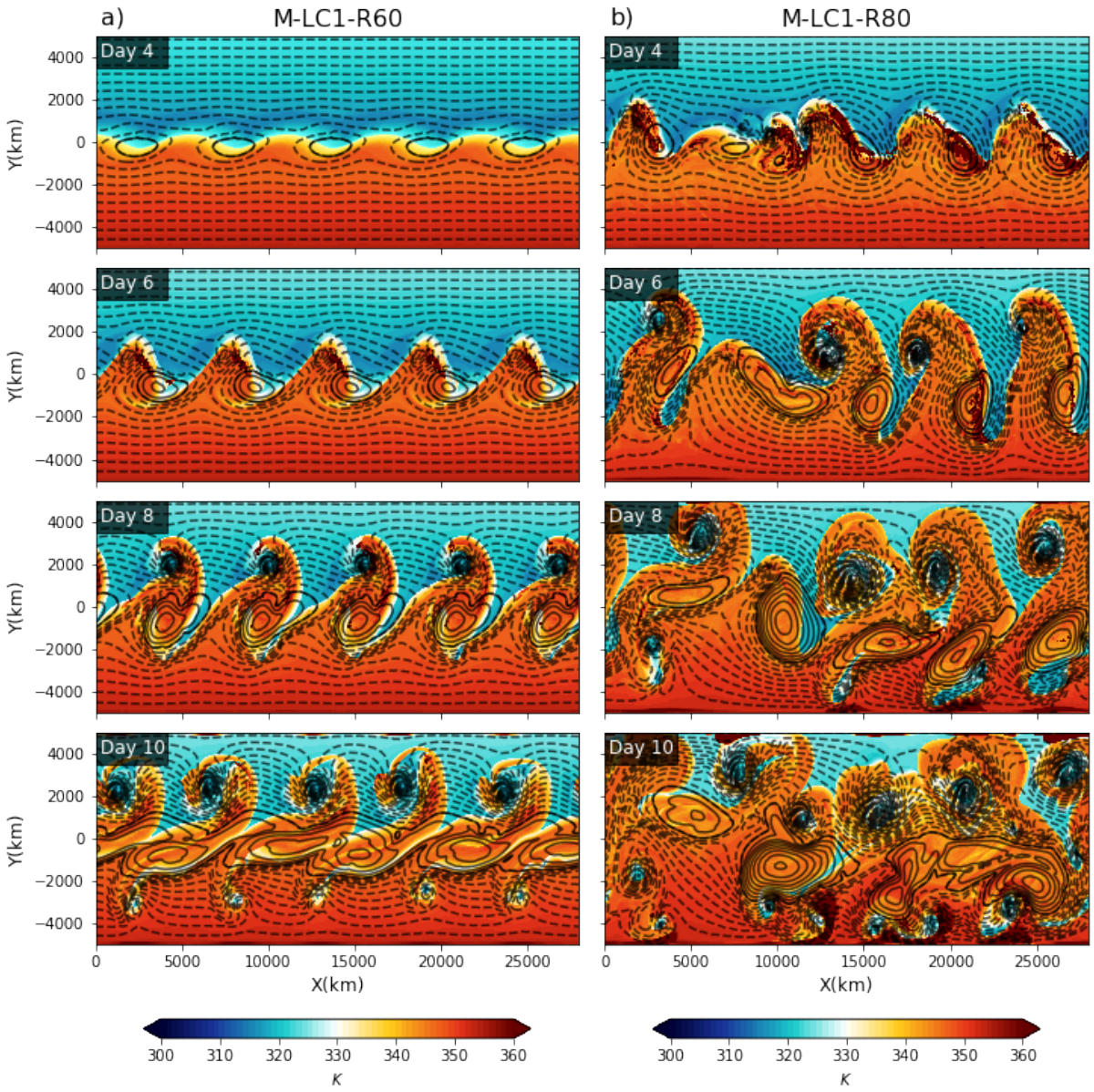

Figure 3.7: Surface pressure (black contours in hPa) and potential temperature on the PV = 2 PVU surface (shading in K) for a) M-LC1-R60 and b) M-LC1-R80. The contour lines are drawn at intervals of 5hPa, with the bold contour line representing the 1000hPa level. Dashed contours indicate pressure below 1000hPa and solid lines indicate pressure above 1000hPa.

in D-LC1, an initial zonal wavenumber of $k = 5$ for the modal perturbation is selected. With some adjustment to the zonal wavenumber, it may be possible to acquire symmetry for M-LC1-R80. The surface anticyclones still have the largest horizontal radius, however, cyclogenesis appears to the west of these highs already on day 4. This occurs much earlier compared to D-LC1, where the same structure of surface lows does not appear until day 8. M-LC1-R80 starts with an initial surface RH of 80%, which allows the atmosphere to reach saturation at an earlier time step and enhances the impact of microphysical processes. The placement of the lows on day 4 is similar to THM93 (figure 6 from THM93), with the lows placed to the north-east of the highs before moving northward at a later time step. The 2PVU potential temperature field reveals relatively warm air moving northward, creating an uneven wave pattern of the contours without a clear tilt as observed in D-LC1 and M-LC1-R60 on day 4 (figure 3.7b). The same applies to the wave pattern of the 850hPa potential temperature contours (figure 3.8b).

In M-LC1-R80, there are five cyclones and anticyclones developing. The second systems (anticyclone and associated cyclone), viewed from the left side of the domain, are becoming increasingly asymmetric compared to the first and last three systems (figure 3.7b). The position of the second cyclone is closely connected to the upper-level wind (figure 3.9c), which is also causing the surface anticyclones to become elliptical in shape instead of circular. Surface cyclones are explosively growing to the northwest of the surface highs, fueled by latent heat release. The 2PVU potential temperature field shows a meridionally elongated wave turning cyclonically (figure 3.7b). The development of the upper troposphere is connected to the surface development, so ridge tops, of the temperature contours, that have turned more show stronger surface cyclone development. The 850hPa potential temperature field shows strong gradients on both the cold and warm fronts (figure 3.8b), with the cold front catching up to the warm front and occluding. Since the surface cyclones are displaced far north, they bring moisture from the south following the warm conveyor belt (figure 3.8b). It is the cyclonic motion of the potential temperature field and explosive growth of surface lows that differentiate M-LC1-R80 from D-LC1. One hypothesis to consider is that diabatic heating enhances the baroclinicity of the atmosphere, leading to intensified cyclone growth. however, additional research is required to determine if this is the case.

Day 8:
On day 8 of M-LC1-R60, there is a narrowing of the 2PVU potential temperature filaments of cold air, which is indicative of anticyclonic motion (figure 3.7a). However, at the same time, there is also a cyclonic motion of the ridges. Both the surface anticyclones and cyclones have intensified, with the surface highs remaining at $y = 0$, while the surface lows have shifted about 1000km north, in agreement with the shape of the 2PVU potential temperature field. The 850hPa potential temperature field shows that the cyclones have separated from their warm source in the south, but some warm air remains confined to their cores (figure 3.8). The upper-level wind has split into a northward and southward flow (figure 3.9a), with the northward flow having a NW-SE tilt and the southward flow stretching meridionally and curving eastward. Unlike D-LC1, where the 2PVU potential temperature field showed a narrow trough turning westward anticyclonically, M-LC1-R60 exhibits narrow troughs that do not turn westward to the same degree. This could be due to the presence of a second frontal cyclone along the

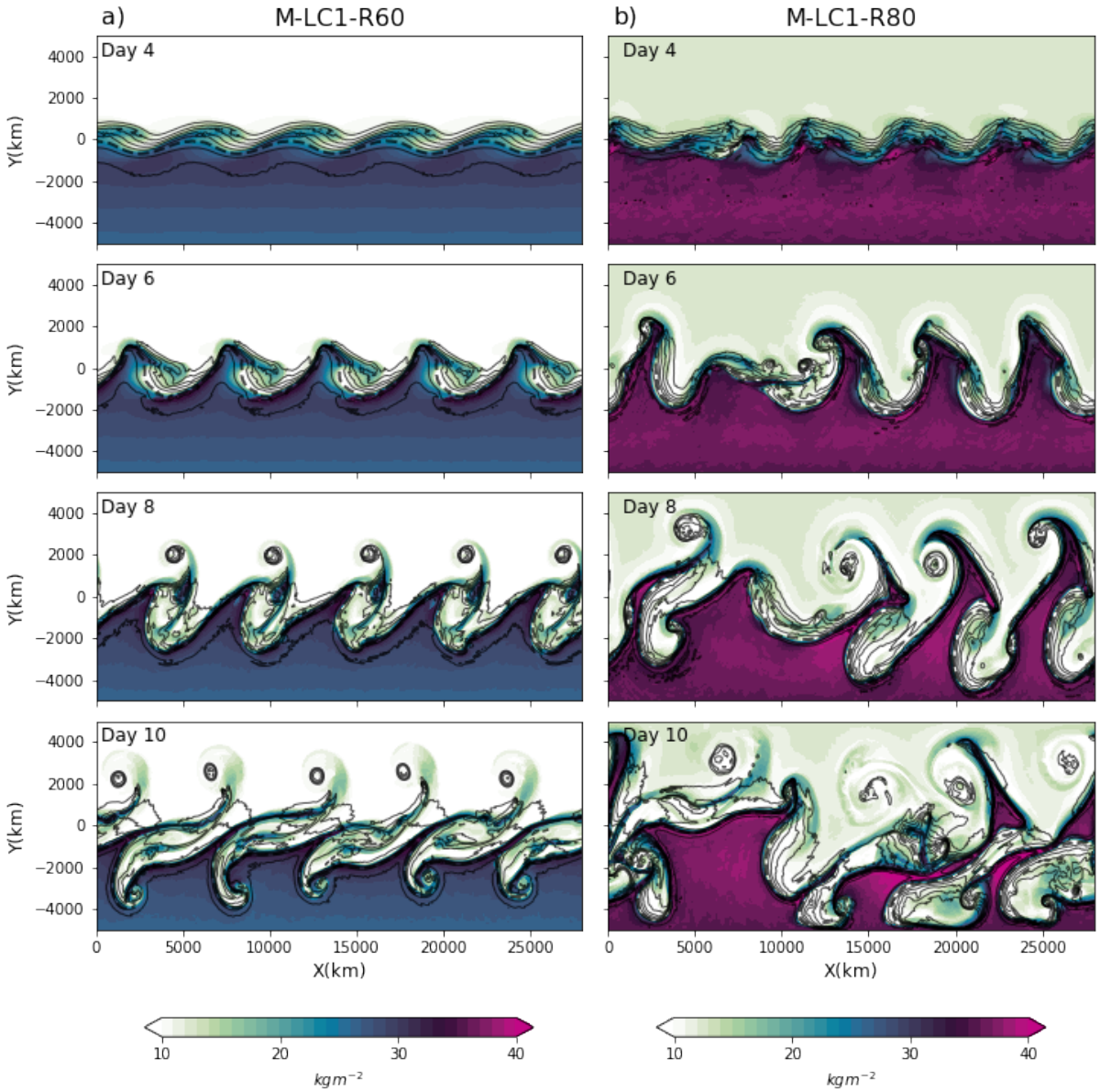

Figure 3.8: Potential temperature (contours in K) at 850hPa and TCWV (shading in kgm^{-2}) for a)M-LC1-R60 and b)M-LC1-R80. The contour lines are drawn at intervals of 5K, with the stippled contour line representing the 300K contour.

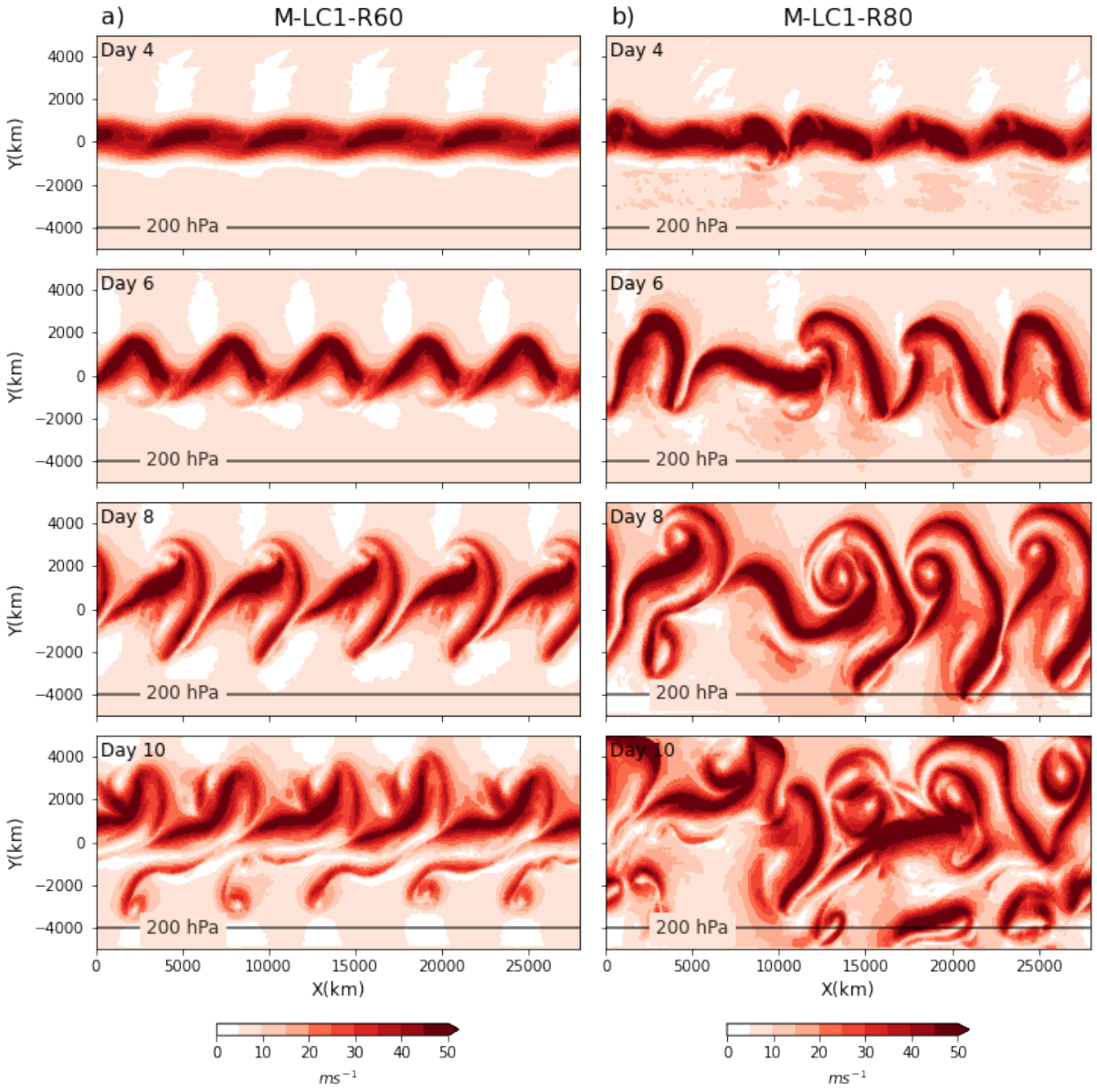

Figure 3.9: Total wind speed at 200hPa (shading in ms^{-1}) for a) M-LC1-R60 and b) M-LC1-R80

cold front to the south (figure 3.7a), as discussed in the previous paragraph. As seen on day 6 of M-LC1-R80, the addition of moisture intensifies cyclone growth.

On day 8 of M-LC1-R80, the 2PVU potential temperature field display a two-part wave in the contours. The southern segment is inclined to the east, with narrow troughs of relatively cold air wrapping up anticyclonically. Meanwhile, the northern section is slanting westward, wrapping up cyclonically around the low-pressure system (figure 3.7b). The surface anticyclones continue to expand and turn zonally, while the surface cyclones keep expanding as well (figure 3.7b). The 850hPa potential temperature indicates that the cyclones are cut off from their warm source in the south (figure 3.8b). Additionally, the TCWV field depicts water vapor transported in a meridionally enlongated path (figure 3.8b). The moisture wraps more around the cyclone, transporting the water vapor much farther north compared to M-LC1-R60.

Day 10:
On day 10 of M-LC1-R60, the surface anticyclones have shifted, creating almost zonal isobars, while the cyclones have intensified but remain stationary in their position (figure 3.7a). A second frontal structure is growing close to the southern boundary. The relatively warm potential temperatures and TCWV field are extended, creating a zonal band (figure 3.8a). The upper-level wind has moved northward by about 1000km since day 8 and now collides with the northern boundary (figure 3.3a). The southward flow seen on day 8 is mostly destroyed, leaving behind the northward flow of the upper-level wind. The turning of the surface anticyclones and the emergence of a second frontal structure is comparable to what we see in D-LC1. However, the addition of moisture with $RH = 60\%$ intensifies the surface cyclones development, which occurs at a much earlier stage compared to D-LC1.

M-LC1-R80 has a higher saturation rate and more water vapor than M-LC1-R60, providing more energy to the system in the form of diabatic heating from latent heat release. As a result, the upper-level wind and cyclones collide with the northern boundary after day 8 (figure 3.9b, figure 3.7b). By day 10, the atmosphere becomes chaotic and is affected by the feedback from colliding with the boundary, making it difficult to predict how the system will develop between day 8 and 10. However, if the surface cyclones had not collided with the boundaries and maintained better symmetry, the anticyclone would likely form a zonal band similar to that seen in M-LC1-R60. Additionally, a second frontal structure would develop along the troughs of the 2PVU potential temperature field.

EP-flux

On day 4 of M-LC1-R60, the EP-fluxes are weak with no significant contribution from heat or momentum fluxes (figure 3.10a). By day 6, the arrows become almost vertical, indicating a greater contribution from heat flux, which continues to increase until day 8 when the arrows turn and point southward, indicating horizontal momentum fluxes. As the momentum flux is defined as downgradient, the momentum flux is directed northward. Between day 7 and 8, the system shifts from baroclinic growth to barotropic decay, with the momentum fluxes and resulting barotropic decay decreasing between day 8 and 10. Only the fluxes in the northern part of the domain remain, corresponding to the

meridional placement of the surface cyclones (figure 3.1a) on day 10.

On day 4, figure 3.10a shows a convergence of the EP-fluxes from the surface up to the tropopause at $y = 0$. A bit further north, we observe divergence in the upper troposphere. The convergence and divergence correspond to the shift in the zonal mean wind between day 4 and day 6 (figure 3.11a). On day 6, the convergence expands northward while the divergence area shifts northward and extends vertically towards the surface. The northward shift of the jet, as seen in the zonal mean wind on day 8 can be explained by the EP-fluxes. The strengthening and vertical stretching of the surface easterlies can also be explained by the convergence of the EP-fluxes.

Comparing the M-LC1-R60 experiment results to D-LC1, we can confirm our previous discussion on synoptic evolution. The evolution up to day 6 is similar between the two experiments, with a slightly higher contour density of EP-flux divergence in M-LC1-R60. However, the EP-fluxes in M-LC1-R60 are greater than the ones in D-LC1. The strong influence of momentum fluxes indicating barotropic decay seen on day 10 in D-LC1 is already present on day 8 in M-LC1-R60. Additionally, the northward shift of the jet is more pronounced in M-LC1-R60 compared to D-LC1. While D-LC1 had a 1500km northward shift of the jet after 10 days, M-LC1-R60 had a 2500km northward shift of the jet during the same period.

On day 4, M-LC1-R80 shows upper tropospheric horizontal arrows directed northward (southward momentum flux) (figure 3.10b). By day 6, we observe heat fluxes contribution at the surface and mid-troposphere with some contribution from the momentum fluxes in the upper troposphere. Between days 6 and 8, the arrows turn southward (northward momentum flux). While there is still some contribution from the heat fluxes, the momentum fluxes contribute more, particularly in the upper troposphere.

Regarding the EP-flux divergence, M-LC1-R80 exhibits mainly divergence on the southern part of the domain and convergence on the northern part of the domain on day 4 (figure 3.10b). The zonal wind indicates a significant reduction of the westerlies on day 6 (figure 3.11b). A second jet core emerges in the upper troposphere at $y = 2500km$, corresponding to the divergence of EP-fluxes in the upper troposphere accelerating the westerlies in this region. Over the next few days, there is more divergence of the EP-fluxes in the northern part of the domain, resulting in the jet strengthening further north. As previously mentioned, the surface cyclones collide with the northern boundary after day 8. Therefore, it appears that there is a southward shift of the jet on day 10, but this is likely due to the collision with the northern boundary.

Compared to M-LC1-R60 and D-LC1, M-LC1-R80 has contributions to the EP-flux vectors over the entire domain by day 6, while M-LC1-R60 and D-LC1 are more restricted to the middle of the domain (figure 3.10, figure 3.4). M-LC1-R60 and D-LC1 exhibit a clear transition from heat fluxes dominating the EP-flux vectors to momentum fluxes being the primary contributor, while the MCL140 transition is less distinct. The EP-flux divergence is generally intensified.

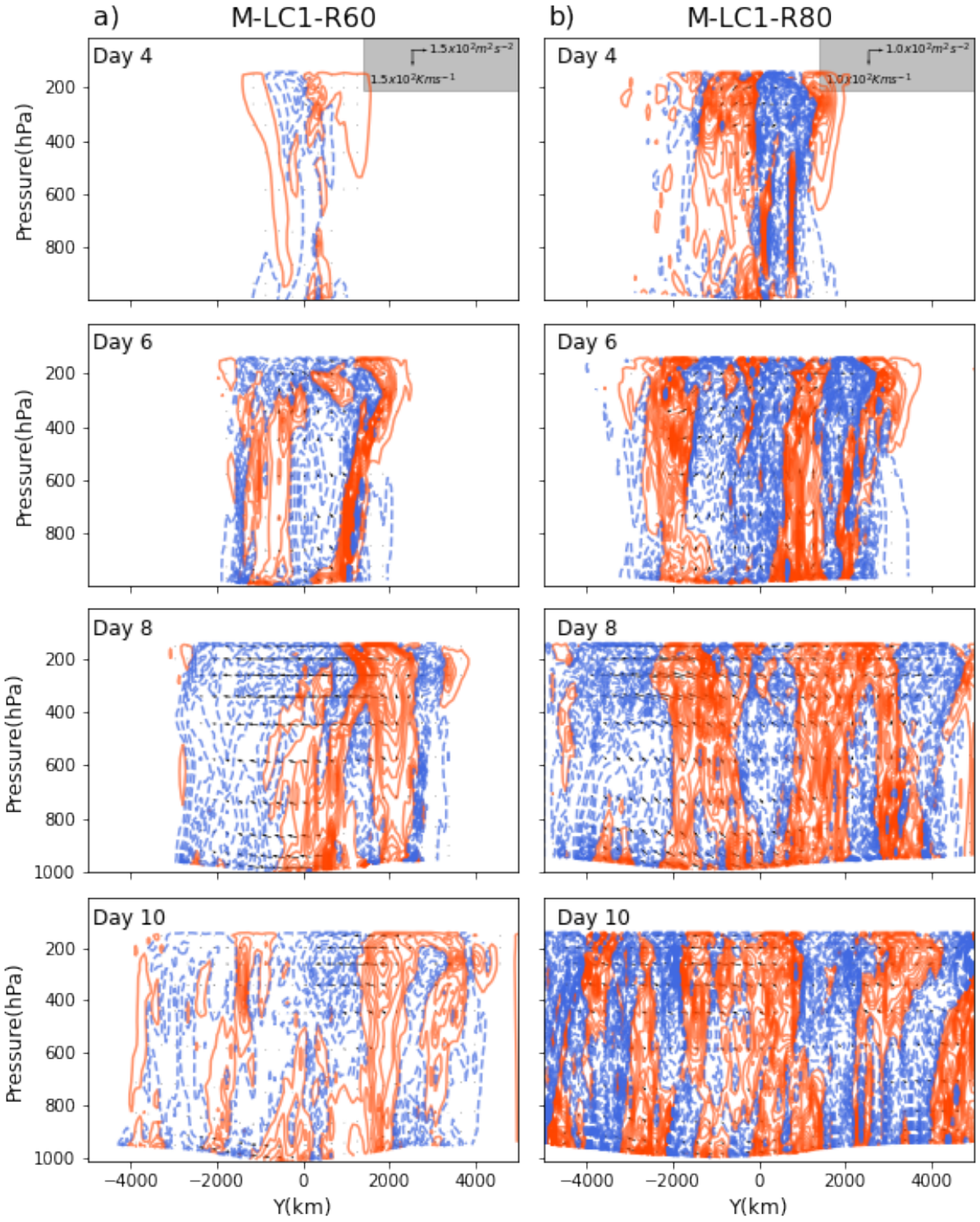

Figure 3.10: EP-flux (arrows, where the vectors are in m^2s^{-2} and Kms^{-2}) and its divergence (contours in ms^{-2}) and zonal mean zonal wind (ms^{-2}) for a) M-LC1-R60 and b) M-LC1-R80. The divergence is multiplied by 400. Solid red contours denote the flux divergence giving eastward flow acceleration. Dashed blue contours denote the flux convergence giving eastward flow deceleration. Contour interval is $10ms^{-2}$.

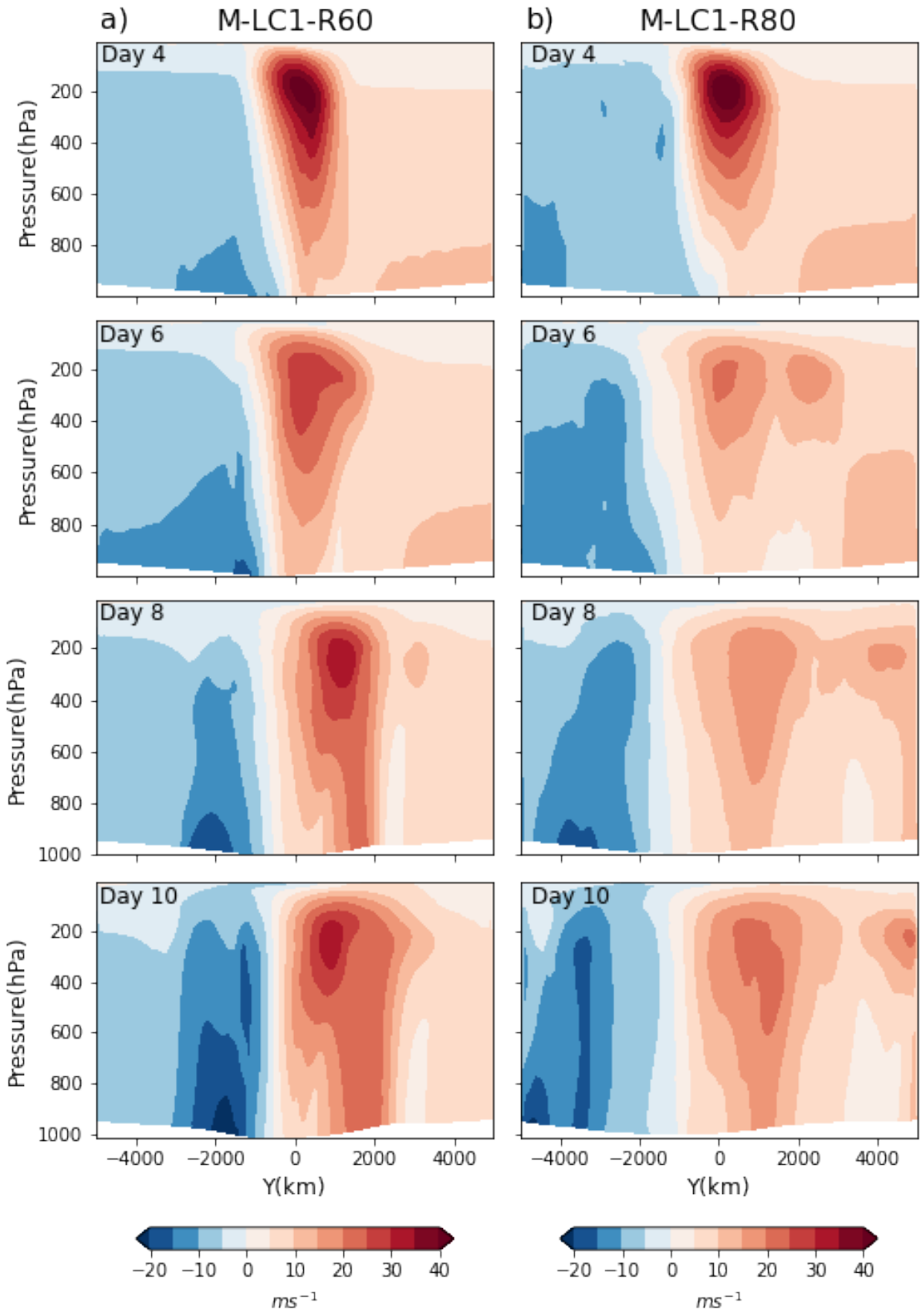

Figure 3.11: Zonal mean zonal wind (shading in ms^{-2}) for a) M-LC1-R60 and b) M-LC2-R80

Energetics

The EKE results shown in figure 3.6 support the findings from the EP-flux analysis. Until day 5, there is little difference in EKE between D-LC1 and M-LC1-R60. However, from day 6 onwards, the EKE of M-LC1-R60 increases faster compared to D-LC1, and the peak for M-LC1-R60 is reached approximately one day earlier. Despite reaching the peak earlier, the maximum value of EKE is approximately the same for both experiments. D-LC1 undergoes a gradual transition from baroclinic growth to barotropic decay over several days before the barotropic decay mechanisms become more active. In contrast, M-LC1-R60 undergoes a more rapid transition, with the barotropic decay mechanisms becoming more active from the start. The EKE for M-LC1-R60 levels off after day 10, which may be associated with the development of the frontal cyclone event observed in the south.

The EKE for M-LC1-R80 confirms a substantial increase in energy compared to M-LC1-R60 and D-LC1 (figure 3.6). Whereas the EKE levels for M-LC1-R60 and D-LC1 do not increase until after day 4, M-LC1-R80 shows an increase in EKE as early as day 2. By day 4, the conversion to EKE increases rapidly and reaches a peak level of approximately $22 \cdot 10^5 Jm^{-2}$, which is more than double the maximum value of M-LC1-R60 and D-LC1. Although M-LC1-R80 reaches the peak at the same time as M-LC1-R60, the barotropic decay is much less active. This is most likely due to the collision with the northern boundary.

3.2.2 MLC2

Day 4:
On day 4, M-LC2-R60 and M-LC2-R80 generate surface cyclones (figure 3.12). The 850hPa potential temperature field shows stronger gradients on the eastern side of the ridge, corresponding to the warm front of the cyclonic system, (figure 3.13). M-LC2-R60 shows the same evolution as D-LC2 up to day 4, similar to M-LC2-R60. The 850hPa potential temperature field of M-LC2-R80 is distorted compared to the smooth contours of M-LC2-R60. M-LC2-R80 has an initial RH of 80%, which is a 20% increase from M-LC2-R60, indicating that moisture already has an effect on the lifecycle of the system by day 4.

Day 6:
On day 6, the surface cyclones in MLC2 continue to intensify (figure 3.12). In comparison, the horizontal radius of the surface cyclones is larger in M-LC2-R60 than in M-LC2-R80. The surface cyclones in M-LC2-R80 are circular with a small southeastern tail. The ridge of the TCWV contours of M-LC2-R80 is flatter compared to M-LC2-R60 and D-LC2 (figure 3.13b). This is related to the more zonal 850hPa potential temperature field of the warm front. Additionally, the 2PVU potential temperature field of M-LC2-R60 and M-LC2-R80 displays cyclonic motion of the relativly warm ridges and cold troughs (figure 3.12), which is similar to D-LC2 (figure 3.1b).

Day 8:
Between day 6 and 7, both M-LC2-R60 and M-LC2-R80 show the merging of the cold front and warm front, resulting in an occluded front, leading to the detachment of the surface cyclones from their heat source in the south on day 8 (figure 3.13). In contrast, these features do not emerge until day 12 for D-LC2. The frontal regions of M-LC2-R60 are still linked to the northern portion of the ridge, similar to D-LC2, whereas for M-LC2-R80, the frontal regions are connected more to the east side of the ridge of the relatively warm air. Both M-LC2-R60 and M-LC2-R80 display a circular pattern with surface isobars similar to D-LC2 (figure 3.12). On day 8, the placement of the upper-level wind at 200hPa for M-LC2-R60 and M-LC2-R80 (figure 3.14) is similar to D-LC2, day 10. (figure 3.3b).

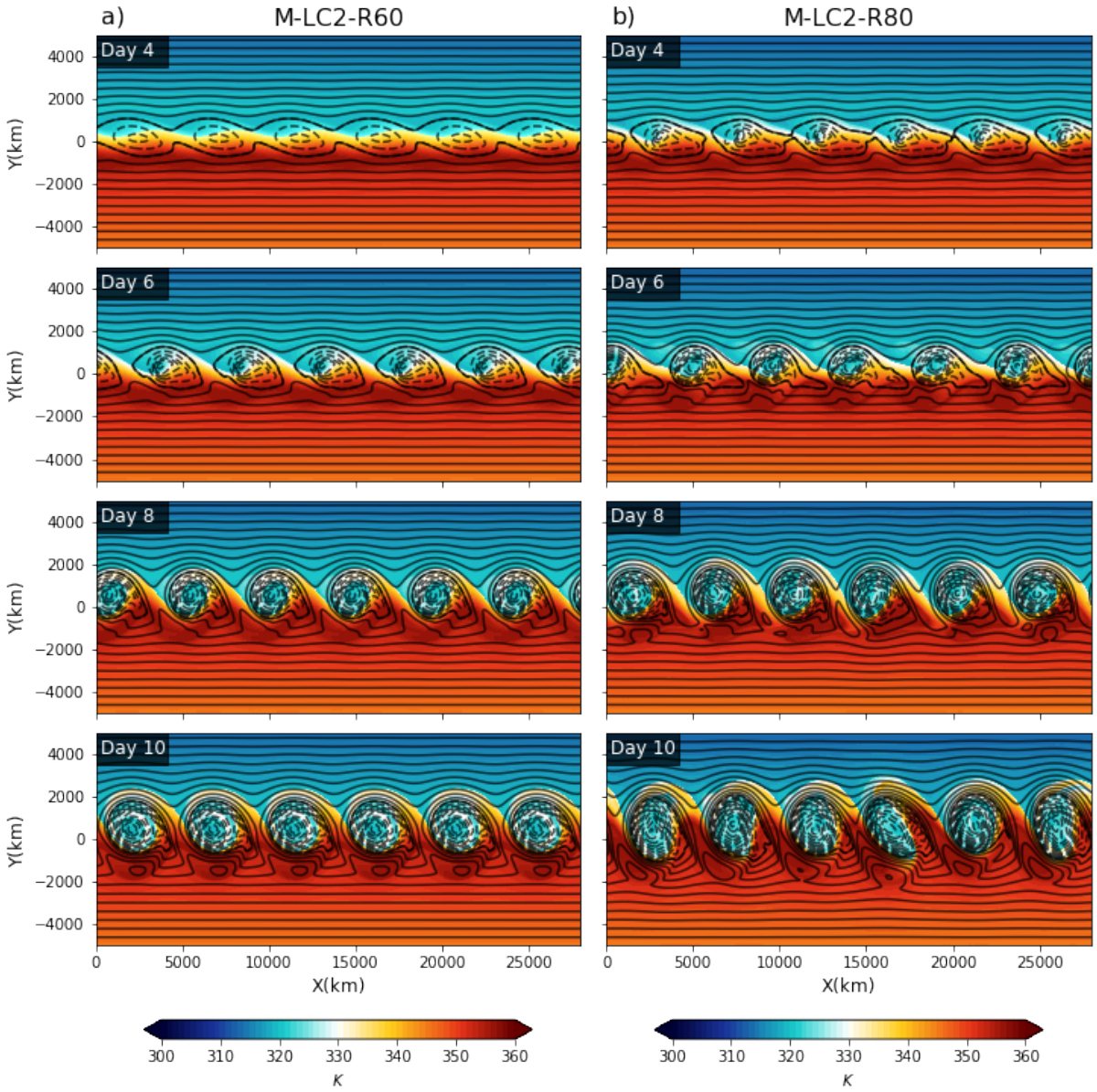

Figure 3.12: Surface pressure (black contours in hPa) and potential temperature on the PV = 2 PVU surface (shading in K) for a) M-LC2-R60 and b) M-LC2-R80. The contour lines are drawn at intervals of 5hPa, with the bold contour line representing the 1000hPa level. Dashed contours indicate pressure below 1000hPa and solid lines indicate pressure above 1000hPa.

Day 10:

On day 10, both M-LC2-R60 and M-LC2-R80 show a continued expansion and a slight northward movement of the surface cyclones (figure 3.12). The 2PVU potential temperature field wraps cyclonically around the surface cyclones. Even though the cyclone has disconnected from the relatively warm source of air from the south, M-LC2-R60, the 850 potential temperature field shows that these warm air masses still stretch northward, turning westward around the cyclones (figure 3.13a). The moist air follows the potential temperature contours and wraps more around the isolated cyclone. However, in M-LC2-R80, the relatively moist, warm air does not move as far northward compared to M-LC1-R60 and does not wrap cyclonically around the cyclone as observed in M-LC1-R60 (figure 3.13). On day 10, we observe the emergence of asymmetries in the potential

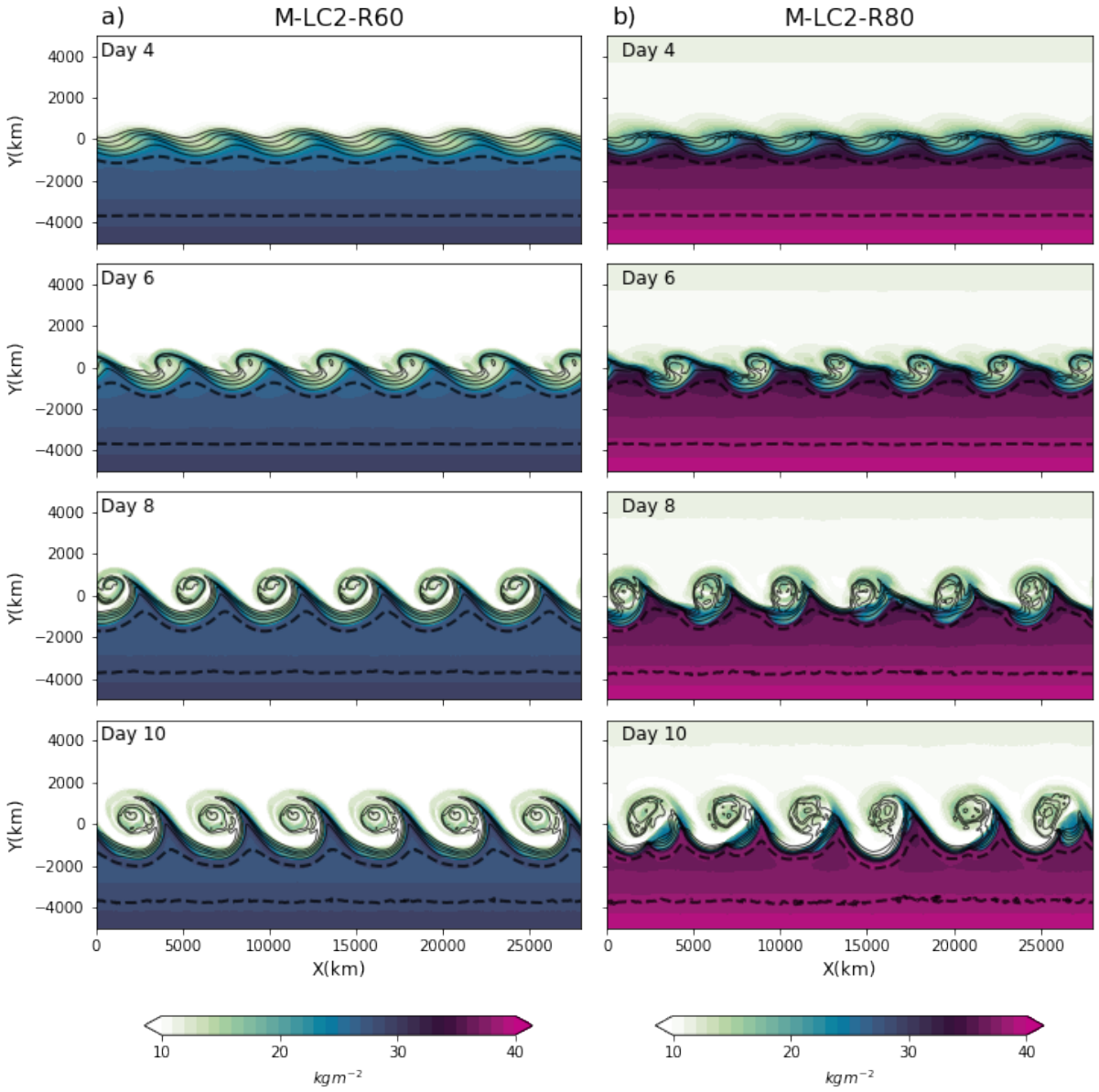

Figure 3.13: Potential temperature (contours in K) at 850hPa and TCWV (shading in kgm^{-2}) for a)M-LC2-R60 and b)M-LC2-R80. The contour lines are drawn at intervals of 5K, with the stippled contour line representing the 300K contour.

temperature and TCWV, although not to the same extent as in M-LC1-R80, indicating that the wavenumber for LC2 ($k = 5$) is a more appropriate choice for the moist LC2 case compared to moist LC1 experiments. The southward flow of the M-LC2-R60 upper-level wind is notably stronger and broader compared to its nortward flow, unlike D-LC2, where both northward and southward flow are fairly similar (figure 3.14a). Meanwhile, the M-LC2-R80 upper-level wind is similar in strength and width for both northward and southward flow, but produces more of a curved shape than D-LC2, with the edge of the curve reaching less far north (figure 3.14c).

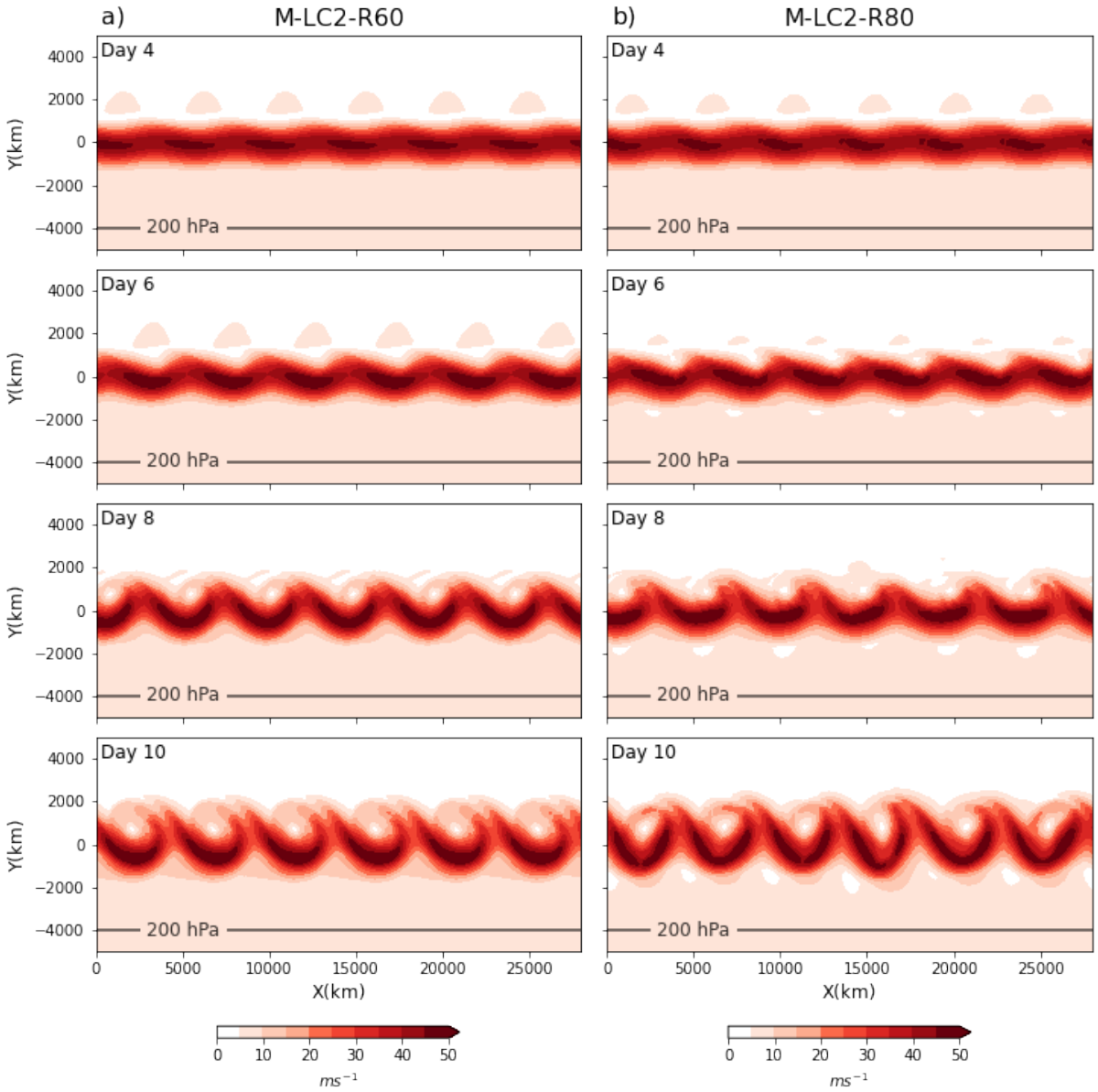

Figure 3.14: Total wind speed at 200hPa (shading in ms^{-1}) for a) M-LC2-R60 and b) M-LC2-R80

EP-flux

Until day 8, the EP-fluxes of M-LC2-R60 show similar characteristics to D-LC2 (figure 3.15a). On day 6, the heat fluxes in the lower troposphere and the momentum fluxes in the upper troposphere affect the EP-fluxes of M-LC2-R60. On day 8, the EP-fluxes for M-LC2-R60 in the lower troposphere is directed more southward compared to day 6, unlike D-LC2, where we mainly observe an increase in northward-directed arrows. On day 10, the arrows turn horizontal, directed northward, indicating southward momentum flux, similar to D-LC2.

Overall, the EP-flux divergence of M-LC2-R60 shows a similar pattern to D-LC2 with a slightly higher density of the contours, especially from day 6 (figure 3.15a). The shift of the jet is hardly different from D-LC1, but the jet core strength is weaker in M-LC2-R60

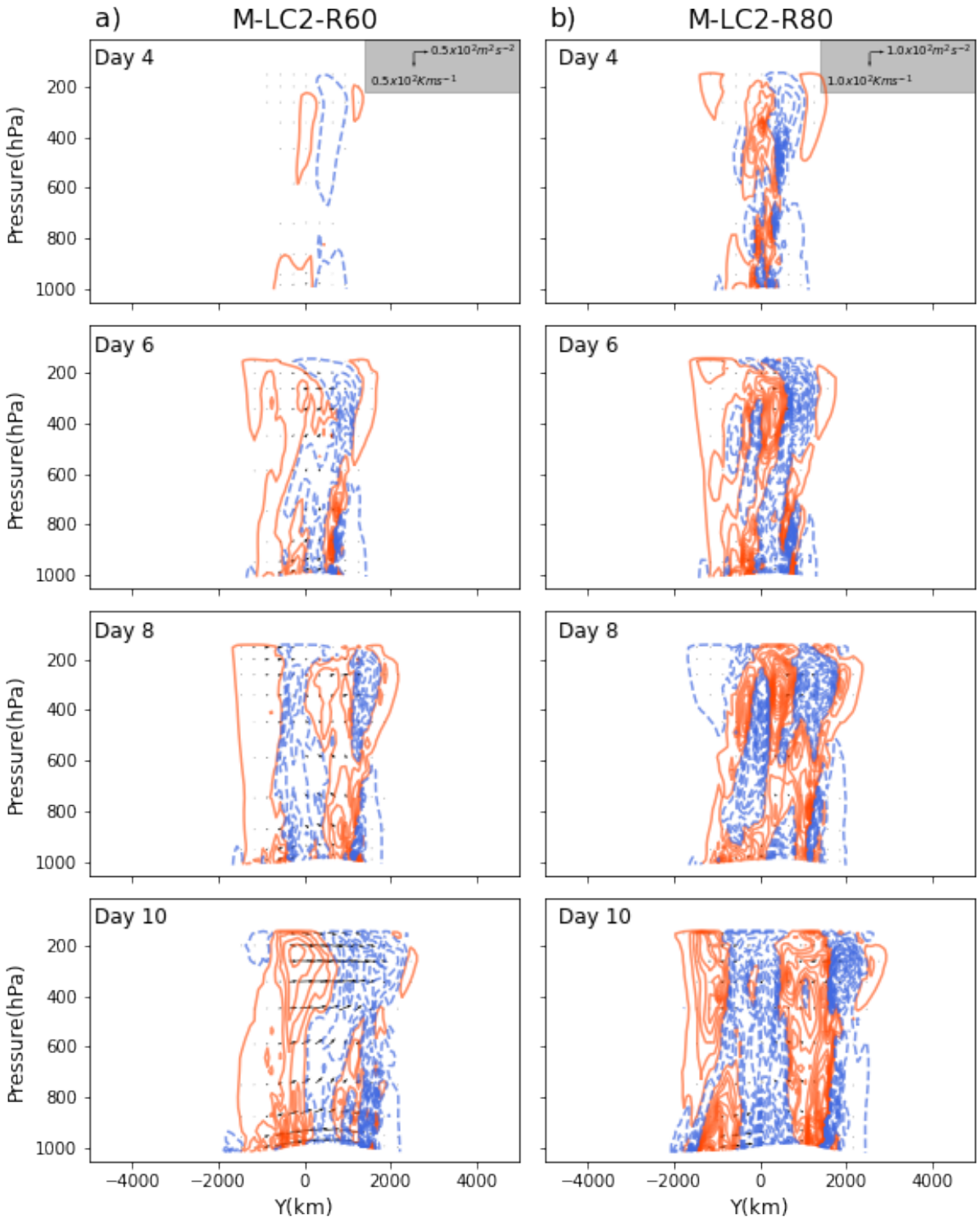

Figure 3.15: EP-flux (arrows, where the vectors are in m^2s^{-2} and Kms^{-2}) and its divergence (contours in ms^{-2}) for a) M-LC2-R60 and b) M-LC2-R80. The divergence is multiplied by 400. Solid red contours denote the flux divergence giving eastward flow acceleration. Dashed blue contours denote the flux convergence giving eastward flow deceleration. Contour interval is $10ms^{-2}$.

on day 8 and 10 compared to D-LC2, (figure 3.16a), which corresponds well with the increased divergence and convergence of the EP-fluxes.

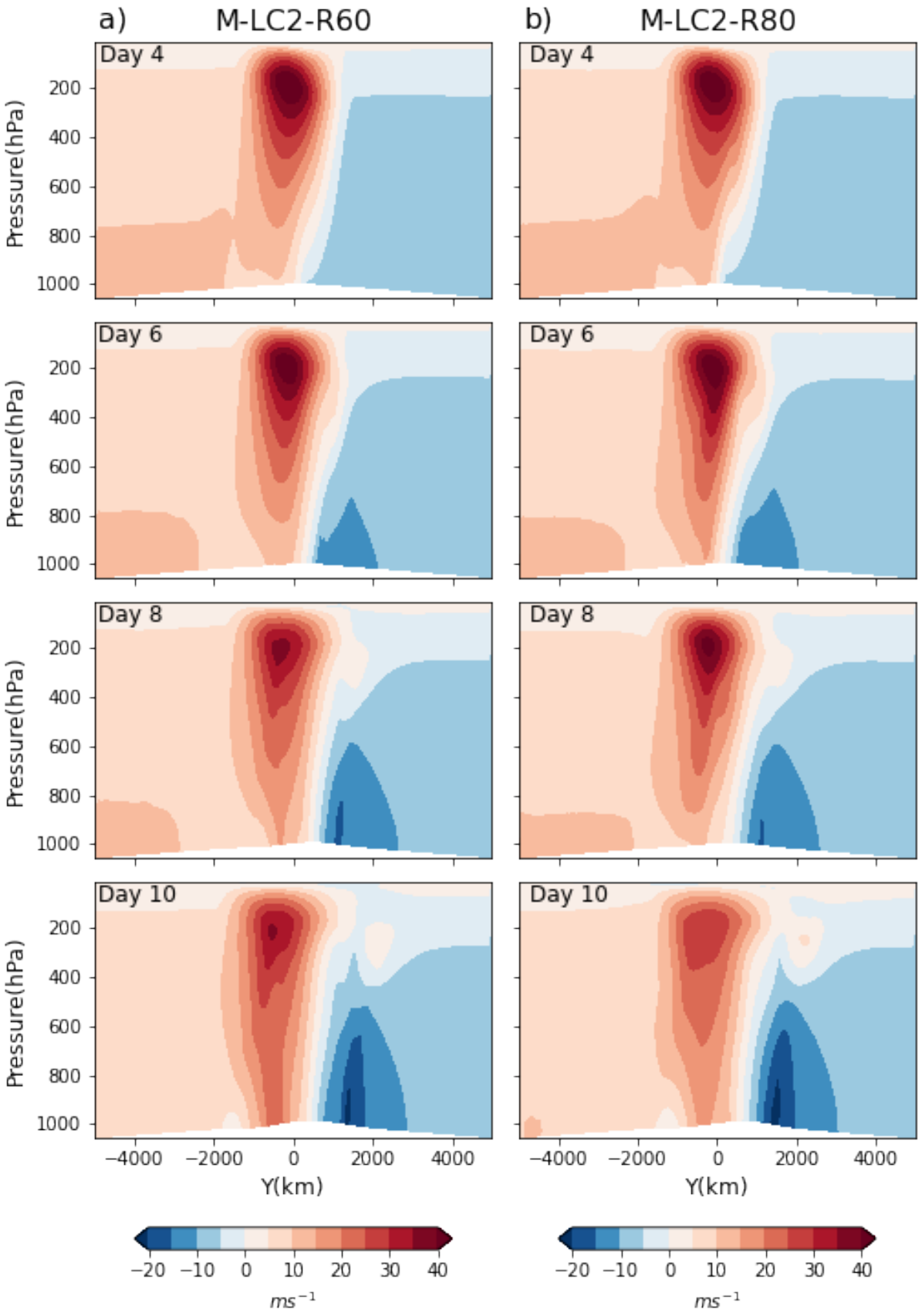

Figure 3.16: Zonal mean zonal wind (shading in ms^{-2}) for a) M-LC2-R60 and b) M-LC2-R80

The EP-flux vectors for M-LC2-R80 are relatively small compared to D-LC2 and M-LC2-R60 (figure 3.15b). The arrows in M-LC2-R80 are primarily influenced by heat fluxes in the mid-troposphere and momentum fluxes in the upper troposphere, with the momentum fluxes directed southward, as observed in M-LC2-R60 and D-LC2.

Throughout its lifecycle, the contour density of the EP-fluxes in M-LC2-R80 is higher than that in D-LC2 and M-LC2-R60 (figure 3.10b). Similar to D-LC2 and M-LC2-R60, the divergence and convergence of M-LC2-R80 correspond to a slight southward shift of the jet, particularly in the lower levels (figure 3.16b). Additionally, the wind speed at the jet core decreases significantly. This phenomenon is also observed in M-LC1-R80, however, the general jet structure decelerates more compared to M-LC1-R60.

Energetics

The EKE curve for M-LC2-R60 follows the curve of D-LC2 (figure 3.6). Generally, baroclinic growth is more intense in M-LC2-R60 than in D-LC2, reaching peak levels one day earlier. The barotropic decay is slightly more defined, with a slight decrease in EKE levels from day 10 to day 13.

The EKE curve of M-LC2-R80 is quite different from that of D-LC2 and M-LC2-R60 (figure 3.6). Until day 9, the M-LC2-R80 EKE levels follow the M-LC2-R60 EKE levels. However, at this point, the M-LC2-R60 EKE curve levels off, but the M-LC2-R80 EKE levels continue to grow until day 12. Afterward, M-LC2-R80 experiences a rapid transition into a barotropic decay, which is more pronounced than that observed in D-LC2 and M-LC2-R60. The maximum EKE levels in M-LC2-R80 are approximately $10 \cdot 10^5 Jm^{-2}$, which is twice the maximum EKE observed in both D-LC2 and M-LC2-R60. Observations of the EKE show that the inclusion of moisture, with high RH induces stronger cyclone growth.

3.3 Synoptic evolution of LD-LC1 and LD-LC2

In the first 6 experiments, we initialized with a modal perturbation for comparison with THM93. It also has the advantage of the synoptic systems developing at the same rate (symmetric). But it is of interest to study how the lifecycle develops if initialized with a localized pressure perturbation (figure 2.2c).

In the experiments initialized with localized pressure perturbation, the systems do not develop at the same time as we see in the model perturbation experiments. Therefore, we have numbered the developing systems in each experiment to easier keep track of which system we are discussing (e.g. figure 3.17). For LC1 experiments the systems are labeled with "S#" where the anticyclone and corresponding cyclones are considered as one system. For LC2 experiments, there are only surface cyclones developing and therefore they are named with "C#".

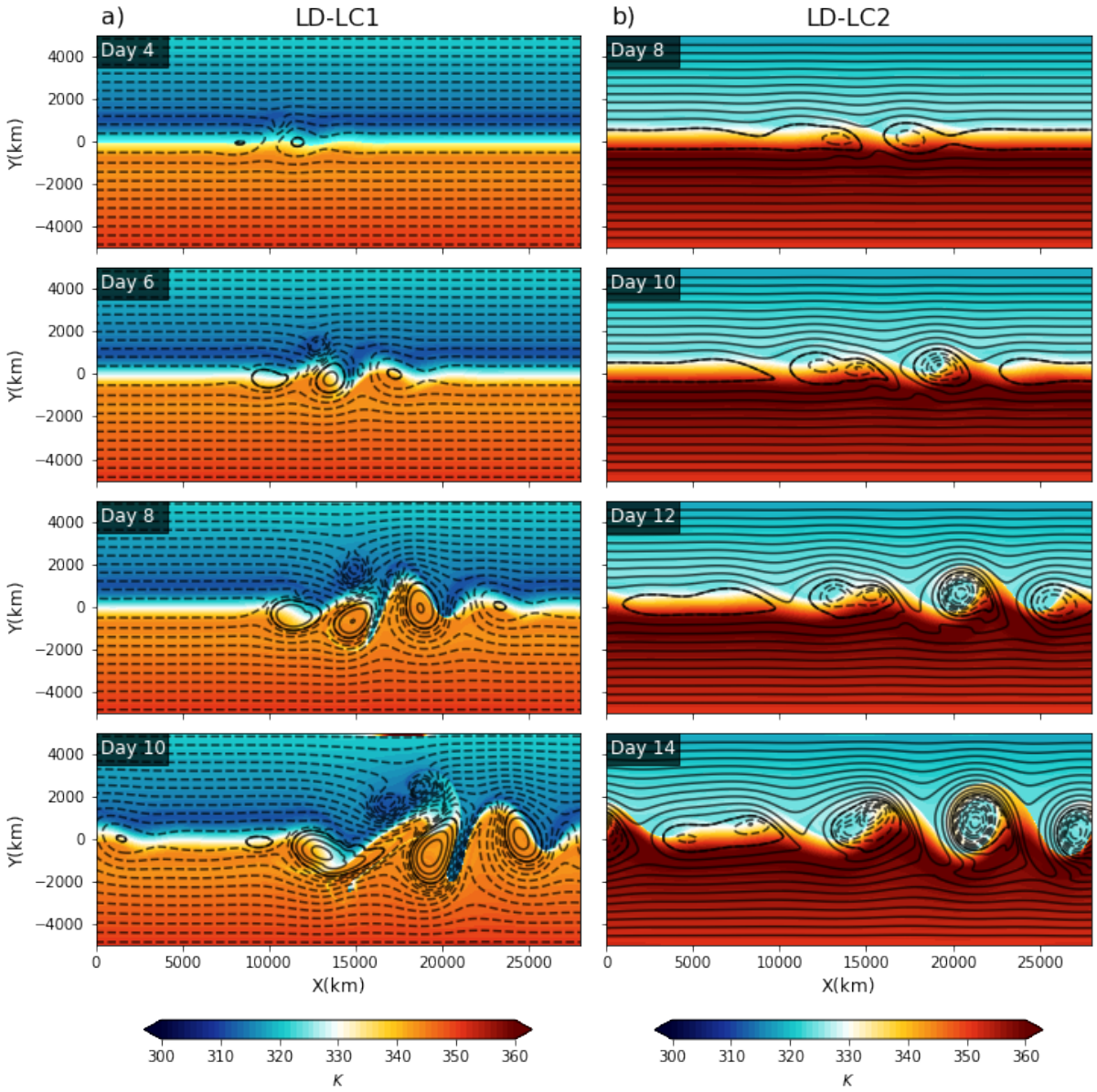

Figure 3.17: Surface pressure (black contours in hPa) and potential temperature on the PV = 2 PVU surface (shading in K) for a) LD-LC1 and b) LD-LC2. The contour lines are drawn at intervals of 5hPa, with the bold contour line representing the 1000hPa level. Dashed contours indicate pressure below 1000hPa and solid lines indicate pressure above 1000hPa.

3.3.1 LD-LC1

Day 4

On day 4, we have the development of two surface anticyclones at $y = 0$, with a cyclone developing to the northwest of the primary anticyclone (S1), (figure 3.17a). The growth of the cyclones is also apparent in the 850hPa potential temperature field, where we have stronger gradients along the cold front (figure 3.18a). We observe, in LD-LC1, primarily development of anticyclones on day 4 which is consistent with the evolution in D-LC1. However, the surface cyclone of S1 seems to be developing at a quicker rate(figure 3.17a), compared to D-LC1 (figure 3.1a).

Day 6

On day 6, S1 and S2 have developed further and we see new development of a surface anticyclone in front of the pre-existing systems (figure 3.17a). The potential temperature on the 2PVU field shows the development of a NE-SW tilting ridge of relatively warm air connected to S1 (figure 3.18a). The developing ridge connected to S3 has no particular tilt on day 6. The 850hPa potential temperature field shows the cold front of the primary cyclone has almost caught up with the warm front (figure 3.18a). The upper-level wind is still almost entirely zonal, with a small northward curve forming over the location of surface highs and lows (figure 3.19a). Compared to D-LC1, on day 6, D-LC1 has a clear northward curved shape of the upper-level wind, while the LD-LC1 upper-level wind is barely changed from its zonal position. The surface systems are connected to the position of the upper-level wind, where a relatively zonal wind tends to favor cyclone development over anticyclone development.

Day 8

On day 8, the anticyclone of S3 has intensified and grown to be larger than the succeeding systems, with cyclogenesis located to the northwest (figure 3.17a). There is also the development of a new surface system (anticyclone and cyclone) ahead of S3. The 2PVU potential temperature field shows a narrowing ridge of the developing potential temperature contours connected to S1 and S3(figure 3.17a). The cyclone (S1) has disconnected from its warm source in the south, but there is still a ridge connected to the southern part of the cyclone(figure 3.18a). The potential temperature contours connected to S3 shows stronger gradients on the western side of the ridge, which is the cold front of the developing surface cyclone (S3). The upper-level wind can explain some of the patterns we see at the surface (figure 3.19a). The part of the upper-level wind located over S1 ($x = 15000km$) is still almost zonal. S1 has stronger development of the surface cyclone compared to the other systems. The upper-level wind located over S3 is curving northward and S3 has a strong development of the surface anticyclone compared to the other systems. Even though anticyclonic growth is still favored in LD-LC1, it is not to the same extent as in D-LC1, and the surface cyclones have a bit grown more compared to D-LC1 at this point in time.

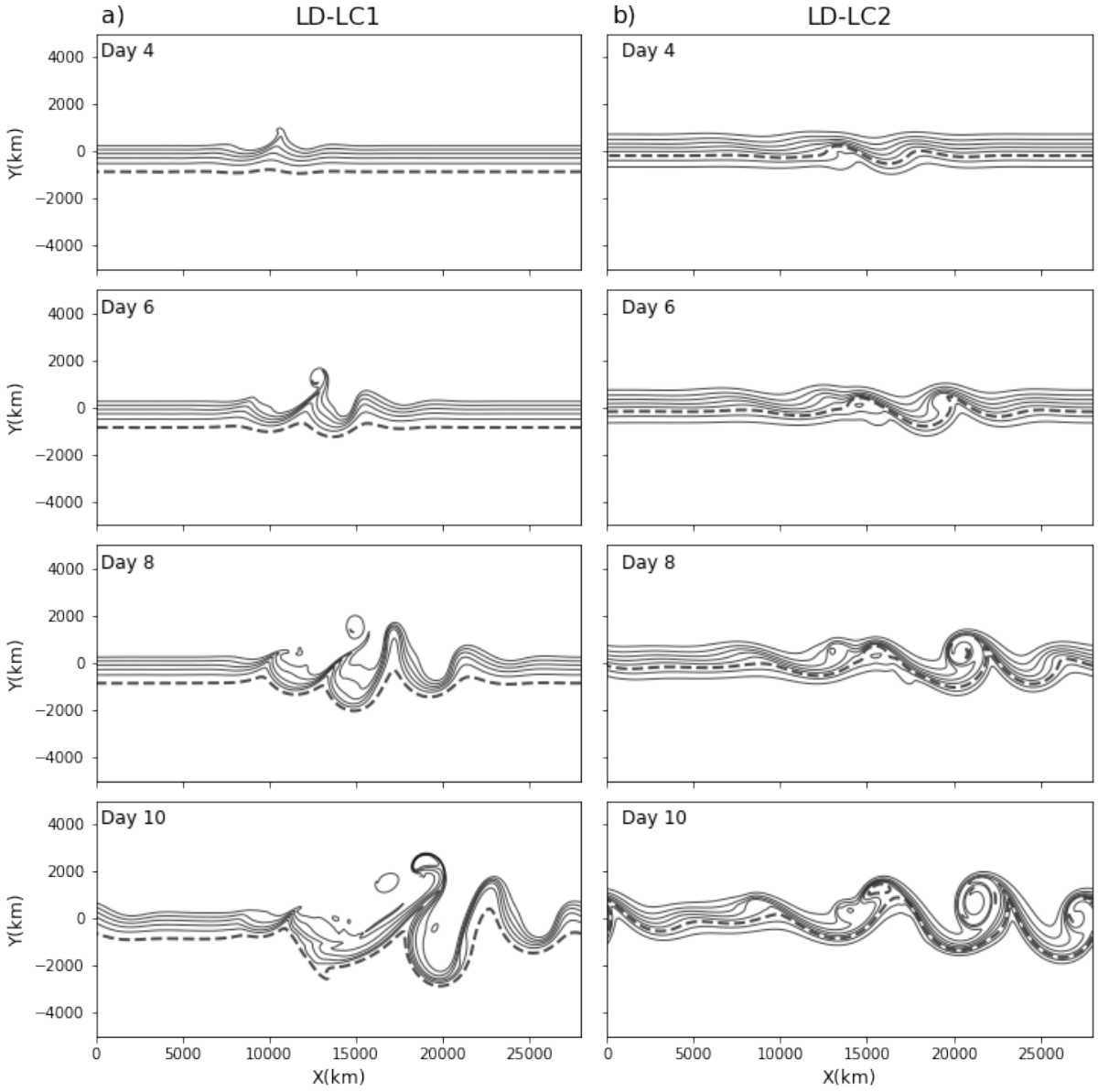

Figure 3.18: Potential temperature (contours in K) for a)LD-LC1 and b)LD-LC2. The contour lines are drawn at intervals of 5K, with the stippled contour line representing the 300K contour.

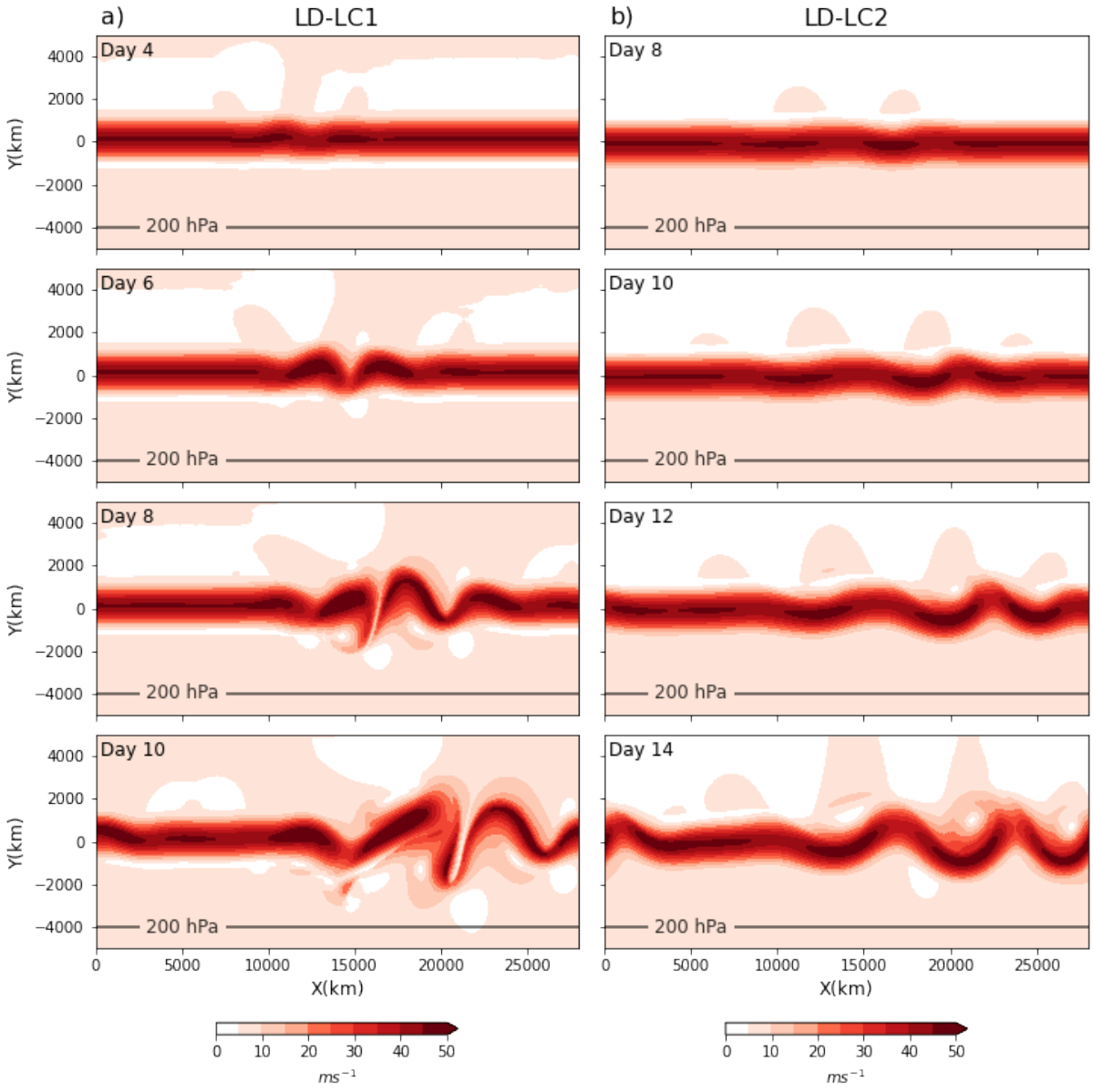

Figure 3.19: Total wind speed at 200hPa (shading in ms^{-1}) for a) LD-LC1 and b) LD-LC2

Day 10
On day 10, the cyclone connected to S3 has grown explosively moving several 100 km northward. The corresponding anticyclone is relatively stationary compared to the succeeding systems, blocking their westward movement (figure 3.17a). Therefore the anticyclone of S2 is merging with the anticyclone of S1 (figure 3.17a). On the 2PVU potential temperature field, the ridge over S1 is merged with the ridge of S3, tilting it NE-SW. The corresponding trough for S3 is narrowing and stretching meridionally. Ahead of S3, S4 shows the same characteristics as S3 on day 8. At the upper-level wind, we have a slight northward shift.

Over the next few days (not shown in the figures), we have the development of new anticyclones ahead of previously developed systems blocking the westward movement. Between day 12 and 14 the cyclone of S3 hits the northern boundary and the atmosphere becomes chaotic.

EP-flux

Prior to day 8, there are almost no EP-fluxes visible in figure 3.20a. However, it is not until day 10, we are able to observe the direction of the arrows. On day 10 we observe vertical arrows in the lower- to mid-troposphere indicating the majority of the EP-fluxes is stemming from the heat fluxes. In the northern, upper troposphere we observe southward-directed horizontal arrows indicating northward momentum fluxes.

The contours of the EP-fluxes indicate only a slight deceleration and acceleration of the zonal mean wind (figure 3.21a). The zonal mean wind shows a slight deceleration at the jet core between day 4 and 10. There is also a slight tilt to the north of the surface wind. Even though it is not as clear a northward shift of the jet structure after 10 days as seen in D-LC1 (figure 3.5a), there is an indication of the northward shift. Additionally, we observe the same weakening of the jet structure as observed in D-LC1.

The EP-flux is calculated as a zonal mean and since each system develops at different timesteps, this will influence the results. In the modally perturbed experiment (D-LC1, figure 3.1a) the five cyclones grow simultaneously, while in LD-LC1, which is locally perturbed, we observe upstream and downstream development of new cyclones throughout the entire simulation (figure 3.17a). The small contribution to the EP-fluxes in LD-LC1 prior to day 8 is likely due to the fact that there are only two-three cyclones developing in a small subregion with no activity outside this region.

Energetics

From day 6 onwards, the EKE of LD-LC1 increases and continues to increase throughout the remaining simulation period (figure 3.22). Prior to day 6, we only observe the development and growth of two cyclones, whereas after day 6 we see the appearance of several new cyclones. Additionally, the primary and secondary cyclones have been, on day 6, developing for some time. Because of the constant appearance of new cyclones, we do not get the clear baroclinic growth and barotropic decay phases as observed in D-LC1 (figure 3.6). Potentially, if the duration of the simulation is extended or if we

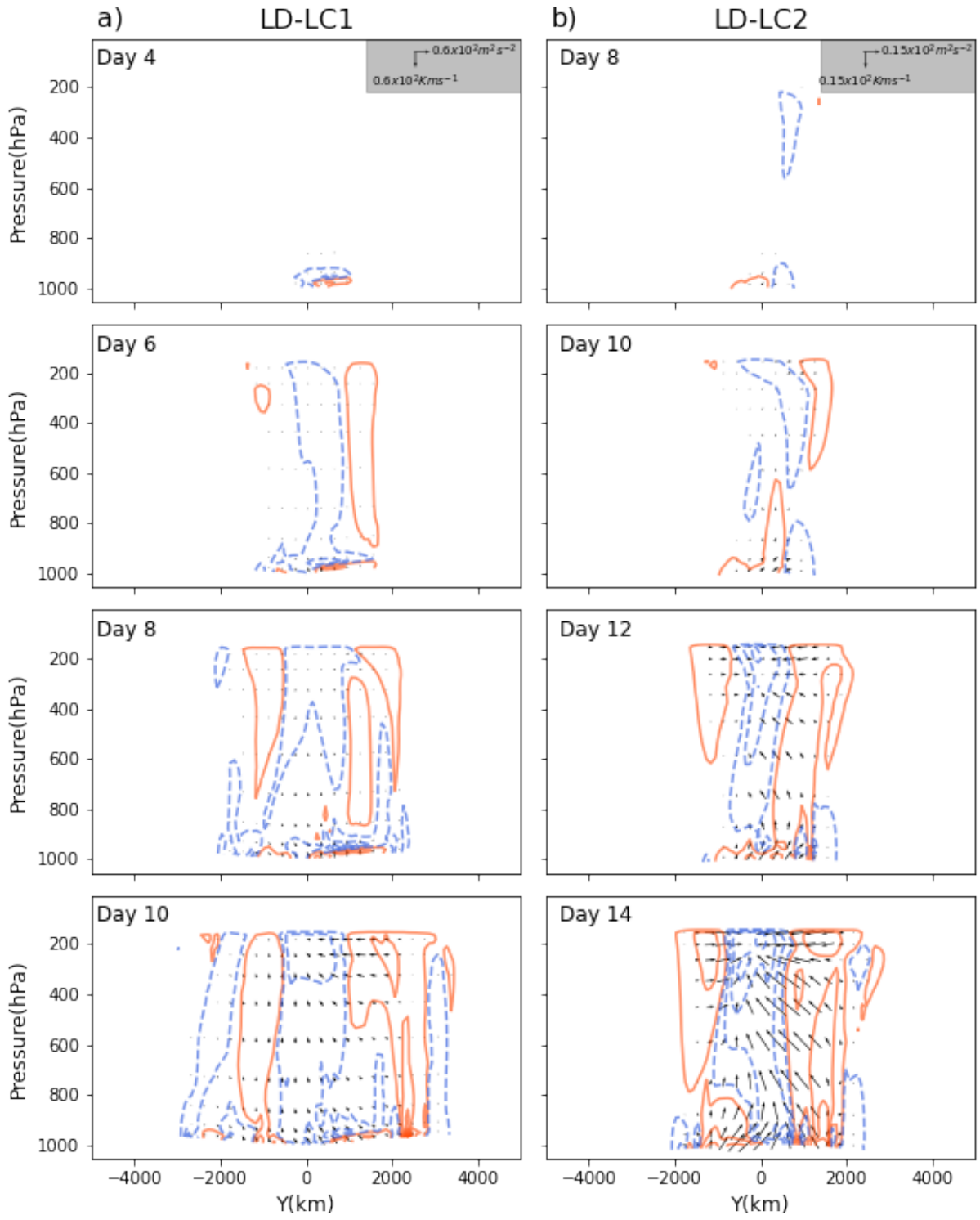

Figure 3.20: EP-flux (arrows, where the vectors are in m^2s^{-2} (momentum flux) and Kms^{-2} (heat flux)) and its divergence (contours in ms^{-2}) for a) LD-LC1 and b) LD-LC2. The divergence is multiplied by 400. Solid red contours denote the flux divergence giving eastward flow acceleration. Dashed blue contours denote the flux convergence giving eastward flow deceleration. Contour interval is $10ms^{-2}$.

limited the area to only cover one cyclone (e.g S1) when calculating the EKE we could potentially be able to observe the barotropic decay phase.

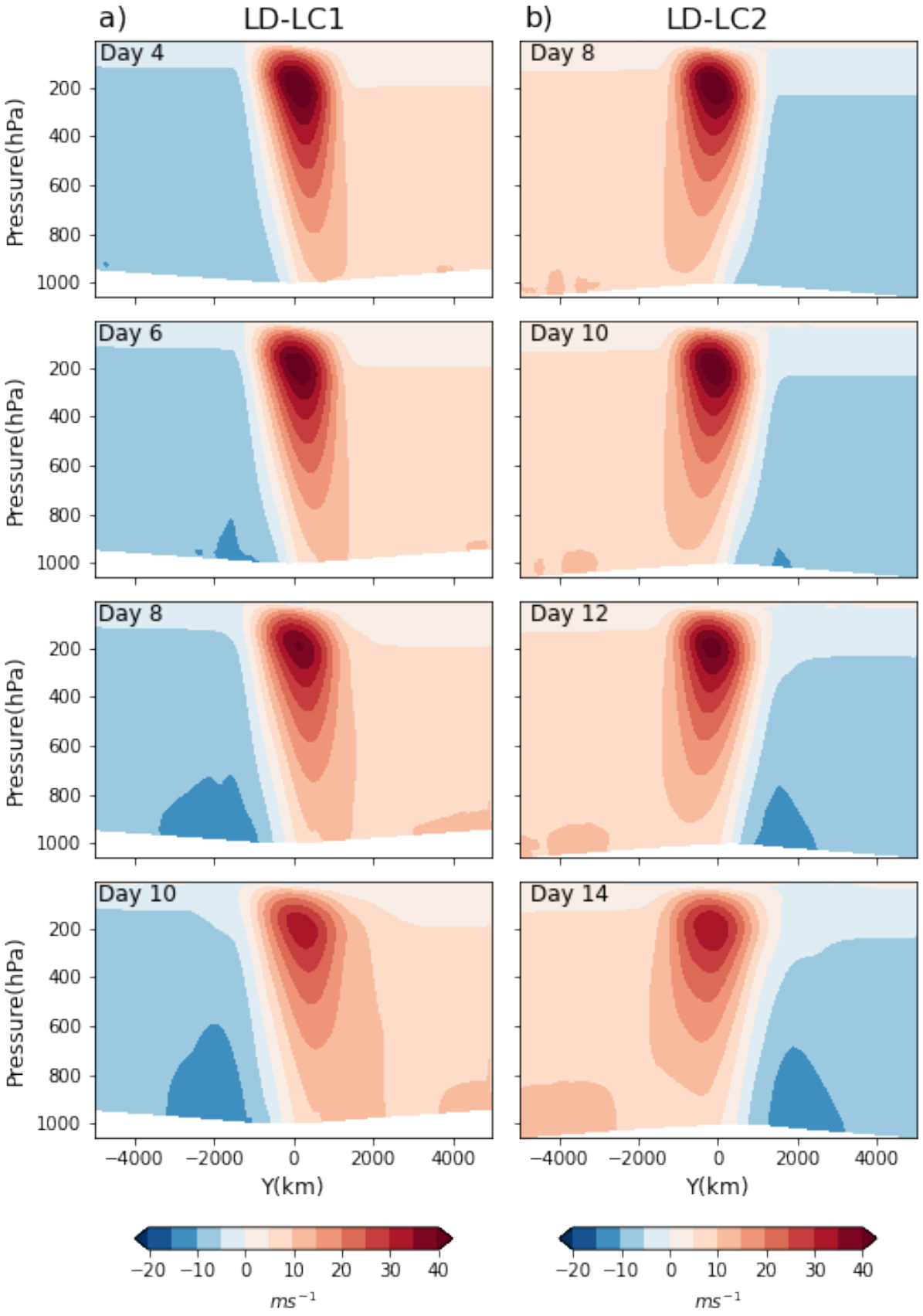

Figure 3.21: Zonal mean zonal wind (shading in ms^{-2}) for a) LD-LC1 and b) LD-LC2.

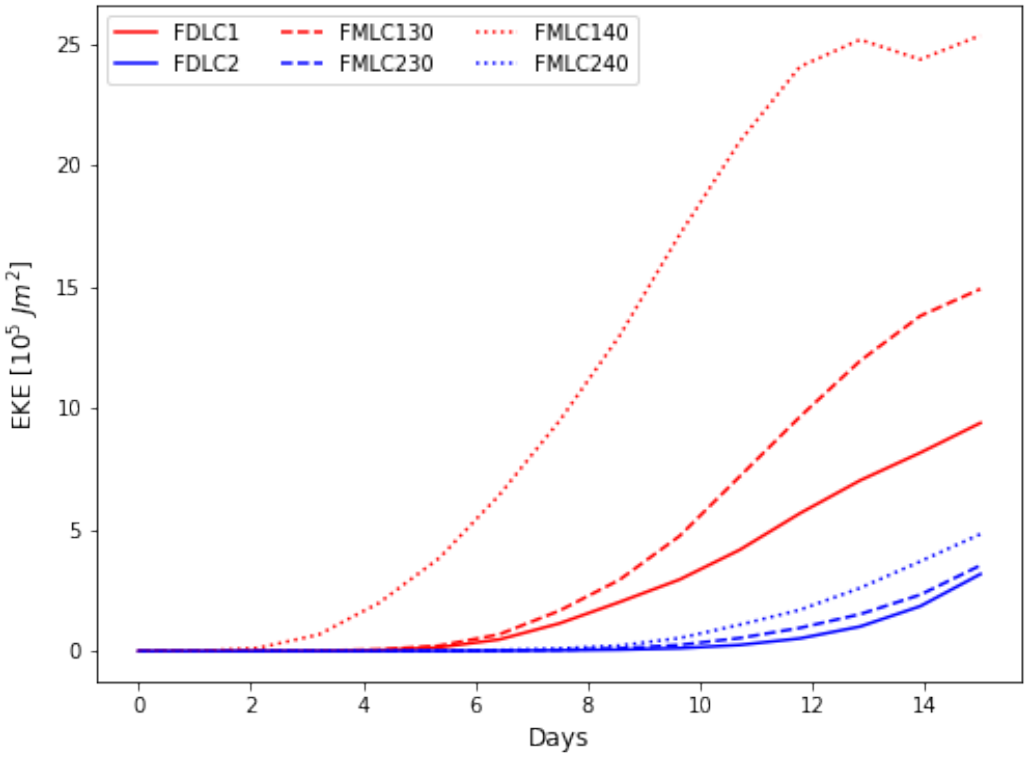

Figure 3.22: Eddy kinetic energy ($10^5 Jm^{-2}$) for localized pressure perturbed experiments.

3.3.2 LD-LC2

Day 8

On day 8, two surface cyclones are growing at $y = 0$ (figure 3.17b), with C1 having a circular shape and C2 being zonally stretched with two centers. The 850hPa potential temperature field indicates that the developing wave has stronger gradients on the east side of the ridge, corresponding to the warm front of C2 (figure 3.18b). C1's frontal structures is less prominent on day 8, but the shape resembled the shape of surface cyclones in D-LC2. Both cyclones' frontal structures had similar characteristics to D-LC2 due to the NW-SE tilted 850hPa potential temperature field.

Day 10

By day 10, warm air moving northward in the upper troposphere is creating a ridge over C1, with C1 growing most rapidly at the surface(figure 3.1b). C2 is dividing into two cyclones, with the larger one to the west. There is also evidence of a new cyclone developing upstream of C1. The 850hPa potential temperature field now reveals a clear frontal structure of C1, while C2 is split, with the most eastern cyclone core having a more defined frontal structure. The upper-level wind shows a slight curve southward over the area of cyclone development (figure 3.19b). On day 10, C1 shares similarities with D-LC2 in terms of the shape of the isobars and the shape of the 850hPa potential temperature field, while C2 has similar frontal structure characteristics, albeit with some differences in the shape due to the split.

Day 12

On day 12, it is evident from the results displayed in figure 3.17b that C3, developing upstream from C1, is growing at a faster rate compared to C2. Additionally, a new cyclone is developing downstream from C2. The 2PVU potential temperature field reveals a wave where the ridges are tilting NW-SE, with the ridge over C1 wrapping up cyclonically (figure 3.1b). Furthermore, the cold front of C1 is observed to be moving at a faster speed compared to the warm front, resulting in occlusion and seclusion of warm air within the cyclone core on day 12 (figure 3.18b).

Day 14

On day 14, the surface pressure field indicates that the split cyclones within C2 have merged, while a new cyclone, C4, has developed downstream of C2, exhibiting two pressure minima similar to C2 (figure 3.17b). C4 shares similarities with C1 in terms of its surface features, as well as with the 2PVU potential temperature field wrapping up cyclonically (figure 3.17b). The upper-level wind curves southward over C1 and C3, while remaining more zonal over C2 and C4. This corresponds well with the circular shape of C1 and C4, which are wider, compared to C2 and C3, which are more zonally elongated. In comparison to D-LC2, the cyclones developing upstream exhibit the same characteristics of surface pressure, the potential temperature fields of the lower and upper troposphere, and the upper-level wind structure. The characteristics of C2 and C4 still exhibit cyclonic motion of the potential temperature field with stronger gradients along the warm front but differ with the split of the cyclone core and the zonally elongated shape of these cyclones.

EP-flux

On day 8 in LD-LC2, we observe EP-fluxes only in the lower troposphere, but the strength of the fluxes is minor (figure 3.20b). Over the next few days, the EP-fluxes strengthen and we observe EP-fluxes throughout the entire troposphere around $y = 0$. On day 12, the direction of the arrows is vertical in the lower- to mid-troposphere, while horizontal in the upper troposphere. The horizontal arrows in the upper troposphere are directed southward in the northern domain and northward in the southern domain. The strength of the individual arrows causes convergence at $y = 0$ and divergence further north and south. Over the next few days, the fluxes continue to strengthen, while the overall direction remains mostly unchanged.

Between day 8 and 10, the zonal mean wind hardly changes from its original state (figure 3.21b). However, over the next few days, we observe a deceleration of the jet core resulting from the convergence of EP-fluxes in this area (figure 3.20b). Between day 12 and 14, there is further deceleration of the jet core. Additionally, the jet does not extend as far toward the surface as it originally did. We also observe the strengthening of the easterlies in the lower- to mid-troposphere at around $y = 2000$km.

LD-LC1 sees the appearance of EP-fluxes at a much later time compared to D-LC1 (figure 3.4b). This is a consequence of cyclone growth being much slower compared to D-LC1. Contrarily, the weakening of the jet core and no particular south- or northward

displacement of the jet is consistent with the characteristics described for D-LC1.

Energetics

From day 11 onwards, the EKE of LD-LC2 increases and continues to increase through the remaining simulation period (figure 3.22). Like D-LC1, prior to day 10, we only observe the development of two cyclones, whereas after day 12 we see the appearance of new cyclones both upstream and downstream (figure 3.17b). For the modal perturbed experiments, we observed that D-LC2 has smaller values of EKE compared to D-LC1. This is also observed in the localized perturbed experiments. The EKE for LD-LC2 increases at a later time and at a slower rate compared to LD-LC1. Additionally, as observed for LD-LC1, there is no decay phase observed in LD-LC2. With a longer simulation period or limited zonal area to only cover one cyclone (e.g C1) instead of the entire zonal domain, one could potentially observe a different evolution of the EKE curve.

3.4 Synoptic evolution of LM-LC1 and LM-LC2

3.4.1 LM-LC1

Day 4

On day 4 of the experiment, LM-LC1-R60 exhibits the formation of two surface anticyclones at $y = 0$, with a cyclone developing to the northwest of the anticyclone (C1) (figure 3.23a). The development of the cyclones is also evident in the 850hPa potential temperature field, with stronger gradients along the cold front (figure 3.24a). At this stage, there is no noticeable difference in the development of the systems compared to LD-LC1. The resemblance between LM-LC1-R60 and LD-LC1, in terms of the impact of moisture on the lifecycle, is already observed in M-LC1-R60 and D-LC1. This is most likely due to the fact that the atmosphere is not yet sufficiently saturated for moisture to have a significant effect on the lifecycle.

In the LM-LC1-R80 experiments, the initial RH is increased by 20% compared to LM-LC1-R60. As a result, it was observed that the two cyclones present intensified significantly on day 4 (figure 3.7b). Furthermore, the anticyclonic strength is reduced compared to LD-LC1 and LM-LC1-R60. The 850hPa potential temperature field shows that the cold front of the cyclone connected to S1 has caught up with the warm front and occluded (figure 3.8b). The warm moist air has not moved far north during this process due to the rapid cyclogenesis of the cyclone connected to S1. The 2PVU potential temperature field shows that relatively warm air is wrapping cyclonically above the location of surface cyclones (figure 3.17b). In previous experiments (e.g. M-LC1-R80) the trough of the potential temperature contours is narrow and meridionally stretched even though we see the cyclonic motion of the warm side. In LM-LC1-R60, the trough is narrowing but limited in the y-direction.

Day 6

On day 6, in the LM-LC1-R60 experiment, we observe the progression of S1 and S2, along with the emergence of a new surface anticyclone and cyclone ahead of the pre-existing

systems (figure 3.17a). The potential temperature on the 2PVU surface displays the development of a NE-SW tilted ridge of relatively warm air associated with S1 (figure 3.18a). The developing ridge linked to S3 is exhibiting indications of turning in a cyclonic direction. Furthermore, the 850hPa potential temperature field shows that the cold front of S1 and S3 has caught up with the warm front and occluded (figure 3.18a). The upper-level wind remains almost zonal, but a small, steep northward curve is forming over the position of S1 (figure 3.19a). In contrast to LD-LC1, we can now begin to notice the effects of moisture as evidenced by the presence of the cyclone attached to S3 on day 6. This is also evident in the cyclonic motion of the ridge of the 850hPa potential temperature field, which was also a characteristic seen when moisture was added to the model-perturbed experiments of LC1.

Over the next few days of the LM-LC1-R80 experiment, there is an intensification of the cyclone connected to S1, (figure 3.23b). Compared to LM-LC1-R60, the cyclones' intensification is significantly greater due to increased energy from latent heat release. This is also evident at the 850hPa potential temperature field, where the cyclone already is disconnected from its warm source in the south by day 6 (figure 3.24b). New systems emerged behind and ahead of the prevailing systems, while the existing anticyclone of S1 moved westward at a slower pace than the succeeding systems, hindering their westward movement. Additionally, the surface cyclone corresponding to the blocking anticyclone is prevented from expanding and moving northward. The blocking anticyclones impeded the development of troughs in the upper potential temperature field in the manner characteristic of LC1 development, and the two ridges of the wave merged at an early time step (figure 3.17b).

Day 8

On day 8, in the LM-LC1-R60 experiment, the anticyclone of S2 merges with the blocking anticyclone of S3, while a new surface system (anticyclone and cyclone) develops ahead of S3 (figure 3.23a). Both cyclones connected to S1 and S3 intensify, with cyclone (S3) showing the most rapid intensification. The 2PVU potential temperature field shows a narrowing trough wrapping anticyclonically around the surface anticyclone (S3) (figure 3.23a), and the ridge wrapping up cyclonically around the surface cyclone (S3). The 850hPa potential temperature field connected to S4 exhibits stronger gradients on the western side of the ridge, which corresponds to the cold front of the developing surface cyclone (figure 3.24a). Notably, as the microphysics contribution becomes more pronounced, LM-LC1-R60 appears to be a few timesteps ahead of the evolution in LD-LC1, a pattern that is consistent with the comparison between MLC130 and D-LC1.

Due to the blocking anticyclones of LM-LC1-R80, we do not see as much westward movement as we do in the LM-LC1-R60 experiment (figure 3.23b). The primary cyclone developed already on day 4 keeps intensifying. There is also some new frontal structure developing to the north of the cyclone which will over the next few days merge together. The 2PVU potential temperature field shows a very elongated meridional ridge wrapping cyclonically above the surface cyclone. The regions of the upper-level wind located over the regions of a lot of surface action are stretched meridionally in the northern direction that it is hitting the northern boundary (figure 3.25b). This results in the northward movement of the surface cyclone.

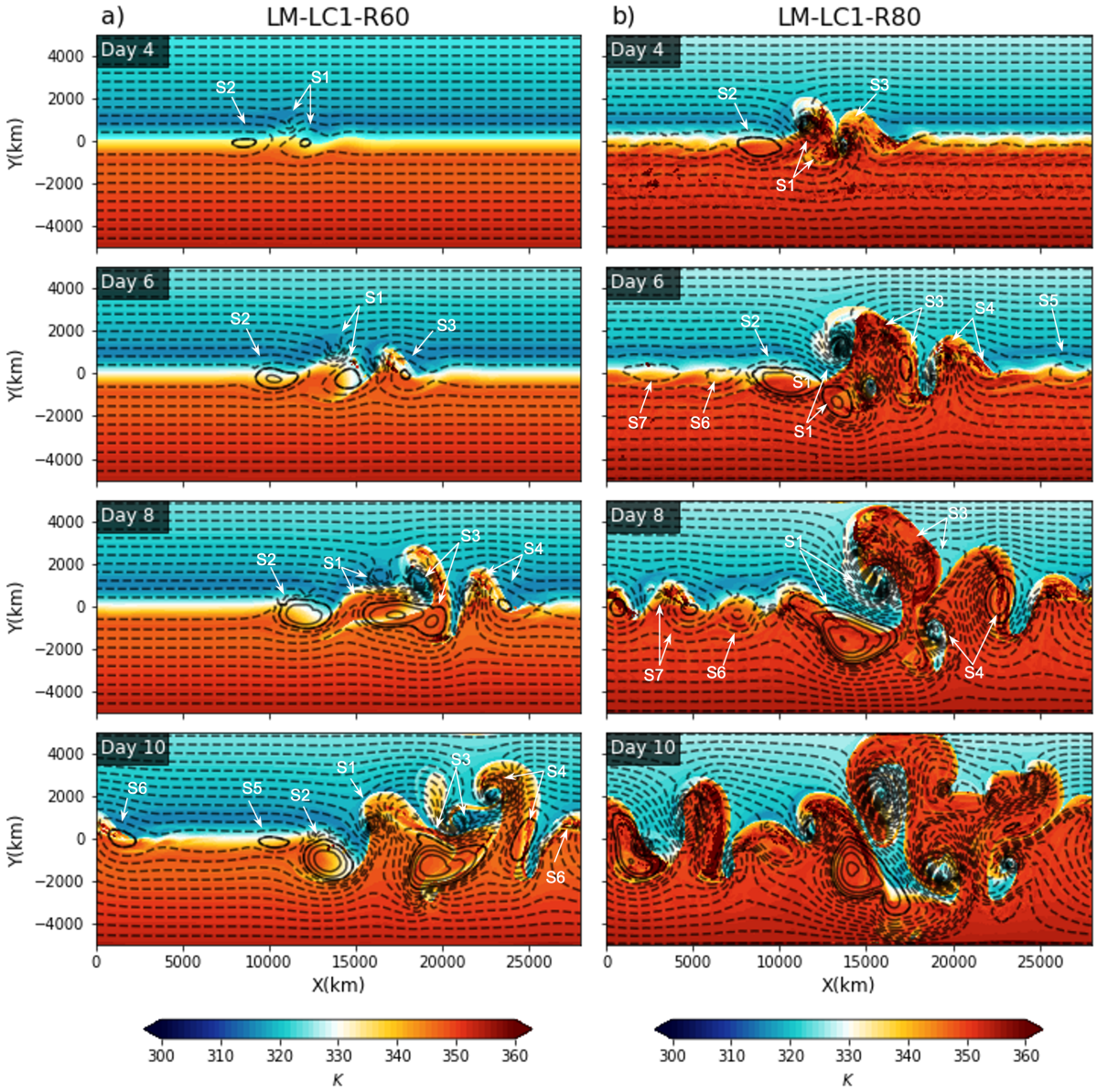

Figure 3.23: Surface pressure (black contours in hPa) and potential temperature on the PV = 2 PVU surface (shading in K) for a) LM-LC1-R60 and b) LM-LC1-R80. The contour lines are drawn at intervals of 5hPa, with the bold contour line representing the 1000hPa level. Dashed contours indicate pressure below 1000hPa and solid lines indicate pressure above 1000hPa.

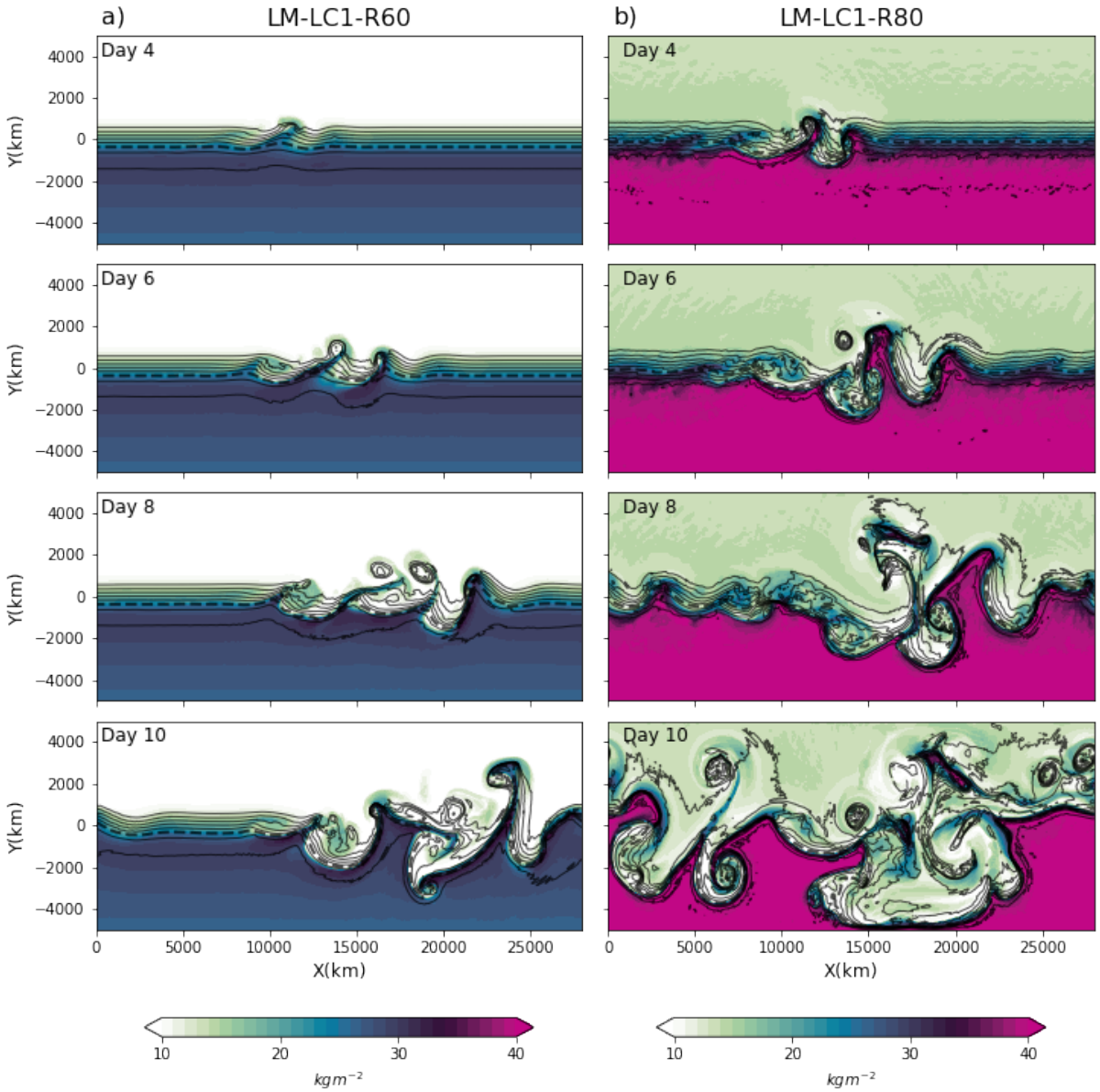

Figure 3.24: Potential temperature (contours in K) at 850hPa and TCWV (shading in kgm^{-2}) for a)LM-LC1-R60 and b)LM-LC1-R80. The contour lines are drawn at intervals of 5K, with the stippled contour line representing the 300K contour.

In LM-LC1-R80, the blocking anticyclones impede the westward movement as observed in the LM-LC1-R60 experiment (figure 3.23b). The primary cyclone (S1), which is already developed on day 4, continues to intensify. The 2PVU potential temperature field reveals a highly elongated meridional ridge wrapping cyclonically above the region of the surface cyclone. Furthermore, the upper-level wind situated over areas of significant surface activity is disorganized and stretched so far in the northern direction that it reached the northern boundary, resulting in the northward movement of the cyclones we experience at the surface (figure 3.25b).

Day 10

On day 10, in the LM-LC1-R60 experiment, we observed explosive growth of the cyclone connected to S4, moving several hundred kilometers northward, while its corresponding anticyclone remains relatively stationary, blocking the westward movement of succeeding systems (figure 3.17a). On the 2PVU potential temperature surface, we see the narrowing and meridional stretching of troughs that are typical of LC1 lifecycles, as the ridge over S4 wraps up cyclonically around the surface cyclone. The upper-level wind is also meridionally stretching up into the northern boundary (figure 3.25a). Similar to the behavior of M-LC1-R60, the addition of moisture with less initial relative humidity (RH) has accelerated the development of cyclones from day 6 onward, resulting in a faster evolution.

As observed in M-LC1-R80, the additional energy from diabatic heating intensified the meridional movement of the upper-level wind, causing it to hit the boundaries. This phenomenon is also observed in LM-LC1-R80 between day 8 and 10, resulting in a chaotic atmosphere on day 10.

EP-flux

In Figure 3.26a, we observe minimal momentum and heat fluxes before day 8. However, on day 8, there is a small contribution of heat fluxes to the EP-fluxes in the mid-troposphere, along with southward momentum fluxes in the upper troposphere. On day 10, there is a convergence of fluxes in the upper troposphere, specifically at around $y = 1000$km.

Compared to LD-LC1, we can observe a substantial increase in the density of EP-fluxes divergence and convergence in LM-LC1-R60, especially on days 8 and 10 when microphysics becomes more important. The zonal mean wind shows no significant difference until day 8 (figure 3.26d). However, from day 8 to day 10, there is a deceleration of the jet core and the general jet structure, accompanied by an increase in easterlies at the southern border. This is consistent with the convergence and divergence of the EP-fluxes observed on those days.

The EP-fluxes of LM-LC1-R80 are significantly stronger than that of LM-LC1-R60. The fluxes are already present on day 6, whereas they did not appear before day 8 in LM-LC1-R60 (figure 3.26c). Between day 6 and 10, the EP-fluxes are almost horizontally over the entire domain, particularly in the upper troposphere, indicating a substantial influence from momentum fluxes. The arrows are directed northward, indicating southward

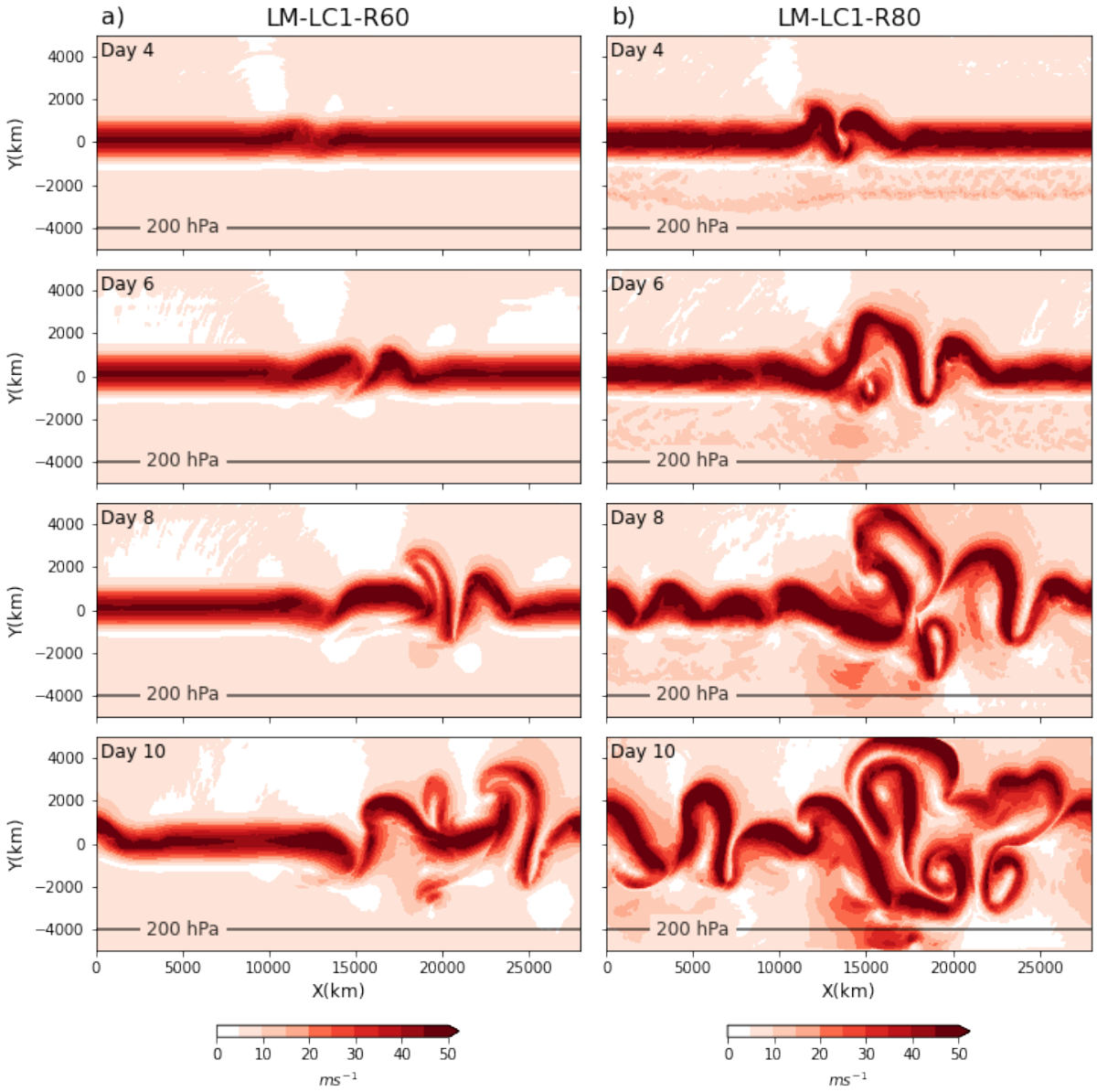

Figure 3.25: Total wind speed at 200hPa (shading in ms^{-1}) for a) LM-LC1-R60 and b) LM-LC1-R80

momentum fluxes. This is a somewhat unusual result, given the northward movement of the jet, but it may be due to the fact that the cyclones are in different stages of their lifecycle compared to the cyclones in modal perturbed experiments.

In comparison to LM-LC1-R60, there is a noticeable increase in EP-flux divergence and convergence in the LM-LC1-R80 experiment, starting from an earlier time. The zonal mean wind does not exhibit a noteworthy northward displacement until day 10, which might be influenced by the collision with the northern boundary (figure 3.26d). Nevertheless, there is a remarkable reduction in the surface westerlies from day 4 to day 6. On day 8, we observe a notable deceleration of the jet across the entire vertical domain, which corresponds well with the convergence of EP-fluxes located in the same region in the days beforehand.

Energetics

The shape of the EKE curve for LM-LC1-R60 follows that of LD-LC1, with a gradual increase in EKE (figure 3.22). However, the values of EKE are generally higher for LM-LC1-R60 compared to LD-LC1, indicating a more energetic atmosphere in the presence of moisture. This is consistent with the idea that moisture can enhance baroclinic instability and lead to stronger and more persistent low-pressure systems.

As observed in M-LC1-R80, there is a significant rise in energy levels in LM-LC1-R80 when compared to LM-LC1-R60 and LD-LC1 (figure 3.22). While the EKE levels for LM-LC1-R60 and LD-LC1 remain low until after day 6, LM-LC1-R80 shows a noticeable increase in EKE as early as day 3. By day 4, the conversion to EKE rapidly accelerates and reaches a maximum value of approximately $25 \cdot 10^5 \mathrm{Jm}^2$, which is a significant increase compared to the maximum value of EKE observed in LM-LC1-R60. As observed for M-LC2-R60, a moist atmosphere with higher relative humidity gives rise to explosive cyclone growth.

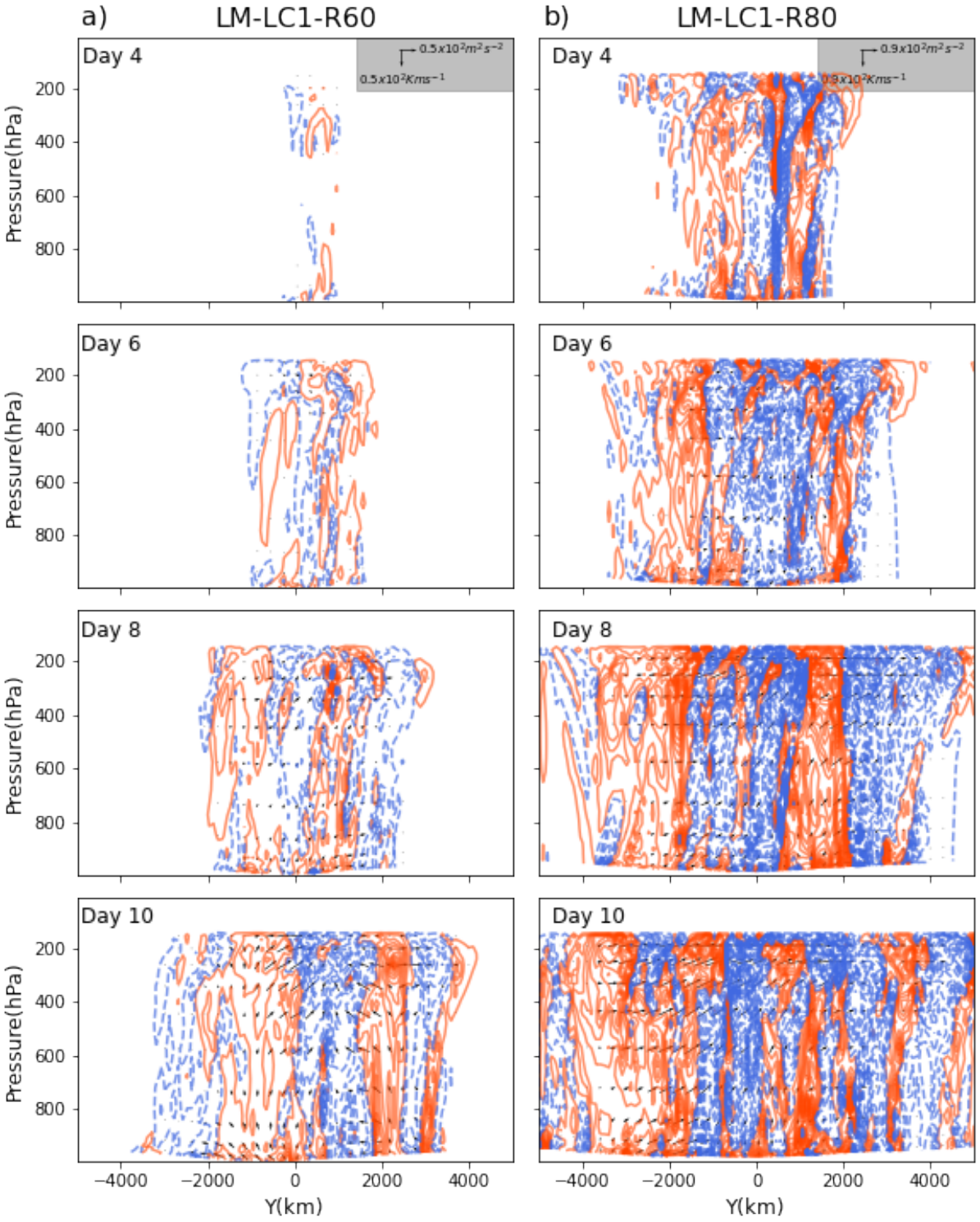

Figure 3.26: EP-flux (arrows, where the vectors are in m^2s^{-2} and Kms^{-2}) and its divergence (contours in ms^{-2}) for a) LM-LC1-R60 and b) LM-LC1-R80. The divergence is multiplied by 400. Solid red contours denote the flux divergence giving eastward flow acceleration. Dashed blue contours denote the flux convergence giving eastward flow deceleration. Contour interval is $10ms^{-2}$.

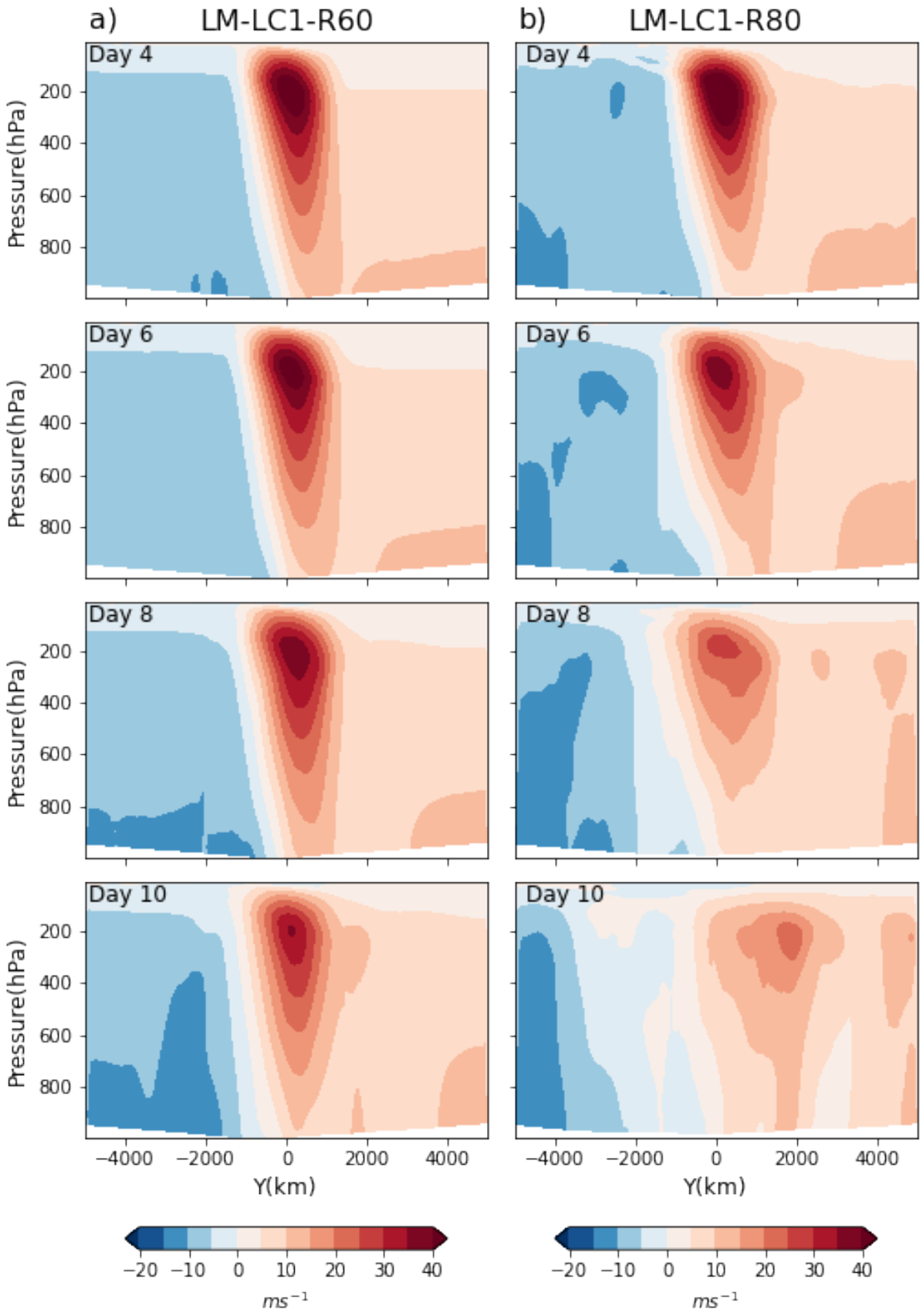

Figure 3.27: Zonal mean zonal wind (shading in ms^{-2}) for a) LM-LC1-R60 and b) LM-LC1-R80.

3.4.2 LM-LC2

Day 8

On day 8, LM-LC2-R60 and LM-LC2-R80 both display the formation of three surface cyclones (figure 3.28). C1 grew first, followed by C2 and C3 at slightly later timesteps. C2 developed downstream of C1 and C3 formed upstream of C1. The 850hPa potential temperature field shows stronger gradients on the east side of the ridge, corresponding to the warm fronts of C1 and C2. LM-LC2-R60 on day 8 still resembles LD-LC2 due to its less saturated initial conditions, while LM-LC2-R80 is slightly ahead in time due to the microphysics contributing to excess energy.

Day 10

By day 10, warm air moving northward in the upper troposphere is generating a ridge over C1 and C3, with the upstream cyclone (C3) intensifying most rapidly at the surface (figure 3.28). Unlike the downstream cyclone in LD-LC1, which splits into two cyclones, the downstream cyclone in the moisture experiments grows more intensely as a single cyclone. Furthermore, there is evidence of a new cyclone developing upstream of C3. The 850hPa potential temperature field now clearly displays the frontal structures of C3 (figure 3.29). The upper-level wind exhibits a slight southward curvature over the region of cyclone formation (figure 3.30b). On day 10, it is the upstream developed cyclones (C3, C5) that exhibit the most similar characteristics to the LC2 lifecycle. Compared to the dry evolution, the only difference is that the greater moisture content leads to faster growth and intensification of the cyclones.

Day 12

On day 12, the cyclones that were initially present on day 8 have detached from their warm source in the south, with LM-LC2-R80 breaking off slightly earlier than LM-LC2-R60 (figure 3.29). The 2PVU potential temperature field displays a NW-SE tilted wave with a clear cyclonic motion of the ridges, and the wave is confined meridionally with wider troughs, corresponding well with the typical characteristics of the LC2 lifecycle (figure 3.28).

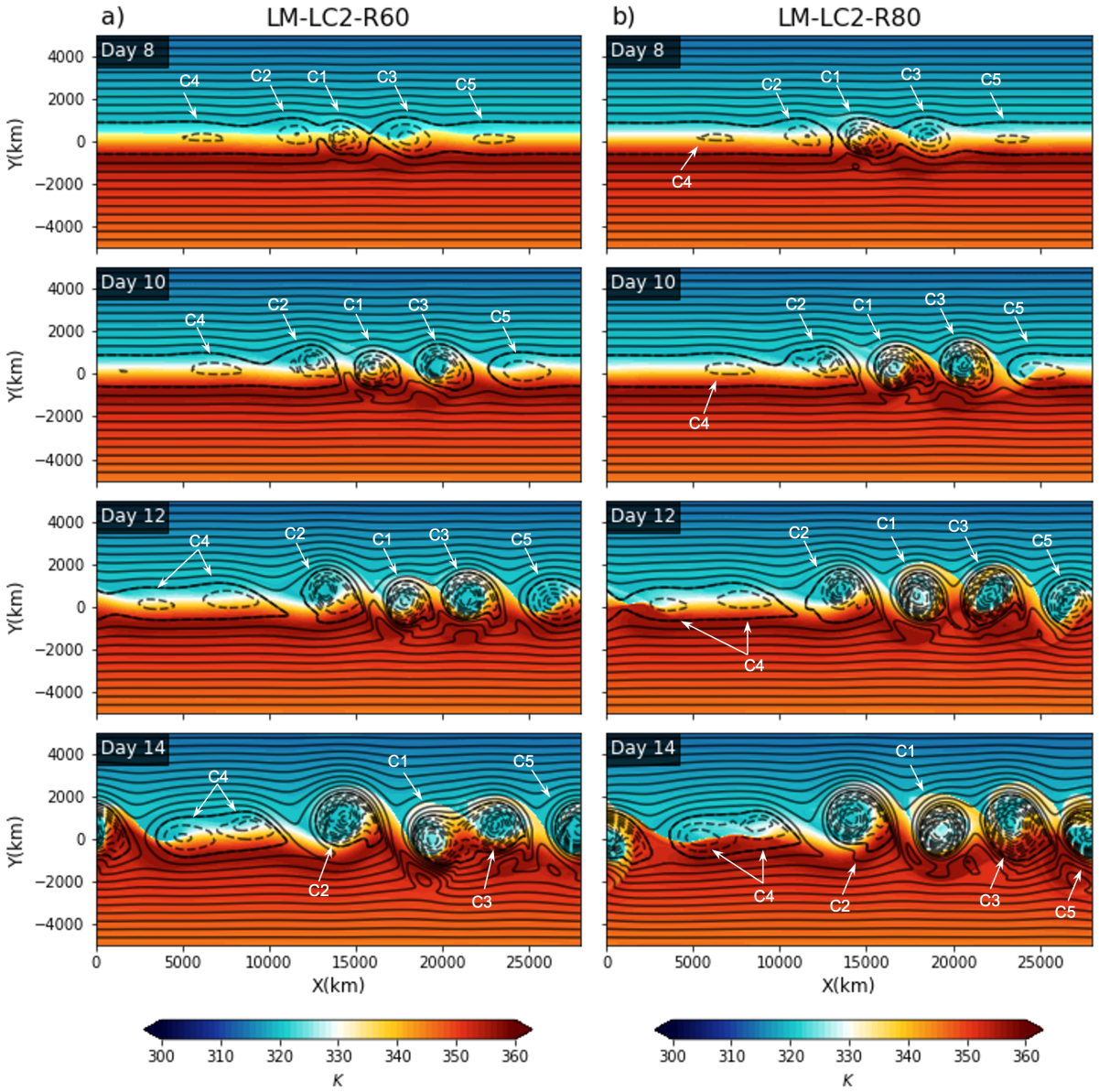

Figure 3.28: Surface pressure (black contours in hPa) and potential temperature on the PV = 2 PVU surface (shading in K) for a) LM-LC2-R60 and b) LM-LC2-R80. The contour lines are drawn at intervals of 5hPa, with the bold contour line representing the 1000hPa level. Dashed contours indicate pressure below 1000hPa and solid lines indicate pressure above 1000hPa.

Day 14

On day 14, we observe, the existing cyclones continue to expand, along with downstream cyclogenesis of the prevailing systems. These cyclones exhibit two pressure minima, similar to the downstream development observed in LD-LC2. Additionally, the upper-level wind shows clear signs of curving southward over the active surface regions, while remaining zonal over the less active regions.

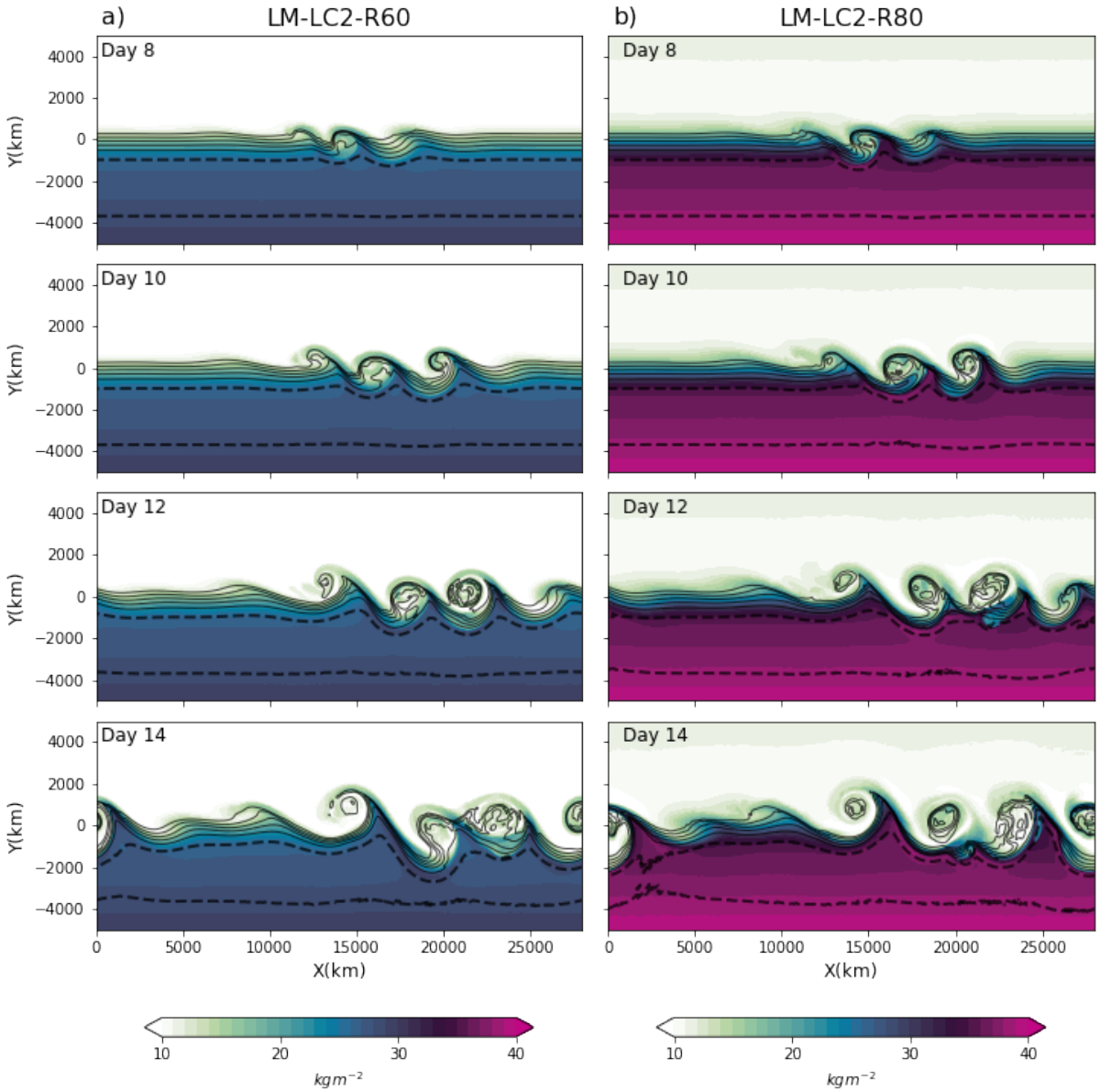

Figure 3.29: Potential temperature (contours in K) at 850hPa and TCWV (shading in kgm^{-2}) for a)LM-LC2-R60 and b)LM-LC2-R80. The contour lines are drawn at intervals of 5K, with the stippled contour line representing the 300K contour.

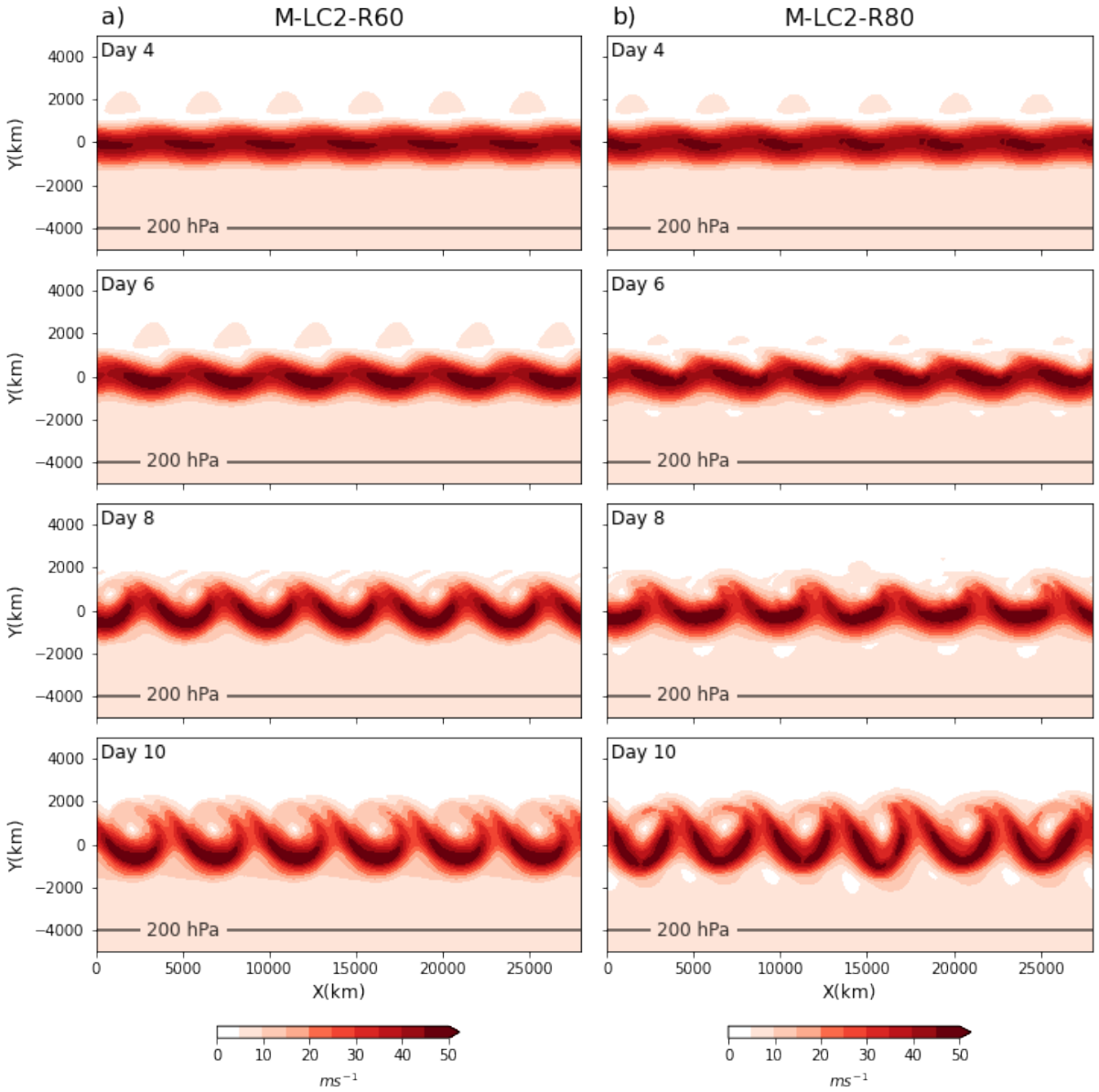

Figure 3.30: Total wind speed at 200hPa (shading in ms^{-1}) for a) LM-LC2-R60 and b) LM-LC2-R80

EP-flux

Similar to LD-LC2 (figure 3.20b), the EP-flux arrows are not visually apparent by day 8 in the LM-LC2-R60 and LM-LC2-R80, but the fluxes progressively intensify as the simulation progress (figure 3.31). Generally, the individual arrows indicate convergence at $y = 0$ and divergence towards the north and south. Over the following days, the fluxes continue to strengthen while the overall direction remains the same.

In LM-LC2-R60, the zonal mean wind, similar to LD-LC2, shows minimal changes from day 8 to 10 (figure 3.32a). Over the following days, there is a gradual decrease in the intensity of the jet core. Between day 12 and 14, the jet core weakens further, but not to the same degree as observed in LD-LC2 during the same time span. Unlike LD-LC2, the jet in LM-LC2-R60 still extends to the surface.

The placement of EP-flux contours in LM-LC2-R80 closely resembles that of LM-LC2-R60 throughout the simulation but with a greater density of the contours (figure 3.31). Furthermore, the jet core weakens more compared to the observations in LM-LC2-R80 This difference can be explained by the EP-flux contours, which show a greater convergence and divergence compared to LM-LC2-R60 (figure 3.32).

In general, EP-fluxes and the placement of EP-flux contours of LM-LC2-R60 and LM-LC2-R80 are highly comparable to those of the LD-LC2 experiment, with mid-tropospheric heat fluxes and upper tropospheric momentum fluxes contributing to the EP-fluxes (figure 3.31b). However, the inclusion of moisture strengthens the EP-fluxes. This is apparent by the higher values of convergence and divergence which act to accelerate or decelerate the zonal mean wind. The higher the moisture content the stronger the divergence and convergence of the EP-fluxes are.

Energetics

The EKE curve of both LM-LC2-R60 and LM-LC2-R80 exhibit a similar shape to that of LD-LC2 (figure 3.22.) However, we observe higher EKE values for both LM-LC2-R60 and LM-LC2-R80 compared to LD-LC2, with LM-LC2-R80 showing the highest values among the two simulations. This is consistent with the observed difference in the modal perturbed experiments (figure 3.6). A higher moisture content corresponds to a greater conversion of energy into EKE.

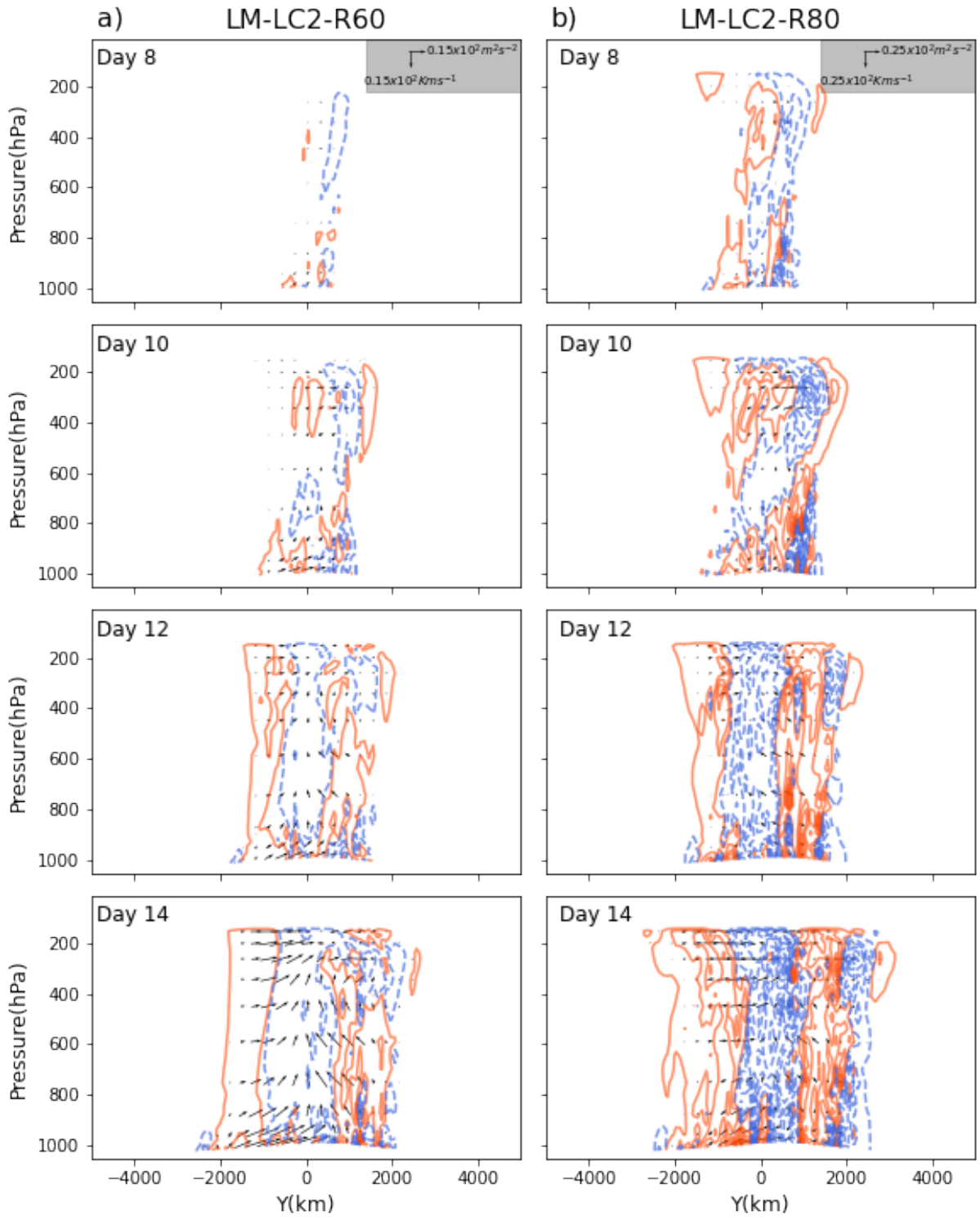

Figure 3.31: EP-flux (arrows, where the vectors are in m^2s^{-2} and Kms^{-2}) and its divergence (contours in ms^{-2}) for a) LM-LC2-R60 and b) LM-LC2-R80. The divergence is multiplied by 400. Solid red contours denote the flux divergence giving eastward flow acceleration. Dashed blue contours denote the flux convergence giving eastward flow deceleration. Contour interval is $10ms^{-2}$.

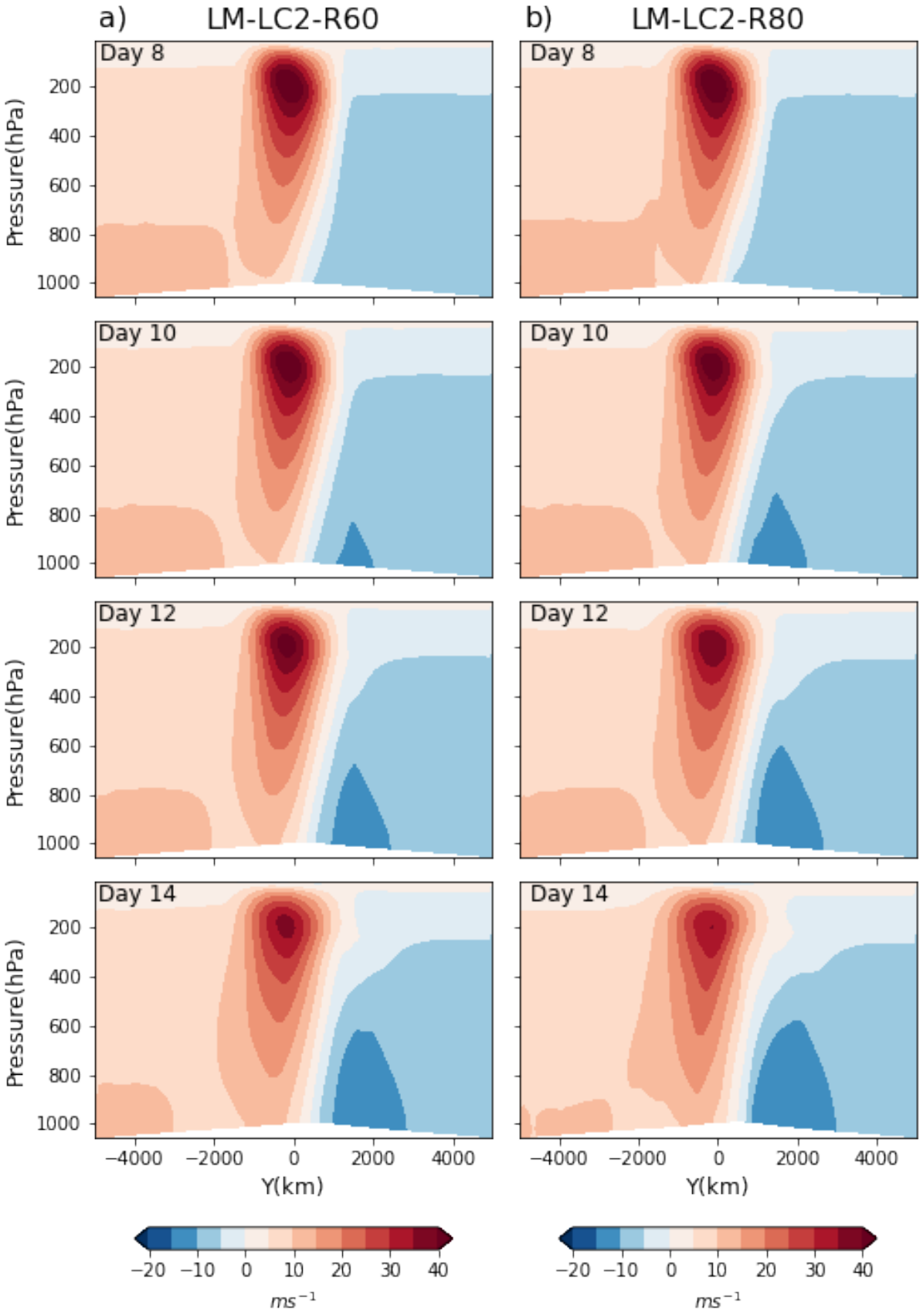

Figure 3.32: Zonal mean zonal wind (shading in ms^{-2}) for a) LM-LC2-R60 and b) LM-LC2-R80.

4 Summary and Conclusions

This thesis focuses on the impact of diabatic heating on the paradigmatic LC1 and LC2 baroclinic lifecycles THM93 using WRF within a zonally periodic channel with f-plane approximation. The first part of the results focuses on how our dry, modal experiments compare with THM93's simulations. Afterward, moisture is introduced and we observe how diabatic heating affects the synoptic evolution. In the second part, we carry out similar experiments but with localized surface perturbation instead of modal allowing for upstream and downstream development of cyclones and anticyclones.

The D-LC1 experiment is primarily marked by the emergence of large surface anticyclones accompanied by small, slowly evolving cyclones moving in a northerly direction. The 2PVU potential temperature field exhibits a clear anticyclonic motion of the temperature contours with the formation of narrow, elongated troughs. Meanwhile, the 850 hPa potential temperature field shows stronger gradients on the western side of the contours' ridge, which corresponds to the cold front of the cyclones. Additionally, the jet is observed to shift northward. These characteristics are comparable to THM93's LC1 simulation where they observe, amongst other things, the NE-SW tilt of the upper and lower potential temperature field, the northward shift of the jet, and growth of large anticyclones.

The D-LC2 experiment primarily grows large, meridionally confined cyclones. The 2PVU potential temperature field exhibits a clear cyclonic motion of the temperature contours with the formation of wider, meridionally confined troughs. At the same time, the 850 hPa potential temperature field features stronger gradients on the east side of the contours' ridge, corresponding to the warm front of the cyclones. Additionally, there is a minor southward shift in the jet. These characteristics are comparable to THM93's LC2 simulation where they observe, amongst other things, the NW-SE tilt of the upper and lower potential temperature field and the growth of large surface cyclones.

During the first 4-5 days of the M-LC1-R60 experiment, there is no noticeable difference in the synoptic evolution compared to D-LC1. However, from day 6 onwards, the 2PVU potential temperature field shows a distinctive change. While we still observe the development of elongated, narrow troughs characteristic of anticyclonic motion to the south, the ridge of relatively warm air is now bending westward and wrapping cyclonically around the surface cyclone. Throughout the simulation, we observe stronger gradients on the western side of the 850 hPa potential temperature field corresponding to the characteristics of D-LC1. The mean zonal wind profile features strong westerly winds approximately at y=1000 km which is suggestive of a northward shift of the jet.

The M-LC1-R80 experiment exhibits early cyclogenesis compared to the other modal LC1 experiments (D-LC1 and M-LC1-R60). The growth of anticyclones is slower, but we observe intensified cyclone growth. At 850hPa, we see strong gradients along both the cold and warm fronts with moisture transport to the far north. The 2PVU potential temperature field undergoes a notable change. While elongated and narrow troughs,

characteristic of anticyclonic motion, still develop to the south, the ridge of relatively warm air bends westward and wraps around the surface cyclone in a cyclonic manner. The jet shifts poleward, but its structure is not as coherent as seen for M-LC1-R60, likely due to the collision with the northern boundary.

The two moisture experiments for LC2 (M-LC2-R60 and M-LC2-R80) show similar evolution characteristics as D-LC2 with only slight intensification of the cyclones. The primary feature is the growth of meridionally confined cyclones with the clear cyclonic motion of the 2PVU potential temperature contours. At the lower levels, we observe strong gradients on the eastern side of the 850hPa potential temperature contours, and there is a minor southward shift of the upper-level jet.

In the experiments with localized perturbations, we observe the development of both upstream and downstream cyclones and anticyclones. The primary system in LD-LC1 (S1) exhibits anticyclonic behavior, which closely resembles what is observed in D-LC1, the main difference is that the cyclones of S1 develop at an earlier time compared to D-LC1. The developing systems upstream of the S1 (e.g. S3) demonstrate a combination of the anticyclonic motion of the 2PVU potential temperature contours to the south and cyclonic motion to the north. However, the S3 moves slower eastward compared to S1 and its slower progression obstructs the subsequent systems. Consequently, the succeeding systems interact with S3, causing a NE-SW shift in the 2PVU potential temperature field and intensifying the NE-SW tilt of the temperature contours.

LD-LC2 undergoes an extended period with no noticeable development. It takes until day 8 for surface cyclones to develop. The upstream cyclones show the expected characteristics already seen for D-LC2, whereas the downstream systems exhibit slower growth compared to upstream development.

In the first 4-5 days of the LM-LC1-R60 experiment, the synoptic evolution does not appear qualitatively different from that seen in LD-LC1. However, starting from day 6, S3 undergoes intense cyclone development. The anticyclone associated with S3 obstructs the westward movement of subsequent systems, while the corresponding cyclone experiences rapid intensification, resulting in a cyclonic wrap-up of the 2PVU potential temperature contours. Similar to the development observed in M-LC1-R60 and M-LC1-R80, the inclusion of moisture amplifies cyclone development and also induces cyclonic behavior in the 2PVU potential temperature contours.

When we increase the amount of available moisture (LM-LC1-R80), we observe intense cyclone development already by day 4. However, the growth of anticyclones appears to be slower in comparison to simulations with less (LM-LC1-R60) or no moisture (LD-LC1). At 850 hPa, we notice strong temperature gradients along both the cold and warm fronts, with moisture being transported much faster north compared to LM-LC1-R60. While the characteristic elongated and narrow troughs associated with anticyclonic motion still form to the south, a distinct cyclonic pattern emerges as the relatively warm air ridge bends westward and encircles the surface cyclone. Moreover, We observe the same blocking from the upstream anticyclone as observed in LD-LC1 and LM-LC1-R60.

The two moist experiments conducted for finite pressure perturbed LC2 cases (LM-LC2-R60 and LM-LC2-R80) present similar dynamics as in LD-LC2, with only a slight intensification in cyclone growth. The upstream cyclones exhibit the typical characteristics of LC2 cyclones with NW-SE tilt of the upper and lower potential temperature field. The downstream systems display slower development compared to upstream cyclones.

In conclusion, the addition of moisture in the model has a significant impact on cyclone development, leading to intensified and more rapid growth. This effect is particularly evident in the LC1 experiments. In the dry LC1 experiments (D-LC1 and LD-LC1), cyclogenesis occurs late in the simulation and tends to favor anticyclone development. However, when moisture is included in the LC1 experiments, cyclogenesis occurs earlier, and the growth of cyclones is intensified. Furthermore, we observe that the atmospheric circulation in the upper troposphere (200 hPa) drives cyclones further north. The change is less pronounced in the LC2 experiments. In the dry LC2 experiments (D-LC2 and LD-LC2), which already favor cyclone development, the inclusion of moisture only serves to intensify the growth, but the effects are not as noticeable as in the LC1 experiments.

We conducted two moisture experiments, one with a surface RH of 60% and the other with a surface RH of 80%, corresponding to TCWV values of 30 kgm^{-2} and 40 kgm^{-2}, respectively. In the experiment with lower saturation (RH = 60%), there was minimal difference in the synoptic evolution during the first 4-5 days compared to the dry simulation. Diabatic heating occurs when water vapor condenses, which requires the atmosphere to reach a sufficient level of saturation. With an initial surface RH of 60%, it takes more time for the atmosphere to become saturated. On the other hand, in the experiment with higher initial RH (RH = 80%), the atmosphere becomes saturated earlier, leading to earlier cyclogenesis and intensified cyclone development in M-LC1-R80 and LM-LC1-R80. Additionally, in LC1 experiments, higher initial RH results in a stronger northward transport of moisture. However, in LC2 experiments, the cyclones are inherently characterized by meridional confinement, regardless of the moisture content. Therefore, even with the inclusion of moisture, the moisture transport in LC2 experiments remains predominantly meridionally confined.

5 Outlook

Based on our findings from the test experiments aimed at selecting the optimal basic-state jet structure (not included in the results), it is clear that modifications to the underlying jet configuration lead to changes in the behavior of the 2PVU potential temperature field evolution, as well as the structure of the evolving cyclones and associated fronts. This observation is consistent with previous studies conducted by *Davies et al.* (1991), THM93, and *Wernli et al.* (1998). Despite some differences in the initial state prescribed in THM93 and*Jäger et al.* (2023), both studies show similar and distinct lifestyles. It is worth noting that THM93 and *Jäger et al.* (2023) employs a spectral model, whereas *Wernli et al.* (1998), *Davies et al.* (1991), and our experiments make use of the f-plane approximation. Furthermore, *Wernli et al.* (1998) and *Davies et al.* (1991) simplify their setups using the semi-geostrophic framework. Thus, for future investigations, it would be interesting to explore the sensitivity of the jet structure under the simplified f-plane approximation and the relatively simpler semi-geostrophic framework, in comparison to the use of a spectral model.

In the LC1 experiments, we observed a significant elongation of the 2PVU potential temperature cold air masses in the meridional direction. The inclusion of moisture further displaced the relatively colder air masses northward, eventually reaching the boundary. Consequently, it would be insightful to investigate the evolution of LC1 under a β-plane approximation, which accounts for variations in the Coriolis parameter (f) and tends to confine the system more effectively compared to the f-plane approximation. While the f-plane approximation adequately captures the essence of baroclinic instability, exploring the use of a β-plane approximation would add an additional layer of complexity to the simulations. By allowing for latitude-dependent changes in the f within the governing equations, the β-plane approximation would also provide a more realistic representation of large-scale atmospheric circulation, taking into account the latitudinal variation of f and allowing for Rossby wave propagation.

In our experiments, we have a horizontal, homogenous relative humidity profile as the basis for determining the moisture distribution of the atmosphere. Exploring the sensitivity of moisture distribution and how that affects the lifecycle presents an intriguing avenue for further investigation. For instance, one could consider implementing a relative humidity profile that exhibits different scale heights for the two halves of the meridional domain or different maximum surface relative humidity at the two halves of the meridional domain.

The analysis conducted in this thesis involves a visual examination of the synoptic evolution, as well as the inspection of the EP-flux and its divergence, and the EKE within the specified domain. It would be of particular interest to examine more thoroughly the impact of diabatic heating on cyclone evolution (its positioning and intensity). In particular, by looking at the effects of different positions and intensities of diabatic processes (e.g. by tweaking microphysics parameters in the simulations). In addition, a more quantitative approach could involve analyzing variables such as the growth rate,

propagation speed, and lifetime of the surface cyclones. This would provide further insights into the dynamics and characteristics of these weather systems, complementing the visual observations and calculations of the EP-flux, its divergence, and the EKE. By incorporating both qualitative and quantitative analyses, we can gain a comprehensive understanding of the synoptic evolution and the influence of diabatic heating associated with moist processes.

A Derivations

A.1 Shear emulating *Jäger et al.* (2023)

The shear (u_s), inspired by *Terpstra and Spengler* (2015),

$$u_s(y, z^*) = u_0 w_y(y) w_z(z^*), \tag{A.1}$$

where u_0 is the maximum shear velocity and z^* is the transformed vertical coordinate defined in equation (2.15). The horizontal ($w_y(y)$) shear function,

$$w_y(y) = \begin{cases} \left| cos^r \left(\frac{\pi}{l_y}(y - D) \right) \right|, & -l_y - s < y < -s, \\ -\left| cos^r \left(\frac{\pi}{l_y}(y - D) \right) \right|, & -s < y < l_y - s, \\ 0, & \text{otherwise}, \end{cases} \tag{A.2}$$

where l_y is the meridional length of the shear, s is the meridional shift of shear from $y = 0$, and r is the **...??**. The vertical ($w_z(z^*)$) shear function,

$$w_z(z^*) = \begin{cases} sin^t \left(\frac{\pi}{2} \frac{z - z_l}{z_0 - z_l} \right), & z_l \leq z \leq z_0, \\ sin^s \left(\frac{\pi}{2} \frac{z - z_u}{z_0 - z_u} \right), & z_0 < z \leq z_u, \\ 0, & \text{otherwise}, \end{cases} \tag{A.3}$$

where z_l, z_0, and z_u are the lower, core, and upper shear heights, respectively.

A.2 Barotropic shear

The barotropic shear ($u_{barotropic}$) is modified from the wind equations in appendix A.1,

$$u_{barotropic}(y, z^*) = u_0(u_s(y, z^*) + u_t(y)) = u_0(w_y(y) w_z(z^*) + u_t(y)), \tag{A.4}$$

where u_t represents the barotropic contribution, while u_s incorporates a sinusoidal function to ensure a smooth transition in regions without wind shear ($u_{barotropic} = 0$). The horizontal, vertical, and barotropic shear functions are as follows:

$$w_y(y) = \begin{cases} \left| cos^r \left(\frac{\pi}{l_y}(y - D) \right) \right|, & -l_y - s < y < -s, \\ -\left| cos^r \left(\frac{\pi}{l_y}(y - D) \right) \right|, & -s < y < l_y - s, \\ 0, & \text{otherwise}, \end{cases} \tag{A.5}$$

$$w_z(z^*) = \begin{cases} sin^s \left(\frac{\pi}{2} \frac{z - z_u}{z_0 - z_u} \right), & z_0 < z \leq z_u, \\ 0, & \text{otherwise}, \end{cases} \tag{A.6}$$

$$u_t(y) = \begin{cases} \left| cos^r \left(\frac{\pi}{l_y}(y - D) \right) \right|, & -l_y - s < y < -s, and\ z < z_b, \\ -\left| cos^r \left(\frac{\pi}{l_y}(y - D) \right) \right|, & -s < y < l_y - s, and\ z < z_b, \\ 0, & \text{otherwise}, \end{cases} \tag{A.7}$$

where z_b is the height of the barotropic contribution to the shear function.

A.3 Derivation of Elliasen-Palm flux

The EP-flux is derived from the QG-potential vorticity and buoyancy equations following *Vallis* (2017c),

$$\frac{\partial q}{\partial t} + J(\psi, q) = D, \quad q = \beta y + \left[\nabla^2 + \frac{\partial}{\partial z}\left(\frac{f_0^2}{N^2}\frac{\partial}{\partial z}\right)\right]\psi \quad , \quad 0 < z < H, \tag{A.8a}$$

$$\frac{\partial b}{\partial t} + J(\psi, b) + wN^2 = H, \quad b = f_0\frac{\partial \psi}{\partial z} \quad , \quad z = 0, H. \tag{A.8b}$$

Here, D and H are non-conservative terms of potential vorticity and heating term, respectively. equation (A.8b) is the boundary condition for equation (A.8a). If we assume no vertical velocity($w = 0$) and heating at the boundary we can reduce equation (A.8b) to:

$$\frac{\partial b}{\partial t} + J(\psi, b) = 0. \tag{A.9}$$

The next step is to divide the total flow (x) into a mean ($\bar{x}$) and eddy (x') component and then linearize. Assuming the mean is a zonal mean, $\partial\bar{q}/\partial x = 0$, $\bar{v} = 0$, we can rewrite equation (A.8a) to:

$$\frac{\partial q'}{\partial t} + \bar{u}\frac{\partial q'}{\partial x} + v'\frac{\partial \bar{q}}{\partial y} = D', \tag{A.10}$$

where D' is the eddy forcing and dissipation and,

$$q' = \nabla^2\psi' + \frac{\partial}{\partial z}\left(\frac{f_0^2}{N^2}\frac{\partial \psi'}{\partial z}\right), \bar{q} = \beta y - \frac{\partial \bar{u}}{\partial y} + \frac{\partial}{\partial z}\left(\frac{f_0}{N^2}\bar{b}\right), \frac{\partial \bar{q}}{\partial y} = \beta - \frac{\partial^2 \bar{u}}{\partial y^2} - \frac{\partial}{\partial z}\left(\frac{f_0^2}{N^2}\frac{\partial \bar{u}}{\partial z}\right). \tag{A.11}$$

The eddy potential vorticity (q') is known from equation (A.11). By multiplying with v' and replace $\nabla^2\psi' = \zeta'$ and $b = f_0\partial\psi'/\partial z$ we can write the eddy potential vorticity flux:

$$v'q' = v'\zeta' + f_0 v'\frac{\partial}{\partial z}\left(\frac{b'}{N^2}\right) \tag{A.12}$$

Two right-hand terms in equation (A.12) becomes:

$$v'\zeta' = -\frac{\partial}{\partial y}(u'v') + \frac{1}{2}\frac{\partial}{\partial x}(v'^2 - u'^2), \tag{A.13}$$

$$\begin{aligned} f_0 v'\frac{\partial}{\partial z}\left(\frac{b'}{N^2}\right) &= f_0\frac{\partial}{\partial z}\left(\frac{v'b'}{N^2}\right) - f_0\frac{\partial v'}{\partial z}\frac{b'}{N2} \\ &= f_0 v'\frac{\partial}{\partial z}\left(\frac{b'}{N^2}\right) - f_0\frac{\partial}{\partial x}\left(\frac{\psi'}{\partial z}\right)\frac{b'}{N^2} \\ &= f_0 v'\frac{\partial}{\partial z}\left(\frac{b'}{N^2}\right) - \frac{f_0^2}{2N^2}\frac{\partial}{\partial x}\left(\frac{\partial \psi'}{\partial z}\right)^2, \end{aligned} \tag{A.14}$$

and use this in equation (A.12):

$$v'q' = -\frac{\partial}{\partial y}(u'v') + \frac{\partial}{\partial z}\left(\frac{f_0^2}{N^2}v'b'\right) + \frac{1}{2}\frac{\partial}{\partial x}\left((v'^2 - u'^2) - \frac{b'^2}{N^2}\right) \tag{A.15}$$

By zonally averaging equation (A.15) we get the equation for the poleward flux of potential vorticity which is defined as,

$$\overline{v'q'} = \nabla \cdot \mathcal{F} = -\frac{\partial}{\partial y}(u'v') + \frac{\partial}{\partial z}\left(\frac{f_0^2}{N^2}v'b'\right), \tag{A.16}$$

where,

$$\mathcal{F} = -\overline{u'v'}\mathbf{j} + \frac{f_0}{N^2}\overline{v'b'}\mathbf{k}, \tag{A.17}$$

is the EP-flux.

Bibliography

Aon-Benfield (2010), Annual global climate and catastrophe report. 1

Bjerknes, J. (1919), On the structure of moving cyclones, *Monthly Weather Review*, *47*, 95 – 99, doi:https://doi.org/10.1175/1520-0493(1919)47<95:OTSOMC>2.0.CO;2. 2, 3

Bjerknes, J., and H. Solberg (1922), Life cycle of cyclones and the polar front theory of atmospheric circulation, *Geophysisks Publikationer*, *3*, 3–18. iv, 2, 3

Blackmon, M. L., J. M. Wallace, N.-C. Lau, and S. L. Mullen (1977), An observational study of the northern hemisphere wintertime circulation, *Journal of Atmospheric Sciences*, *34*, 1040 – 1053, doi:https://doi.org/10.1175/1520-0469(1977)034<1040:AOSOTN>2.0.CO;2. 4, 20

Bui, H., and T. Spengler (2021), On the influence of sea surface temperature distributions on the development of extratropical cyclones, *Journal of the Atmospheric Sciences*, *78*, 1173–1188, doi:10.1175/JAS-D-20-0137.1. 12, 15

Carlson, T. N. (1980), Airflow through midlatitude cyclones and the comma cloud pattern, *Monthly Weather Review*, *108*, 1498 – 1509, doi:https://doi.org/10.1175/1520-0493(1980)108<1498:ATMCAT>2.0.CO;2. 3

Charney, J. G. (1947), The dynamics of long waves in a baroclinic westerly current, *Journal of Atmospheric Sciences*, *4*, 136–162, doi:10.1175/1520-0469(1947)004<0136:TDOLWI>2.0.CO;2. 1, 4

Craig, G., and H.-R. Cho (1988), Cumulus heating and cisk in the extratropical atmosphere. part i: Polar lows and comma clouds, *Journal of Atmospheric Sciences*, *45*, 2622 – 2640, doi:https://doi.org/10.1175/1520-0469(1988)045<2622:CHACIT>2.0.CO;2. 5

Dacre, H. F., O. Martínez-Alvarado, and C. O. Mbengue (2019), Linking atmospheric rivers and warm conveyor belt airflows, *Journal of Hydrometeorology*, *20*, 1183–1196, doi:10.1175/JHM-D-18-0175.1. 1, 3

Danard, M. B. (1964), On the influence of released latent heat on cyclone development, *Journal of Applied Meteorology and Climatology*, *3*, 27 – 37, doi:https://doi.org/10.1175/1520-0450(1964)003<0027:OTIORL>2.0.CO;2. 5

Davies, H. C., C. Schär, and H. Wernli (1991), The palette of fronts and cyclones within a baroclinic wave development, *Journal of Atmospheric Sciences*, *48*, 1666 – 1689, doi:https://doi.org/10.1175/1520-0469(1991)048<1666:TPOFAC>2.0.CO;2. 4, 6, 76

Delden, A. V. (1999), The slope of isentropes constituting a frontal zone, *Tellus A: Dynamic Meteorology and Oceanography*, *51*, 603, doi:10.3402/TELLUSA.V51I5.14479. 5

Eady, E. T. (1949), Long waves and cyclone waves, *Tellus*, *1*, 33–52, doi:10.1111/J.2153-3490.1949.TB01265.X. 1, 4

Edmon, H. J., B. J. Hoskins, and M. E. McIntyre (1980), Eliassen-palm cross sections for the troposphere, *Journal of Atmospheric Sciences*, *37*, 2600 – 2616, doi:https://doi.org/10.1175/1520-0469(1980)037<2600:EPCSFT>2.0.CO;2. 20

Eliassen, A., and E. Palm (1960), On the transfer of energy in stationary mountain waves, *Geofysiske Publikasjoner*, *22*, 1–23. 20

Ferreira, J. A., M. L. Liberato, and A. M. Ramos (2016), On the relationship between atmospheric water vapour transport and extra-tropical cyclones development, *Physics and Chemistry of the Earth, Parts A/B/C*, *94*, 56–65, doi:10.1016/J.PCE.2016.01.001. 1

Holton, J. R., and G. J. Hakim (2012), *An Introduction to Dynamic Meteorology*, pp. 213–254, fifth edition ed., Academic Press, doi:10.1016/C2009-0-63394-8. 1

Hong, S.-Y., J. Dudhia, and S.-H. Chen (2004), A revised approach to ice microphysical processes for the bulk parameterization of clouds and precipitation, *Monthly Weather Review*, *132*, 103 – 120, doi:https://doi.org/10.1175/1520-0493(2004)132<0103:ARATIM>2.0.CO;2. 7, 8

Hoskins, B. J., and P. J. Valdes (1990), On the existence of storm-tracks, *Journal of Atmospheric Sciences*, *47*, 1854 – 1864, doi:https://doi.org/10.1175/1520-0469(1990)047<1854:OTEOST>2.0.CO;2. 5

Johannessen, R. (1970), *The Climate of Scandinavia, in: Climates of Northern and Western Europe, World Survey of Climatology*, vol. 5, pp. 23–80, Elsevier Science Ltd. 1

Jäger, F., P. Rupp, and T. Birner (2023), Robust poleward jet shifts in idealised baroclinic-wave life-cycle experiments with noisy initial conditions, *Weather and Climate Dynamics*, *4*, 49–60, doi:10.5194/WCD-4-49-2023. iii, 6, 14, 31, 76, 78

Kain, J. S. (2004), The kain–fritsch convective parameterization: An update, *Journal of Applied Meteorology*, *43*, 170 – 181, doi:https://doi.org/10.1175/1520-0450(2004)043<0170:TKCPAU>2.0.CO;2. 7, 8

Lamb, H. H. (1991), *Historic storms of the North Sea, British Isles, and Northwest Europe*, p. 204. 1

Liberato, M. L., J. G. Pinto, I. F. Trigo, and R. M. Trigo (2011), Klaus – an exceptional winter storm over northern iberia and southern france, *Weather*, *66*, 330–334, doi:10.1002/WEA.755. 1

Liberato, M. L., J. G. Pinto, R. M. Trigo, P. Ludwig, P. Ordóñez, D. Yuen, and I. F. Trigo (2013), Explosive development of winter storm xynthia over the subtropical north atlantic ocean, *Natural Hazards and Earth System Sciences*, *13*, 2239–2251, doi:10.5194/NHESS-13-2239-2013. 1

Lin, S. C., and P. J. Smith (1979), Diabatic heating and generation of available potential energy in a tornado-producing extratropical cyclone, *Monthly Weather Review*, *107*, 1169 – 1183, doi:https://doi.org/10.1175/1520-0493(1979)107<1169:DHAGOA>2.0.CO;2. 5

Lin, Y. L. (2007), *Mesoscale dynamics*, vol. 9780521808750, pp. 379–441, Cambridge University Press, doi:10.1017/CBO9780511619649. 5

Lorenz, E. N. (1955), Available potential energy and the maintenance of the general circulation, *http://dx.doi.org/10.3402/tellusa.v7i2.8796*, *7*, 157–167, doi:10.3402/TELLUSA.V7I2.8796. 19

Ludwig, P., J. G. Pinto, M. Reyers, and S. L. Gray (2014), The role of anomalous sst and surface fluxes over the southeastern north atlantic in the explosive development of windstorm xynthia, *Quarterly Journal of the Royal Meteorological Society*, *140*, 1729–1741, doi:10.1002/QJ.2253. 5

Moore, R. W., and M. T. Montgomery (2004), Reexamining the dynamics of short-scale, diabatic rossby waves and their role in midlatitude moist cyclogenesis, *Journal of the Atmospheric Sciences*, *61*, 754 – 768, doi:https://doi.org/10.1175/1520-0469(2004)061<0754:RTDOSD>2.0.CO;2. 5

Murray, R., and D. H. Johnson (1952), Structure of the upper westerlies; a study of the wind field in the eastern atlantic and western europe in september 1950, *Quarterly Journal of the Royal Meteorological Society*, *78*, 186–199, doi:10.1002/QJ.49707833607. 1

Papritz, L., and T. Spengler (2015), Analysis of the slope of isentropic surfaces and its tendencies over the north atlantic, *Quarterly Journal of the Royal Meteorological Society*, *141*, 3226–3238, doi:https://doi.org/10.1002/qj.2605. 5

Pfahl, S., and H. Wernli (2012), Quantifying the relevance of cyclones for precipitation extremes, *Journal of Climate*, *25*, 6770–6780, doi:10.1175/JCLI-D-11-00705.1. 1

Pierrehumbert, R. T., and K. L. Swanson (2003), Baroclinic instability, *https://doi.org/10.1146/annurev.fl.27.010195.002223*, *27*, 419–467, doi:10.1146/ANNUREV.FL.27.010195.002223. 1, 19

Polvani, L. M., and J. G. Esler (2007), Transport and mixing of chemical air masses in idealized baroclinic life cycles, *Journal of Geophysical Research Atmospheres*, *112*, doi:10.1029/2007JD008555. 14, 31

Robertson, F. R., and P. J. Smith (1983), The impact of model moist processes on the energetics of extratropical cyclones, *Monthly Weather Review*, *111*, 723 – 744, doi:https://doi.org/10.1175/1520-0493(1983)111<0723:TIOMMP>2.0.CO;2. 5

Schemm, S., H. Wernli, and L. Papritz (2013), Warm conveyor belts in idealized moist baroclinic wave simulations, *Journal of the Atmospheric Sciences*, *70*, 627–652, doi:10.1175/JAS-D-12-0147.1. 5, 13, 14, 15

Skamarock, W. C., J. B. Klemp, J. Dudhia, D. O. Gill, Z. Liu, J. Berner, W. Wang, J. G. Powers, M. G. Duda, D. M. Barker, and X.-Y. Huang (2021), A description of the advanced research wrf model version 4.3, doi:10.5065/1DFH-6P97. 7

Terpstra, A., and T. Spengler (2015), An initialization method for idealized channel simulations, *Monthly Weather Review*, *143*, 2043–2051, doi:10.1175/MWR-D-14-00248.1. 8, 16, 78

Thorncroft, C. D., B. J. Hoskins, and M. E. McIntyre (1993), Two paradigms of baroclinic-wave life-cycle behaviour, *Quarterly Journal of the Royal Meteorological Society*, *119*, 17–55, doi:10.1002/QJ.49711950903. iv, 1, 3, 4, 5, 6, 14, 19, 21, 22, 23, 24, 25, 27, 29, 30, 31, 33, 47, 73, 76

Vallis, G. K. (2017a), *Atmospheric and Oceanic Fluid Dynamics*, pp. 539–584, second edition ed., Cambridge University Press, doi:10.1017/9781107588417. 1, 2

Vallis, G. K. (2017b), *Atmospheric and oceanic fluid dynamics: Fundamentals and large-scale circulation, second edition*, pp. 335–378, second edition ed., Cambridge University Press, doi:10.1017/9781107588417. 19

Vallis, G. K. (2017c), *Atmospheric and Oceanic Fluid Dynamics*, pp. 379–412, second edition ed., Cambridge University Press, doi:10.1017/9781107588417. 20, 79

Vederman, J. (1954), The life cycles of jet streams and extratropical cyclones, *Bulletin of the American Meteorological Society*, *35*, 239–244, doi:10.1175/1520-0477-35.6.239. 1

Vincent, D. G., G. B. Pant, and H. J. Edmon (1977), Generation of available potential energy of an extratropical cyclone system, *Monthly Weather Review*, *105*, 1252 – 1265, doi:https://doi.org/10.1175/1520-0493(1977)105<1252:GOAPEO>2.0.CO;2. 5

Warner, T. T. (2011a), *Numerical Weather and Climate Prediction*, pp. 119–251, Cambridge University Press. 8

Warner, T. T. (2011b), *Numerical Weather and Climate Prediction*, pp. 17–118, Cambridge University Press. 21

Weijenborg, C., and T. Spengler (2020), Diabatic heating as a pathway for cyclone clustering encompassing the extreme storm dagmar, *Geophysical Research Letters*, *47*, 1–9, doi:10.1029/2019GL085777. 5

Wernli, H., R. Fehlmann, and D. Lüthi (1998), The effect of barotropic shear on upper-level induced cyclogenesis: Semigeostrophic and primitive equation numerical simulations, *Journal of the Atmospheric Sciences*, *55*, 2080 – 2094, doi:https://doi.org/10.1175/1520-0469(1998)055<2080:TEOBSO>2.0.CO;2. 4, 76

Wernli, H., M. A. Shapiro, and J. Schmidli (1999), Upstream development in idealized baroclinic wave experiments, *Tellus A*, *51*, 574–587, doi:10.1034/J.1600-0870.1999.00003.X. 4

Wernli, H., S. Dirren, M. A. Liniger, and M. Zillig (2002), Dynamical aspects of the life cycle of the winter storm 'lothar' (24–26 december 1999), *Quarterly Journal of the Royal Meteorological Society*, *128*, 405–429, doi:https://doi.org/10.1256/003590002321042036. 5